Toward quantitative limited-angle ultrasound reflection tomography to inform abdominal HIFU treatment planning

Daniel Heanes

Centre for Medical Image Computing
University College London

A dissertation submitted in partial fulfilment
of the requirements for the degree of
Master of Philosophy
of
University College London.

Department of Medical Physics and Bioengineering
University College London

January 12, 2018

Author Declaration

I, Daniel Martin Heanes, confirm that the work presented in this thesis is my own. Where information has been derived from other sources, I confirm that this has been indicated in the thesis.

Abstract

High-Intensity Focused Ultrasound (HIFU) is a treatment modality for solid cancers of the liver and pancreas which is non-invasive and free from many of the side-effects of radiotherapy and chemotherapy. The safety and efficacy of abdominal HIFU treatment is dependent on the ability to bring the therapeutic sound waves to a small focal ”lesion” of known and controllable location within the patient anatomy. To achieve this, pre-treatment planning typically includes a numerical simulation of the therapeutic ultrasound beam, in which anatomical compartment locations are derived from computed tomography or magnetic resonance images. In such planning simulations, acoustic properties such as density and speed-of-sound are assumed for the relevant tissues which are rarely, if ever, determined specifically for the patient. These properties are known to vary between patients and disease states of tissues, and to influence the intensity and location of the HIFU lesion.

The subject of this thesis is the problem of non-invasive patient-specific measurement of acoustic tissue properties. The appropriate method, also, of establishing spatial correspondence between physical ultrasound transducers and modeled (imaged) anatomy via multimodal image reg-istration is also investigated; this is of relevance both to acoustic tissue property estimation and to the guidance of HIFU delivery itself. First, the principle of a method is demonstrated with which acoustic properties can be recovered for several tissues simultaneously using reflection ultrasound, given accurate knowledge of the physical locations of tissue compartments. Second, the method is developed to allow for some inaccuracy in this knowledge commensurate with the inaccuracy typical in abdominal multimodal image registration. Third, several current multimodal image registration techniques, and two novel modifications, are compared for accuracy and robustness.

In conclusion, relevant acoustic tissue properties can, in principle, be estimated using reflected ultrasound data that could be acquired using diagnostic imaging transducers in a clinical setting.

Impact statement

The approach taken to estimate acoustic properties of a piecewise-homogeneous medium, particularly the principle of the novel method described in Chapter 4, could be investigated for possible implementation to improve the accuracy of clinical tumour targeting with HIFU.

Acknowledgements

I would like to thank my supervisors, Dr Dean Barratt and Prof Simon Arridge for their guidance, insights and encouragement. I am very grateful to Dean and my colleagues in CMIC and elsewhere in the Department of Medical Physics and Bioengineering at UCL for providing me with such a supportive day-to-day environment in which to work: Yipeng Hu, Ester Bonmati, Rachael Rodell, Eli Gibson and Paul Martin, to name a few. I also wish to thank Ben Cox for generously sparing the time to chat with me over technical matters. Much of the computing work involved would also have proved much more difficult had not the gentlemen of the Computer Science Helpdesk been so ready to offer their expertise when asked yet another “quick question” ...

I am grateful to my private tuition students and families for their moral and financial support, with Joe and Kate Richards particularly in mind.

Finally, I wish to thank my loving parents and brother: Ivor, Pamela and Jon, for their patience and encouragement.

This work was part-supported by the EPSRC under grant EP/F025750/1.

Contents

List of Figures

List of Tables

Glossary

BE	Boundary Element, 29
CT	Computed Tomography, 32
DFT	Discrete Fourier Transform, 50
DOF	Degrees Of Freedom, 106
ENIM	Echo-wise Normalised Integration Method, 76
FD	Finite Difference, 29
FE	Finite Element, 29
FOV	Field Of View, 100
GT	Ground Truth, 100
HIFU	High-Intensity Focused Ultrasound, 13
ICP	Iterative Closest Point, 106
INCS	Iterative Nonlinear Contrast Source, 31
ITK	Insight Segmentation and Registration Toolkit, 119
IVC	Inferior Vena Cava, 101
KZK	Kokhlov-Zabolotskaya-Kuznetsov, 31
MI	Mutual Information, 34
MR	Magnetic Resonance, 32
NMI	Normalised Mutual Information, 34

PDE	Partial Differential Equation, 29
PPW	Points Per Wavelength, 29
PSTD	Pseudospectral Time Domain, 32
RANSAC	Random Sample Consensus, 77
RHS	Right Hand Side, 29
ROI	Region Of Interest, 33
SMRF	Simultaneous Robust Multiple Fitting, 77
SSD	Summed Squared Differences, 52
TOF	Time Of Flight, 39
TRE	Target Registration Error, 37
US	Ultrasound, 32

List of symbols

Chapter 1

ρ	Mass density
c	Speed of sound
K	Bulk modulus
Z	Acoustic impedance

Chapter 2

β	Nonlinearity parameter (alternative to B/A)
δ	Thermoviscous diffusivity
$\mathbf{f}$	Volume force density
μ	Shear modulus
ω	Angular frequency
$\tilde{p}_k$	Spatial frequency domain expression for pressure
$\tilde{p}_\omega$	Temporal frequency domain expression for pressure
ξ_m	Relaxation constant
c_e	Small-signal sound speed
E	Young's modulus
G	Green's function
$I(\cdot,\cdot)$	Mutual information
k	Wavenumber

p	Acoustic pressure
q	Volume density of volume injection rate
S	Source term for a physical wave equation
t	Time

Chapter 3

α_0	conjugate gradient line search parameter
$\boldsymbol{\Phi}$	Acoustic medium parameter space
$\boldsymbol{\phi}$	Acoustic medium parameter vector
$\boldsymbol{\phi}^*$	Reference (true) acoustic medium parameter vector
$\delta(\cdot)$	Dirac delta function
$\epsilon_{\boldsymbol{\phi}}$	Termination tolerance on parameters
$\epsilon_{\mathcal{E}}$	Termination tolerance on cost function
$\mathbf{x}_r$	Position of r^{th} receiver
$\mathbf{x}_s$	Position of r^{th} source
$\mathcal{E}_{\text{ENV}}$	Envelope signal dissimilarity function
$\mathcal{E}_{\text{NIM}}$	*Normalised Integration Method* signal dissimilarity function
$\mathcal{E}_{\text{SSD}}$	Summed-squared differences signal dissimilarity function
μ	Attenuation coefficient
μ_a	Absorption coefficient
μ_{bs}	Back-scatter coefficient
ρ_0	Equilibrium density
ρ_0, c_0, K_0, Z_0	*Background* density, speed, bulk modulus and impedance
$\tilde{p}$	Adjoint acoustic pressure
$\tilde{S}$	Source term for an “adjoint wave equation”
B/A	Non-linearity parameter

$E[\cdot]$	Envelope functional
N_j	Number of transducer positions
N_k	Number of transducer array elements
N_r	Number of receivers
N_{pars}	Number of optimisation parameters
p	(Absolute) pressure
p^*	Reference (observed) acoustic pressure
p_0	Ambient pressure
p_{sr}	Pressure recorded at receiver r following excitation at source s
Q, P	Function spaces
$Q_{\text{NIM}}[\cdot]$	*Normalised Integration Method* functional
s, r	Source and receiver labels
T	Final time
u	Acoustic particle velocity
u	particle velocity
u_0	Ambient particle velocity
w_{sr}	Binary weighting constants

Chapter 4

$\delta_{\cdot,\cdot}$	Kronecker delta
$\hat{p}_{srm}$	Scaled template echo
$\mathcal{T}_m$	Travel-time surface
T_1	Echo amplitude fitting matrix
T_2	Echo phase fitting matrix
$\pi(\cdot)$	Permutation
$\psi(\cdot)$	Amplitude scaling model

ρ^*, c^*, K^*, Z^*	*Reference* (true) density, speed, bulk modulus, impedance
$\tilde{p}_{srm}$	Unit-amplitude template echo
$\tilde{t}_{srm}$	mth echo travel time at rth source after sth excitation
$a_{k,m}$	kth biquadratic coefficient for $\mathcal{T}_m$
f_0	Pulse centre frequency
M	Number of "reflection events"
m	"Echo" label
$N_{\tilde{s}}$	Number of sources
$q(\cdot)$	Template pulse
$q_a(\cdot)$	Analyic template pulse
t_{srm}	mth echo arrival time at rth source after sth excitation
W	Energy function
X	Vandermonde matrix of transceiver co-ordinate monomials

Chapter 5

Δt	Fractional sound intensity transmission coefficient
ζ	Registration transformation parameter vector
ζ^{GT}	Ground Truth registration transformation parameter vector
$\mathbf{d}$	Sound ray propagation direction
$\mathcal{T}$	Ultrasound-to-anatomical image co-ordinate mapping
$\mathsf{\Delta}$	Translation matrix (in homogeneous co-ordinates)
$\mathsf{NCC}^2(\cdot)$	Normalised cross-correlation image similarity measure
$\mathsf{NMI}(\cdot)$	Normalised mutual information image similarity measure
$\mathsf{Ph\_Ph\_MI}(\cdot)$	Local phase image similarity criterion
$\mathsf{Phor\_Phor\_MI}(\cdot)$	Local orientation image similarity criterion
$\mathsf{Pr\_Pr\_NCC}(\cdot)$	Vessel probability-based image similarity criterion

R	Rotation matrix (in homogeneous co-ordinates)
$\mathsf{U\_S\_LC2}(\cdot)$	Ultrasound simulation correlation image similarity criterion
μ	CT image intensity (Hounsfield number)
Ω_R^{CART}	‘Polar co-ordinate domain of R
Ω_R^{POL}	“Anatomical” co-ordinate domain of R
$\tilde{p}(\mathbf{x})$	“Echogenicity” at anatomical image point $\mathbf{x}$
$\widetilde{\mathsf{MR}}$	Pre-warped MR image
$A(\mathbf{x})$	Fractional intensity absorption factor along ray from $\mathbf{x}_0$ to $\mathbf{x}$
$a(\mathbf{x})$	Power absorption coefficient at anatomical image point $\mathbf{x}$
$f(\mathbf{x})$	US image intensity at CT image point $\mathbf{x}$ as simulated by Wein et al.
$H(\cdot)$	Entropy (of an image)
$H(\cdot,\cdot)$	Joint entropy (between two images)
$I(\mathbf{x})$	Simulated ultrasound intensity at anatomical image point $\mathbf{x}$
I_0	Maximal simulated ultrasound intensity
P	Surrogate abdominal “anatomy”
$p_{\mathsf{MR}}(I)$, $p_{\mathsf{US}}(I)$,	Vessel probability at image intensity I for MR, US
R	Ultrasound field-of-view
$r(\mathbf{x})$	Sound intensity reflection coefficient at anatomical image point $\mathbf{x}$
$S(\mathbf{x})$	Log-compressed simulated ultrasound intensity at anatomical image point $\mathbf{x}$
$s(\mathbf{x})$	Simulated US image “image source” at anatomical image point $\mathbf{x}$
$t(\mathbf{x})$	Cumulative fractional transmitted sound intensity at anatomical image point $\mathbf{x}$
U	Surrogate “real” ultrasound image
X	Surrogate “anatomical” image

Chapter 1

Introduction

1.1 Problem statement and proposed solution method

Patient-specific estimation of acoustic properties of tissues *in vivo* is not available in the current clinical practice of planning for *High Intensity Focused Ultrasound* (HIFU) of abdominal tumours, such as those of the liver and kidneys. Such estimation is needed *at least* for validation of assumptions made in this planning, and is potentially advantageous for ensuring the safety and efficacy of abdominal HIFU treatment.

Ultrasound is the natural physical field with which to interrogate tissue to obtain these properties. The waves used to probe the tissue could be delivered near HIFU frequencies and intensities, or at higher frequencies and lower intensities, where ultrasound imaging devices operate. The desire to estimate acoustic properties *before* inducing any tissue heating with HIFU motivates a possible approach where the estimation is done using data from a non-ablating device, such as an imaging transducer array. The same temperature dependence has been shown to hold for absorption coefficient in muscle, *whether or not the heating is delivered using HIFU*. This offers plausibility to the idea that acoustic property values estimated using imaging data may be *extrapolated* to values expected, based on knowledge of temperature dependence, in the HIFU regime.

Under this idea, a subproblem arises since the ultrasound data normally available in, or just prior to, a HIFU intervention consist of *reflected* signals which are sparse in spatial coverage, beamformed, and subject to additional processing. Spatially detailed quantitative mapping of acoustic properties from ultrasound tomography, by contrast, typically uses *transmitted* data from an array of sources and receivers, whose relavive positions are precisely localised in space, and which give a full angular coverage of the target.

In this thesis, a method to estimate, *in vivo*, acoustic properties of abdominal tissues is developed, modelling the patient's anatomy as a piece-wise homogeneous medium. Information about the locations of interfaces between different organs is used to regularise this estimation when the available data are reflected signals. This information, as well as knowledge of the spatial locations of ultrasonic sources and receivers, was obtained through registration of a previously acquired magnetic resonance or computed X-ray tomography image to the patient B-mode ultrasound imaging and spatial tracking of the ultrasound imaging probe. Throughout the work, the *acoustic approximation* is assumed to be valid, i.e. the media being modelled are treated as fluids and shear waves are neglected. While shear waves play an important role in abdominal HIFU treatment, so that the shear moduli of tissues are important quantities, particularly near the interfaces between ribs and soft tissues, this work focuses on developing methods for estimating the most important quantities needed to model acoustic waves and which determine the location of a HIFU focus; these are density, ρ, speed-of-sound, c, bulk modulus, K and acoustic impedance, Z, where, owing to the following relationships, each of these properties can be determined from any two of the others:

$$Z = \rho c, \tag{1.1}$$

$$K = \rho c^2. \tag{1.2}$$

1.2 Contributions

The main two contributions of the work are

i. A demonstration that accurate recovery of density and bulk modulus is possible in simple media using only *reflected* sound waves acquired over a *limited angular range*, when medium compartment interface locations are known,

ii. A novel method by which the above task can be accomplished when the interface locations are subject to an error describable with a small number of parameters.

A subsidiary contribution is a comparison of the performances of several current multi-modal image registration criteria in the same registration task.

Chapter 2

Literature Review

2.1 HIFU treatment planning

The first suggestion that beams of high-intensity focused ultrasound (HIFU) might be used for therapeutic purposes came in 1942 [1], after some biological effects of high-intensity ultrasound had been studied [2], and the possibility to *focus* an ultrasound beam using a curved transmitter surface had been investigated [3]. Thermal *ablation*, or destruction of tissue through localized heat transfer, typically occurs when local tissue temperature is brought outside the range $-20°C$ to $+55°C$, with focused ultrasound operating at the upper extreme. Therapeutic ultrasound integrated with imaging is now one of the most rapidly expanding techniques in image-guided therapy, with applications to ablation of targets in the brain, prostate, abdomen, uterus, eye, thyroid and bone [4, 5, 6, 7, 8, 9, 10]. Other, non-ablative, applications include disruptions of the blood-brain barrier, optimization of drug delivery and thrombolysis [11, 12, 6, 13].

Table 2.1, adapted from [14], lists current leading manufacturers of HIFU systems. Some of these systems are illustrated in Figures, 2.1, 2.2, 2.3, 2.4, 2.5 and 2.6.

Thermal ablation treatments with HIFU are currently carried out in the liver, pancreas, kidneys and uterus with one of a small number of clinically approved devices. The most commonly used extracorporeal devices are the HAIFU System (Chongqing HIFU, China), the HIFU Tumor Therapy System (China Medical Technologies, China), the Exablate 2000 system (Insightec, Israel), and the Philips Sonalleve system [15, 16]. The first two systems use a one- or two-element spherically-focused transducer, with B-mode ultrasound guidance imaging, while the Exablate and Sonalleve systems use electronically phased HIFU transducers with magnetic resonance (MR) guidance. In the pre-treatment planning phase for a treatment, an anatomical image is used to locate the target for ablation and to set the transducer positioning and driving parameters so as to place the HIFU beam focus at the desired treatment positions within the target. The rate of removal of heat from the tissue through blood perfusion is also taken into account, e.g. to determine sonication times. In clinical practice the simulation of the ultrasound beam path itself is typically of an ’incident field’ type, i.e. the tissue through which the beam propagates is assumed to be homogeneous [17].

Company	Device Trade Name / Guidance	Clnical Application	Status as of Dec 2011
InSightec, Haifa, Israel	ExAblate 2000/MR	extracoporeal, fibroids	FDA cleared for fibroid ablation
InSightec, Haifa, Israel	ExAblate 4000/MR	extracorporeal, bone, brain, breast, transrectal prostate	USA clinical and preclinical trials
Misonix/USHIFU Focus Surgery, Indianapolis, USA	Sonablate 500/US	transrectal prostate	approved in Europe (CE mark), USA clinical and preclinical trials
Phillips Healthcare P.O. Box 10.000, 5680 DA Best, the Netherlands	Sonalleve MR-HIFU/MR	Uterine fibroids	USA clinical and preclinical trials
EDAP TMS S.S. Parc d'actvités la Poudrette-Lamartine 4, rue du Dauphine, 69120 Vaulx-en-Velin, France	Ablatherm HIFU/US	transrectal prostate	approved in Europe (CE mark), Canada, Russia, Australia, South Korea; USA clinical and preclinical trials
Chongqing Haifu (HIFU) Technology 1 Qingsong Road Renhe, Yubel District, Chongqing 401121, China	Haifu/US	extracorporeal, liver, bone, fibroids, soft tissue sarcomas, kidney, pancreas etc.	USA clinical and preclinical trials
Mirabilis Medica 18706 North Creek Pkwy, Suite 110, Bothell, WA 98011, USA		extracorporeal fibroids	USA clinical and preclinical trials
Profound Medical, 3080 Yonge St, Suite 4040, Box 34, Toronto, Ontario, Canada M4N 3N1		transurethral/prostate	USA clinical and preclinical trials
SuperSonic Imagine Les Jardins de la Duranne, Bât E & F, 510 Rue René Decartes, 13857 Aix-en-Provence, France		brain	
Theraction Pépiniére Paris Santé Cochin, 29 rue du Faubourg Saint Jacques, 75014 Paris, France	TH-One/US	Parathyroid	USA clinical and preclinical trials in hyperparathyroidism
Image guided therapy 2, Allée du Doyen Brus, 33600 Pessac, France			USA preclinical breast cancert treatment and FUS mediated drug delivery

Table 2.1: Therapeutic FUS Companies with Oncologic Applications. Reproduced from [14]

Figure 2.1: ExAblate 4000 (InSightec) for trans-cranial ablation of brain tumours

2.2 Tissue heterogeneity and *ex vivo* characterisation

Some details are given next of the estimates of acoustic propagation parameters in tissues which have been employed in the literature for simulation in HIFU planning. The focus here, and in Chapter 2 of this thesis, is on sound speed and mass density, since these tissue parameters determine the important phenomena of reflection, refraction and linear wave interference.

One of the most widely cited reference texts on the values of acoustic propagation parameters of biological tissues is [18]. The plots shown in Figs 2.7,2.8,2.9 and 2.10 summarize results in [18] collected from [19, 20, 21, 22, 23, 24, 25, 26, 27, 28, 29, 30, 31, 32, 33, 34]. Figure 2.7 summarises speed-of-sound measurements compiled in [18] for liver at or near body temperature. The measurements by Bamber *et al.* (1979) [20] at 1597ms^{-1} and 1639ms^{-1}, were taken from bovine liver, and those by Nasoni *et al.*(1979) [28] by Bowen *et al.* (1979) [21] were from dog liver. The other results are from human liver.

One factor leading to speed variation between samples is the relative fat content of the liver, as the average speed in fat is somewhat lower than in other soft tissues and fluids. For example, the measurement plotted in Fig. 2.7 by Sehgal *et al* (1986) [31] at 1592ms^{-1} was of a sample containing 2.9% fat, whereas the same group measured 1522ms^{-1} in a sample containing 24% fat. This alone could contribute significantly to variation between patients. Figure 2.8 shows speed measurements compiled in [18] for skeletal muscle. The results by Miles *et al.* (1984) were from cow, with varying fat content; those from Nasoni [28] and [21] were from canine muscle, and those from Lewin & Busk (1982) [26] were from porcine muscle. The remaining three were from human forearm, psoas and eye muscle [29, 32, 22]

Figure 2.9 shows speed-of-sound measurements made at 37°C and collected in [18]. Those by [20]

Figure 2.2: Sonablate 500 (Misonix/USHIFU Focus Surgery) for prostate cancer treatment

Figure 2.3: Ablatherm HIFU (EDAP TMS) for prostate cancer treatment

Figure 2.4: Sonalleve MR-HIFU (Philips Healthcare), for treatment of uterine fibroids and palliative therapy for bone pain

Figure 2.5: Haifu (Chongqing HIFU), for ablation of liver, kidney and bone tumours

Figure 2.6: TH-One (Theraclion) for thyroid gland treatment

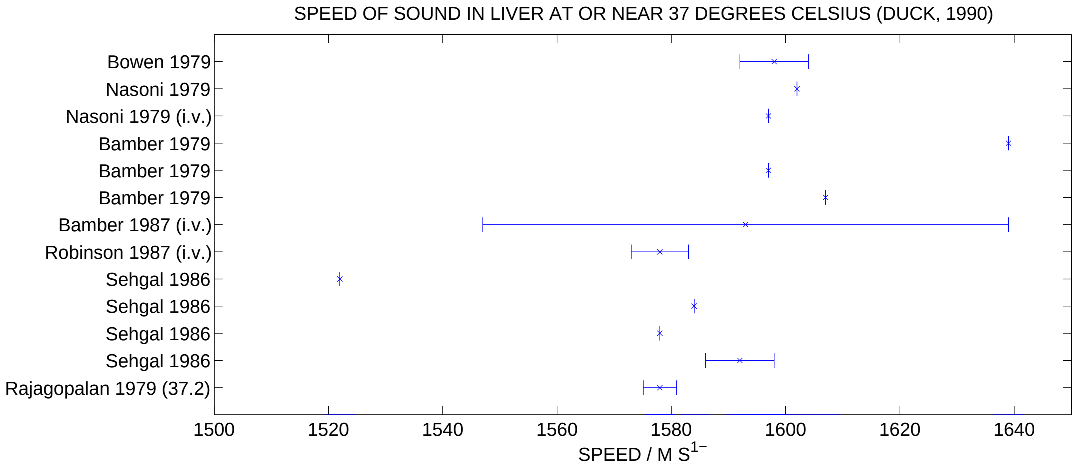

Figure 2.7: Speed of sound measurements in liver. Those labelled "i.v." were taken *in vivo*, and the rest *ex vivo*. Error bars show standard deviations.

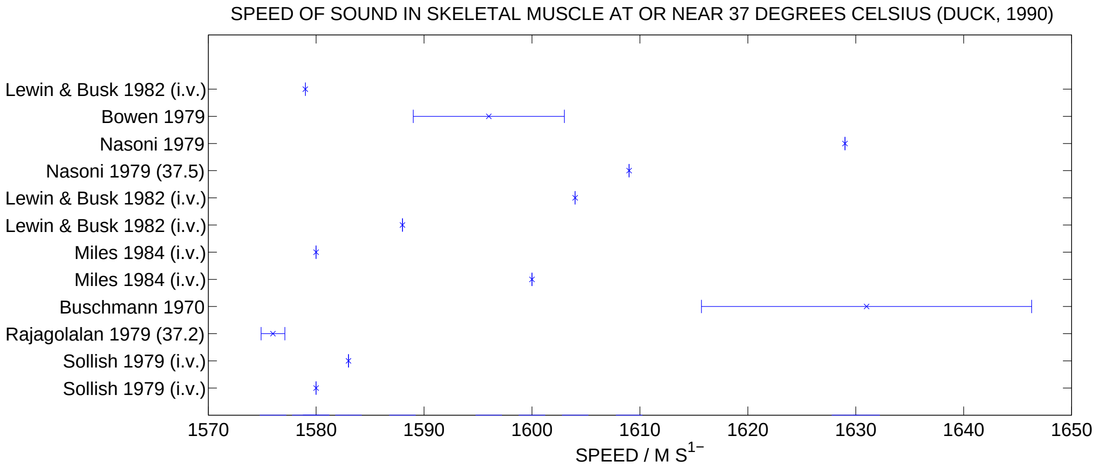

Figure 2.8: Speed of sound measurements in skeletal muscle. Those labelled "i.v." were taken *in vivo*, and the rest *ex vivo*. Error bars show ranges.

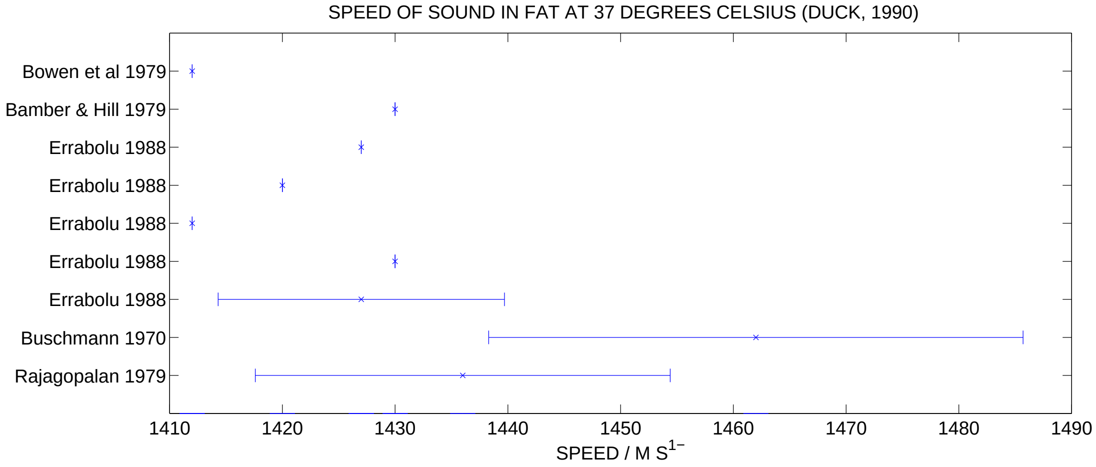

Figure 2.9: *Ex vivo* speed-of-sound measurements in fat. Error bars show ranges.

and [26] were from animal samples; those by Rajagopalan *et al.* (1979) [29], Buschmann *et al.* (1970) [22] and Errabolu *et al.* (1988) [23] from human samples, and the rest were unspecified in [18].

Duck *et al.* [18] present tissue density values from four sources, measured *ex vivo* by comparing apparent mass with and without submersion in water. However, temperatures at the time of measurement are not specified. Values for some adbominal tissues are summarized in Fig. 2.10.

Measurements taken from freshly excised tissue samples *ex vivo* (typically less than one hour after post-mortem for human or slaughter for animal) form the majority among published results, and have been regarded as sufficiently representative of the living tissue state. Figures 2.7 and 2.8 do not show a marked difference between *in vivo* and *ex vivo* measurements compared with the differences between the various investigators. These larger differences, whether due to the difficulties of accurate measurement, or to actual sample/patient differences, notably in fat content, are sufficiently large for speed-of-sound that the ranges for liver and muscle may even *overlap*.

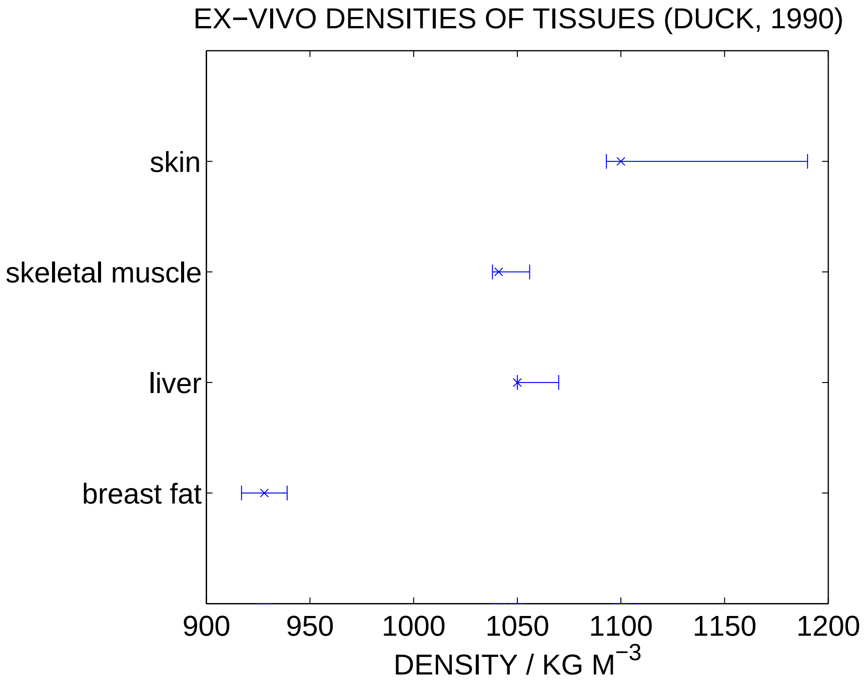

Figure 2.10: Densities measured *ex vivo* by a water displacement method. The error bars show ranges.

Some of the acoustic properties of tissues have been found to vary with disease states [35, 36], and also with each other. Broad features that have been associated with diseased tissue, and detectable with ultrasound, include increases in water content, acoustic scattering and density [36]. Diagnostic information visible in B-mode ultrasound images can be ambiguous, leading to research into methods of extracting quantitative tissue parameters from ultrasound data directly, before image formation. For example, fatty and cirrhotic livers produce almost indistinguishable diagnostic B-mode ultrasound images, while the slope of the attenuation coefficient with respect to frequency, estimable from reflection data, can be used to distinguish them [37]. Statistical analysis of the “speckle” patterns seen in B-mode images can be used to estimate (through the backscatter coefficient) effective scatterer sizes and concentrations. This microstructural information correlates to pathological states of liver tissue, and, for example, to a patient’s response to HIFU or chemotherapy in the liver [38, 39, 40, 41, 42, 43, 44, 45, 46, 47, 48, 49, 50].

> *“Although it might be supposed that speckle suppression would lead to an improvement in image perception this may not necessarily be so. The speckle in ultrasonics is not fully developed and its texture is influenced by larger-then-Rayleigh scatterers. For this reason, the image textures from different tissues may have different appearances which can assist in clinical image interpretations.”* [50]

A “highly significant” empirical linear relationship was found to hold between sound speed and density for a wide range of soft tissues, and also between the nonlinearity parameter “B/A” and each of density and speed [51], but none of these three parameters were found to correlate significantly with attenuation coefficient. Women with high mammographic breast density have a four- to fivefold increased risk of developing breast cancer compared to women with fatty breasts [52]. The strong correlation between sound speed and density in breast tissue has motivated work in ultrasound transmission tomography in the breast, e.g. [53, 52, 54, 55].

> *"The natural variation of the acoustical characteristics of biological media is often very broad and this range is further broadened by difficulty in making accurate measurements. As a consequence it is also difficult to specify in detail the wave-medium interaction mechanisms that are responsible for the observed acoustical characteristics."* [56]

It seems reasonable then, that if soft tissue interfaces affect a focused ultrasound beam path to the extent of shifting the focus by some millimeters, assuming a single value of speed for each tissue might well not enable sufficiently accurate prediction of this effect for different patients. This has been explicitly investigated in the brain, and in abdominal HIFU, where the depth to focus is typically around 15cm, the distorting effects of soft tissue interfaces may be even more severe than that reported in [57, 58]. In all studies involving ultrasound simulation for HIFU planning we have seen, a single value for each parameter, typically a subset of density, speed-of-sound, attenuation coefficient and absorption coefficient, has been assumed for each tissue compartment, and taken, either from a single previous measurement study, or as an average over several such studies. Figure 2.11 shows the dependencies in a selection of this work.

Tissue parameters of importance to the planning of HIFU delivery vary significantly with temperature. Since HIFU works through inducing a temperature increase, a knowledge of this variation is important. Attenuation and absorption coefficients in Np m^{-1} MHz^{-1} for *ex-vivo* muscle, liver and kidney (canine) were found to approximately double on heating with a water bath between 25 °C and 70 °C in [59]. The absorption coefficients were also shown to follow a very similar trend when the heating was accomplished *through HIFU exposure*. Canine liver samples measured in [60] showed sound speed variations with temperature of around 20 m s^{-1} at 3 MHz and 5 MHz. Such speed variations with heating are well known in HIFU and give rise to the phenomenon of *thermal lensing*, which has been shown to produce thermal lesion shifts of several millimetres [61, 62]. Tissue heating at a sufficiently high temperature causes the protein denaturation and tissue coagulation involved in HIFU lesioning. By measuring at 37$°C$ both before and after heating, the authors of [60] also showed that sound speed did not appear to be affected by tissue coagulation, but only temperature, whereas attenuation coefficient not only varies during heating, but is increased after coagulation as well. In this work, density was assumed not to vary over the temperature range.

The bulk modulus (K), shear modulus (μ) and Young's modulus (E) of any material are related by

$$E = \frac{9K\mu}{3K+\mu}, \tag{2.1}$$

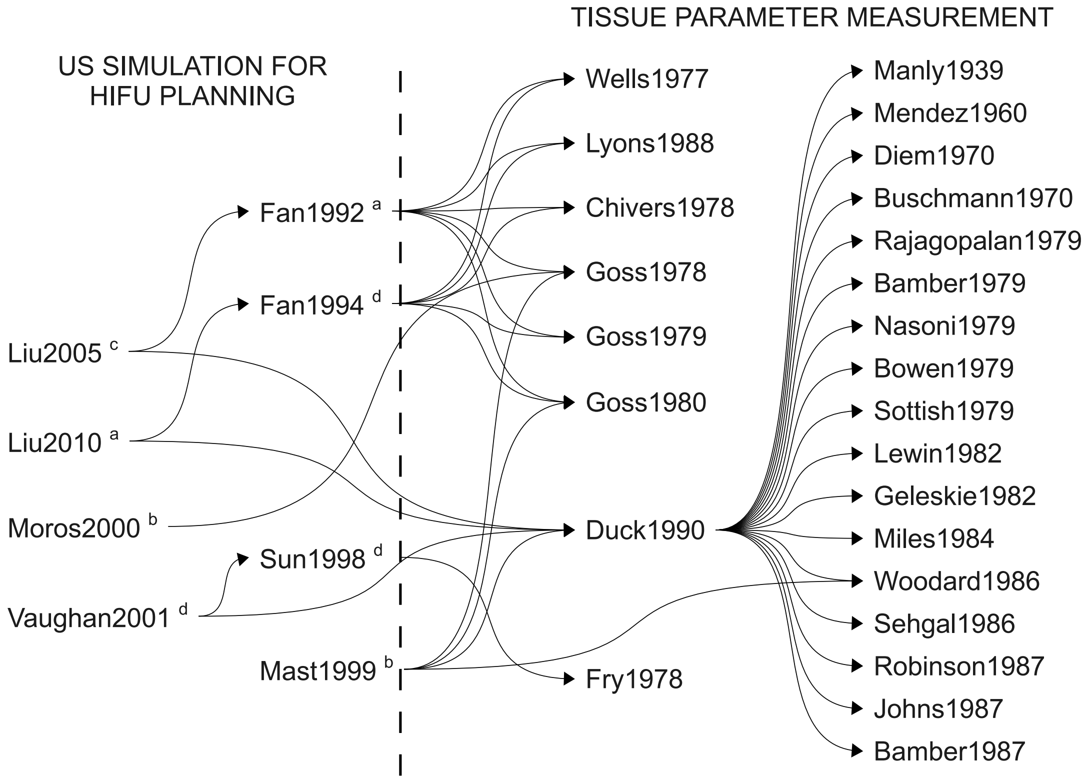

Figure 2.11: Citation diagram. The authors to the left of the dotted line modelled ultrasound propagation through tissue using literature values of acoustic tissue properties taken from the authors to the right. The main tissues compartments included in the modelling were: liver and overlying structures (a), chest wall (b), uterus and overlying structures (c), brain and overlying structures (d).

where, for human soft tissues, K is on the order of 1 GPa, and μ on the order of 1 kPa, so that $E \approx 3\mu$. The variation of K in tissue with temperature is relatively small compared with that of μ, which has been observed to increase by up to 74% in bovine liver samples for which irreversible changes occurred on heating from 25 °C to 55 °C ([63]). The shear modulus becomes an important parameter in modelling elastic wave propagation. Its variation in tissue, under HIFU conditions, along with that of viscosity, were also measured in [64].

2.3 Non-invasive characterisation of acoustic tissue properties

2.3.1 The acoustic inverse problem

The task of non-invasively estimating acoustic properties of human tissues such as density and sound speed, requires these properties to be inferred from the 'response' of the tissue to sound waves [REFERENCE SOMEONE?]. This observation means that the mathematical foundation to the task - which provides clear-cut results detailing what is and isn't possible, as well as general solution methods - naturally lies in the field of *wave equation constrained inverse problems*. From this perspective, a *direct problem* of mathematical physics is one in which one tries to solve a differential equation subject to given initial and/or boundary conditions and given the coefficients of the equation. These coefficients are typically functions of spatial position representing material properties, such as density, sound speed, thermal conductivity, electrical impedance, x-ray attenuation or stiffness, while the solution is the specification of some *field* variable over the whole spatial and temporal domain of interest, such as pressure, temperature, particle velocity, electrical potential or current density. Any of these quantities may be scalar-, vector- or tensor-valued in general. A *PDE-constrined inverse problem* is one in which one tries, given part of, or information about, a *solution* to a differential equation of physics, to find its *coefficents*.

The differential equations of interest in physical problems are typically second-order partial differential equations (PDEs), which may, depending on the values of their coefficients, be classfied as either *elliptic*, *parabolic* or *hyperbolic*. Differential equations describing wave propagation in time under general circumstances are hyperbolic. Kabanikhin [65] gives a useful classification of hyperbolic PDE-constrained inverse problems according to the type of data about the solution to the forward problem that is available.

In inverse **kinematic** problems, only data about travel times of signals between source points and receiver points are known.

In inverse **spectral** problems, the eigenvalues and norms of eigenfunctions of differential operators appearing in the PDE are deduced and used.

In inverse **dynamic** problems, the value of the field variable (solution) itself is recorded over time at one or more spatial locations, inside or on the boundary of the domain in which the PDE coefficients are sought.

In inverse **scattering** problems, the value of the field variable is typically recorded at locations in the far field, that is, at distances from the domain of interest which are large compared to the size of the domain itself.

A slightly more general classification, also considering elliptic and parabolic PDE's, appears in [66].

Aside from the type of data available, wave-equation-constrained inverse problems ("WECIP's") are classified as one-dimensional or multidimensional, according to how many spatial dimensions the PDE coefficients depend upon. Problems in which the medium is layered, i.e. is characterized by properties that vary in only one dimension, but in which waves can propagate in more than one dimension, may be classified in either way [67, 68, 66].

The following is a mathematical formulation of a direct problem in which a material property of some medium varies in one dimension only, as $q = q(x)$, while waves may propagate though the medium in this same dimension only. The solution, $u(x, t)$, to this direct problem is a scalar, such as the transverse displacement of a vibrating string.

$$\begin{aligned} \left(\frac{\partial^2}{\partial^2 t} - \frac{\partial^2}{\partial^2 x}\right) u = 0, \qquad & (x,t) \in \{\mathbb{R}^2 | t > 0\}, \\ u|_{t=0} = \delta(x), & \\ u_t|_{t=0} = 0. & \end{aligned}$$

It has been shown, [67], that, provided q is symmetrical about $x = 0$, i.e. $q(-x) = q(x)$, at least inside a region numerically equal in size to $[-T/2, T/2]$ (the wave speed above is equal to 1) then the data

$$u|_{x=0} = f(t), \qquad t \in (0, T]$$

enable the function q to be recovered uniquely within $[-T/2, T/2]$.

Similarly, [68], for a medium in which $x > 0$ with the conditions

$$\begin{aligned} u|_{t<0} &= 0 \\ u|_{x=0} &= f(t) \\ u_x|_{x=0} &= g(t), \end{aligned}$$

$q(x)$ may be uniquely determined from $f(t)$ and $g(t)$. In each of these formulations *three* conditions or sources of data are required.

When the wave motion itself is not restricted to one spatial dimension, slightly less dynamical information is required to recover more medium information. In the following direct problem, the density,

$\rho(x)$, and sound speed, $c(x)$, vary in one dimension only, x_1, but waves are able to propagate in any direction. The solution, $u(x,t)$ represents a scalar field, typically acoustic pressure.

$$\begin{aligned} u_{tt} - \rho c^2 \nabla \cdot (\rho^{-1} \nabla_x u) &= 0, \qquad (x,t) \in \mathbb{R}^m_+ \times \mathbb{R}, \\ \left.\frac{\partial u}{\partial x_1}\right|_{x_1=0} &= \delta(x')\delta'(t), \\ u_{t<0} &= 0. \end{aligned} \tag{2.2}$$

Here, $x = (x_1, \dots, x_m) = (x_1, x')$ and $\mathbb{R}^m_+ := \{x \in \mathbb{R}^m | x_1 > 0\}$.

Given the solution to 2.2 on x_1 for all x' and all t up to some positive T, i.e. given

$$u|_{x_1=0} = f(x', t), \qquad x' \in \mathbb{R}^{m-1}, \qquad t < T, \tag{2.3}$$

then $\rho = \rho(x_1)$ and $c = c(x_1)$ can be uniquely determined for x_1 up to some finite value that depends upon T and c itself [67]. In the case of two lateral co-ordinates ($m = 3$), where the f in Eq. 2.3 is axisymmetric, i.e. $f(x', t) = f(|x'|, t)$, these data may also be supplied as $\tilde{f}(|k|, t)$ the Fourier transform of $f(x', t)$ with respect to these two co-ordinates for two different values of $|k| = \sqrt{k_2^2 + k_3^2}$, [68]. As another alternative, they may be supplied as $\breve{f}(\xi, p)$, Radon transforms of $f(x', t)$ for two different vectors ξ.

2.3.2 Approaches with full data

2.3.3 Approaches with incomplete data

2.3.4 Incorporation of prior geometrical information

2.3.5 Techniques using (pre-processed) B-mode image data

Parameters estimated from analysis of (pre-processed) B-mode data include attenuation coefficient,[69], backscatter coefficient, [40, 43] and non-linearity parameter B/A, [70, 71]. Measuring sound speed in vivo using data from diagnostic transducers has proven more difficult [72, 73, 74], but specially oriented and triggered diagnostic probes have been used to obtain speed profiles from *transmission* data, with application to breast imaging, [75, 76]. A *single* diagnostic transducer array may also operate so as to detect transmitted energy in a technique known as *reflex transmission imaging* [77]. Reverberation from scattering sources *behind* the focal spot are detected and used to image the attenuation of tissue between these sources and the array. Ultrasound *elastography* is a widely used clinical technique which produces images of tissue *stiffness*, or Young's modulus, E and, in some forms, can give quantitative estimates of this quantity [78, 79], however, it does not provide any information about the bulk modulus, K.

2.4 Numerical methods for simulating acoustic wave propagation

Those computational methods for estimating acoustic tissue properties which attempt to take account of more than superficial features of ultrasound physics typically involve repeated numerical simulation of wave propagation through the medium concerned. From a mathematical point-of-view, this amounts to solving, numerically, a suitable partial differential equation (PDE) to obtain a field variable, such as pressure or particle velocity as a function of space and time, or space and frequency. The variety of physical features to be reproduced in the simulation determine the choice of PDE, and the term “model” generally refers to the equation itself. Under the *acoustic approximation*, the propagation medium does not support shear stresses, as is the case for fluids, so that no transverse (shear) waves are present. The treatment of transverse waves in solids is outside the scope of this thesis. One of the simplest acoustic models is the one-dimensional linear, lossless wave equation for a homogeneous fluid medium with small-signal sound speed c_e, as for Eq. **??**, and excitation $S(x,t)$. In Eq. 3.13, $p(x,t)$ is *acoustic* pressure, i.e. the pressure deviation about the ambient mean due to the presence of the wave:

$$\frac{\partial^2 p}{\partial x^2} - \frac{1}{c_e^2}\frac{\partial^2 p}{\partial t^2} = -S(x,t) \tag{2.4}$$

A more realistic model, also in the time domain, would include additional terms, to approximately account for physical effects expected to play a significant role in the problem being studied. While remaining within the *acoustic approximation*, i.e. neglecting shear stresses and elasticity in the medium, these may include small variations in sound speed (term ’a’ in Eq. 2.5), small variations in density (’b’), absorption due to thermoviscous difffusivity (’c’), acoustic nonlinearity (’d’) and absorption due to additional relaxation mechanisms (’e’). Eq. 2.5 combines features of models used in [80, 81].

$$\nabla^2 p - \frac{1}{c_e^2}\frac{\partial^2}{\partial t^2} = -S(\mathbf{x},t) - \overbrace{\frac{2\Delta c}{c_e^3}\frac{\partial^2 p}{\partial t^2}}^{\text{(a)}} + \overbrace{\frac{1}{\rho_e}\nabla(\Delta\rho)\cdot\nabla p}^{\text{(b)}} - \overbrace{\frac{\delta}{c_e^4}\frac{\partial^3 p}{\partial t^3}}^{\text{(c)}} - \overbrace{\frac{\beta}{\rho c_e^4}\frac{\partial^2 p^2}{\partial t^2}}^{\text{(d)}} + \overbrace{\sum_{m=1}^{v}\xi_m}^{\text{(e)}} \tag{2.5}$$

A number of famous wave equations approximate degrees of physical realism “between” those of Eq. 3.13 and 2.5, such as the Burgers, Blackstock, Kokhlov-Zabolotskaya-Kuznetzov (KZK) and Westervelt equations. Absorption may be modeled in several ways, including replacing term (c) above by a fractional derivative term for non-viscous media with frequency power-law absorption [82]. Wave equations attempt to model all frequency components of the wave simultaneously, but, by working in the temporal frequency domain, individual Fourier components can be simulated separately. This offers a computational speed-up in cases of *linear* propagation, where no energy is transferred between different frequency components of the wave, and amounts to solving a *Helmholtz* equation, of which one of the simplest comes from Fourier transforming Eq. 3.13

$$\partial_x^2 \tilde{p}_\omega + k^2 \tilde{p}_\omega = -\tilde{S}_\omega(x) \tag{2.6}$$

where $k = \omega^2/c_e^2$ is the wavenumber for a particular frequency ω. For large amplitude-to-wavelength ratios, the local sound speed of a medium begins to depend upon the density, due to high density fluctuations, resulting in wavefront steepening behaviour approximately modeled by term (d) in Eq. 2.5. Since terms like this come from using a *nonlinear* equation of state and result in a wave equation which is nonlinear in the field variable (in this case p), this phenomenon is known as *nonlinearity*. Nonlinear wave equations are particularly challenging to solve because of the very small grid spacing which must typically be used to represent the high frequency waves which result from them. Some of the main approaches are summarized below.

2.4.1 Finite-difference, finite-element and boundary element methods

All numerical methods can be categorized as operating in the time domain, or frequency domain, depending on whether they solve a problem equivalent to a wave equation or a Helmholtz equation (respectively). So-called “full-wave” methods are those which inherently model diffraction, refraction and reflection. Partial-wave methods, such as ray-tracing and projection methods are therefore less accurate for many problems, while generally faster. The full-wave FD, FE and BE methods are suitable for modelling propagation in strongly heterogeneous media, and are the most commonly used methods [80, 83, 84, 85]. The Boundary Element Method is well suited to infinite-domain problems, and to *piecewise* homogeneous media, but cannot handle complex small-scale medium variation well. Finite elements are well suited to small-scale medium variation but cannot handle unbounded problems, such as scattering problems as well as BEM. The FD method can handle both unbounded domains and small heterogeneities but requires a regular spatial grid discretization, whereas FEM lends itself to less computationally costly discretization through adaptive mesh sizing. As a rough rule-of-thumb, FD and FEM need a spatial discretization of around ten points-per-wavelength (10 PPW), and this requirement can rise *with* wavenumber, a phenomenon known as “numerical pollution” [86]. Iterative solvers for BEM can require that multiple matrix-vector products be computed, so that computational complexity can scale as $O(N^2)$ for N parameters, whereas FD is a *matrix free* method that scales as $O(N)$. Since it is based on reformulation of the PDE as an integral equation, BEM is applicable only when the Green’s function of the differential operator in the PDE is known.

Figure 2.12 attempts to express the relationship between the common techniques for numerical solution of wave and Helmholtz equations.

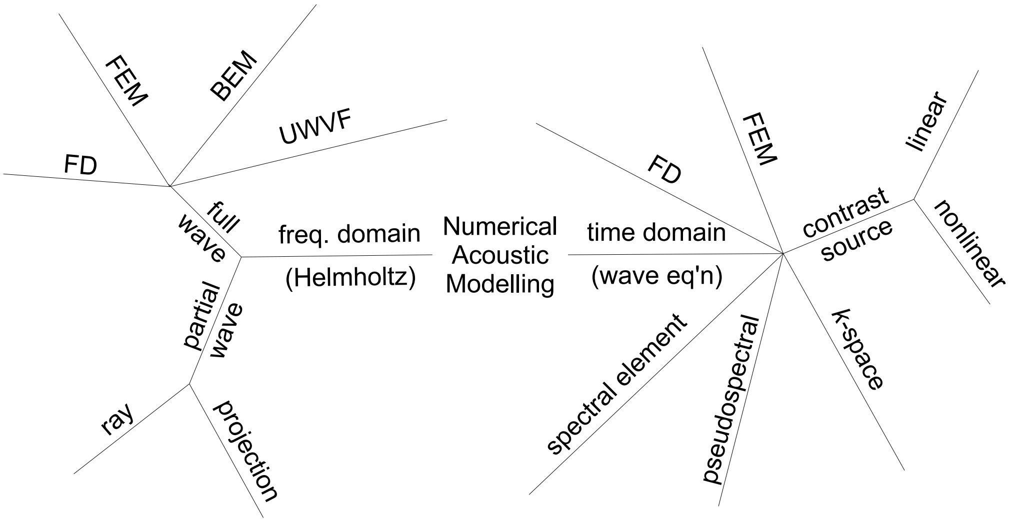

Figure 2.12: Numerical methods for acoustic simulation

2.4.2 Green's Function-based methods: *Field II* and *INCS*

As well as their place in BEM, Green's functions, when known for a given differential operator, can be used to “invert” (solve) the operator equation (the PDE) in a single step if the problem is (treated as) linear, or iteratively if it is non-linear. A well-known implementation of the first approach is the *Field II* MATLAB code by Jørgen Arendt Jensen [81], designed to simulate B-mode ultrasound in heterogeneous media. This is a time domain method for solving

$$\nabla^2 p - \frac{1}{c_e^2}\frac{\partial^2 p}{\partial t^2} = -\frac{2\Delta c}{c_e^3}\frac{\partial^2 p}{\partial t^2} + \frac{1}{\rho_e}\nabla(\Delta p)\cdot\nabla p. \tag{2.7}$$

The terms on the right hand side are treated as *contrast sources* and convolved with the appropriate Green's function to obtain acoustic pressure p, as $p = p_i + p_s$, for

$$p_s(\mathbf{r}_2, t) = \int_V \int_T \left[\frac{1}{\rho_e}\nabla[\Delta\rho(\mathbf{r}_1)]\cdot\nabla p(\mathbf{r}_1, t_1) - \frac{2\Delta c(\mathbf{r}_1)}{c_e^3}\frac{\partial^2 p(\mathbf{r}_1), t_1}{\partial t^2}\right] \times G(\mathbf{r}_1, t_1|\mathbf{r}_2, t_2)dt_1 d^3 r_1. \tag{2.8}$$

Here, $\mathbf{r}_2$ is a receiver position, and $\mathbf{r}_1$ a scatterer position. Since p itself appears inside the integrand, 2.8 cannot be solved for p outright. It is a nonlinear inverse problem even though the wave equation Eq. 2.7 is linear in p, and solution strictly requires a Born-Neumann expansion, where the convolution is repeated iteratively. However, Jensen et al. argue that secondary scatters will be significantly weaker than primary scatters and so substitute incident p_i for p in the RHS of 2.8, i.e. use the *Born approximation*. The heterogeneity quantities $\Delta\rho$ and Δc are generated by first placing several thousands of random point scatterers in the medium.

When the PDE to be solved is itself nonlinear in the field variable, a Green's function may, for sufficiently weak non-linearity, be iteratively convolved with a contrast source including, this time, the nonlinearity term of the PDE. The lossless Westervelt Eq. (2.9) is a wave equation that can model non-linear ultrasound beam distortion in a way that does not depend on propagation direction, i.e. it can form the basis for a full-wave computation, as opposed to a (partial/forward)-wave computation, as, say, the *KZK* Equation does.

$$\left(\nabla^2 - \frac{1}{c_e^2}\frac{\partial^2}{\partial t^2}\right)p = -\frac{\beta}{\rho_e c_e^4}\frac{\partial^2 p^2}{\partial t^2} + \nabla\cdot\mathbf{f} - \rho_e\partial_t q, \tag{2.9}$$

An important difficulty with all full-wave methods of simulating non-linear ultrasound in the time domain, is the fine grid discretization needed to accommodate high frequencies. The *Iterative Nonlinear Contrast Source* (INCS) method [87, 88, 89, 90] is designed primarily to solve Eq. 2.9 in a way that addresses this difficulty, by performing iterative convolutions of the contrast source, $\hat{S} = -\frac{\beta}{\rho_e c_e^4}\frac{\partial^2 p^2}{\partial t^2}$ with the Green's function for the left-hand side of Eq. 2.9, *after both they and* S_t have been filtered to a pre-determined maximum frequency of interest. The iterative process is formally equivalent to Liouville-Neumann iteration, or *the method of successive approximations* [91],

$$\begin{aligned}\left(\nabla^2 - \frac{1}{c_e^2}\frac{\partial^2}{\partial t^2}\right) p &= S_t + \hat{S}(p) \\ p^0 &= G * S_t \\ p^{i+1} &= p^0 + G * \hat{S}(p^i)\end{aligned}$$

This method converged to a p-field that agreed well with two partial-wave calculation methods and a FD method in, typically, less than five iterations. It's main drawback is the need to store the entire pressure field $p(\mathbf{x}, t)$ at all iterations, which led [90] to large computation times on a desktop computer with 2GB of RAM (up to 130hrs) due the need to repeatedly access the hard-disk.

2.4.3 Pseudo-spectral and *k*-space methods

Whether solving a linear or a non-linear equation, FD and FE methods suffer from the need to discretize spatial grids finely (typically 10-20 PPW) for waves at high frequencies, since they model the waveform by fitting low order polynomial functions to adjacent grid points using only local information. Two important branches of alternative methods fit a *Fourier series* to all grid points simultaneously, enabling a coarser gridding down to 2 PPW. In a simple case this amounts to solving Eq. 3.13 after a *spatial* Fourier transform,

$$(ck)^2 \tilde{p}_k + \frac{d}{dt}\tilde{p}_k = \tilde{S}_k(t). \tag{2.10}$$

Pseudospectral time domain (PSTD) methods and k-space methods differ in the way they handle the temporal gradients [92, 93, 94]. Whereas PSTD methods use a FD time gradient, *k*-space methods use an approximate analytical expression for the time derivative that allows larger time steps to be used without loss of accuracy. The MATLAB *k-Wave* Toolbox is based on such a method, and now incorporates the ability to model power law absorption and non-linearity [95, 96].

2.5 Image-based registration of ultrasound to images of other modalities

The locations of interfaces between different organs are more precisely and accurately seen, provided they are visible, in images of high resolution *anatomical* modalities, such as magnetic resonance (MR) or computed tomography (CT) than in B-mode ultrasound (US), due to the characteristic artifacts and relatively low spatial resolution of US and artifacts such as speckle and image aberrations. The geometrical model needed to simulate ultrasound wave propagation, as will be described in Chapter 3, is therefore more accurately derived from segmenting an MR or CT image. An appropriate approach to establishing spatial correspondence between this model and data from a B-mode US probe is then to align, or *register*, the anatomical image to a B-mode US image acquired in the same orientation, with respect to the patient, as the data of interest. Image registration is a wide field of research and *multi-modality* registration is a particularly challenging area [97] [98]

An image may be modelled, mathematically, as an intensity-valued function of spatial position, where, for example, an image I may have intensity $I(\mathbf{x}_i)$ at a pixel or voxel whose spatial coordinates, in some reference frame "native" to I are held in $\mathbf{x}_i \in \Omega_I \subset \mathbb{R}^n$, where $n = 2$ or 3 for a 2D or 3D image, respectively.

$$I : \Omega_I \to \mathbb{R}$$

Within a framework to register two images, a spatial transformation, $\mathcal{T}$ is typically sought which deforms one image in order to maximise its spatial correspondence to the other image. The image to be deformed is often referred to as the *template* image, and the other the *reference* image. These roles are denoted by T and R below, so that

$$\mathcal{T} : \mathbb{R}^n \to \mathbb{R}^n$$

and similarity between $R(\mathbf{x})$ and $T(\mathcal{T}(\mathbf{x}))$ is maxmimised over $\mathbf{x} \in \Omega_R \cap \Omega_{T \circ \mathcal{T}}$. The transformation $\mathcal{T}$ may, in some cases, be parametrized by some finite vector of parameters ζ. For example, in the case of a rigid transformation, a suitable ζ may comprise n displacements and n angles. The similarity criterion is frequently a function of certain *features* obtained *using* T and R.

The simplest possible feature that may be extracted from an image is the unprocessed, grey-level intensity. A registration method in which a similarity function, S (of raw intensity), is optimised, with respect to the parameters, ζ, of a transformation, would usually be called a "voxel-based" method. A method which required manual delination by an expert, of anatomical structures from images, followed by similarity optimisation for a relatively simple functional form of S would usually be called "feature-based". Because of their ability to operate with minimal user interaction (other than choice of initial parameters, ζ_0, and *region of interest* (ROI)), voxel-based methods are preferred in principle for time-critical applications such as procedural guidance [99].

Since the way that intensity represents anatomy in ultrasound is very different from that of other modalities, the choices of feature and similarity metric are crucial for registration between an US image and an image of a different, high-resolution anatomical modality. This application will be referred to as "the US-MR/CT' problem" from now on. Features are generally either chosen from the MR or CT image so as to deliberately facilitate comparison with raw ultrasound intensity, or equivalent features

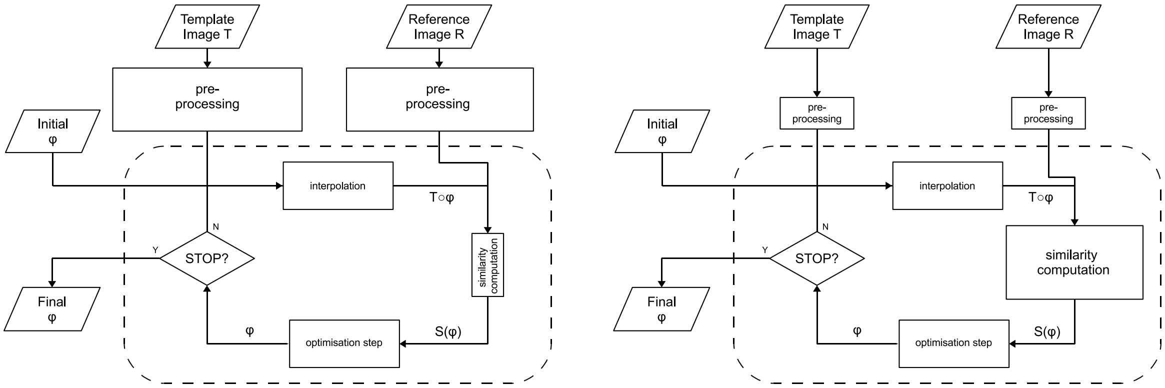

(a) feature-based

(b) voxel-based

Figure 2.13: Schematic representations of image registration approaches

derived from both US and MR/CT to enable comparison on a common feature. These choices allow a further natural division of voxel-based methods, as shown in tables 2.2 and 2.3.

2.5.1 Methods driven by modality-independent features

The most obvious choice of registration basis is raw voxel intensity, $I(x_i)$. A similarity measure capable of handling the widely different intensity characteristics between the modalities is needed, and mutual information [100] between a given pair of images $X(x_k)$ and $Y(x_k)$ has been a popular choice, e.g. [101, 102].

$$I(X,Y) = \sum_{i \in X} \sum_{j \in Y} p(X=i, Y=j) \log \left(\frac{p(X=i, Y=j)}{p(X=i)p(Y=j)} \right) \tag{2.11}$$

Here, the $p(\cdot)$s denote probability distributions over intensity values i and/or j. Mutual information (MI) captures *statistical* dependence between the intensities of X and Y without assuming a *functional* dependence. The assumption of the MI registration criterion is essentially that, at the correct registration pose, a certain, relatively low number of intensity pairings $(Y(\mathbf{x}_i), (X \circ \mathcal{T})(\mathbf{x}_i))$ will occur with relatively high frequency.

Mutual information is affected by the *size* of the overlapping region $\Omega_{X \circ \mathcal{T}} \cap \Omega_R$ as well as on the quality of the alignment within it, potentially introducing a bias toward strong overlap. Normalised mutual information (NMI) ([100, 103]) is independent of this size, dealing with the problem. Equations describing NMI appear in Sec. 5.2.3.

In [101], Pagoulatos et al. used an intensity NMI-driven registration as part of a hybrid scheme to rigidly register small numbers of ultrasound slices to an MR volume of a phantom. Voxel-based registration was initialised from pertubations with respect to a ground truth pose from fiducial marker tracking. The mean registration error was (1.88 ± 0.42)mm, an impressive result for US-MR registration, but the phantom suffered no deformation between MR and US acquisitions and the size of the perturbations was not given. In an interventional scenario, an initialisation based on tracking is feasible, but non-invasive fiducial markers are unreliable due to skin motion, especially if the patient is breathing [104, 97]. Blackall et al. ([102]) registered sets of ultrasound slices and an MR volume of phantom, using NMI,as part of a novel US probe calibration scheme. Performance was slightly inferior, to a well-known, point-based method, with calibration errors of just over 1mm, and the method has not been pursued further to my knowledge.

The (normalised) mutual information criterion is robust with respect to modality differences, however, it can produce ’false positive’ alignments by failing to apply constraints which human perception naturally does. The characteristic *artifacts* and low signal-to-noise ratio of ultrasound images lead to local similarity maxima on uninformed statistical comparison with other modalities. By imposing an assumption of *functional* dependence between coincident intensities in the registered images, say X and Y, the local maxima of MI can be avoided ([105]). If *any* functional dependence of the form $Y(x_i) = f((X \circ \mathcal{T})(x_i))$ is assumed to exist for optimal ζ, then distance from the registration pose may be quantified by

$$\arg\min_{\mathbf{f}} \text{Var}(Y - f((X \circ \mathcal{T}))).$$

With no information about its functional form, the optimal choice for f is the conditional expectation of Y given X, yielding the *correlation ratio* (CR),

$$\eta(Y|(X \circ \mathcal{T})) = \frac{\text{Var}[E(Y|(X \circ \mathcal{T}))]}{\text{Var}(Y)} = 1 - \frac{\text{Var}[Y - E(Y|(X \circ \mathcal{T}))]}{\text{Var}(Y)}.$$

This measure performed well compared to MI, and other criteria in multimodality rigid registration between MR, CT and PET brain images, and was robust with respect to sub-sampling of the images. No results from the group have appeared on using CR for US-X registration, but [106] explains why it wouldn’t work and puts forward a modification. The modified criterion, *bivariate* correlation ratio, takes into account the superficial characteristics of ultrasound images [107].

The unique *intensity* characteristics of a B-mode ultrasound image challenges attempts to automatically recognise corresponding *anatomical* features shared with another image. However, the *local phase* of an image can parametrize the presence of different *types* of object features, e.g. edges, blobs, independently of their intensity and orientation [108, 109, 110, 111, 112]. Applications to multi-modal non-rigid registration with MR and synthetic ultrasound of brain [109, 110] performed well compared to equivalent intensity-based techniques, but I am not aware of its use with real ultrasound.

By using the similarity measure constructed from both local phase and local *orientation* given by Eq. 2.12 for spatio-temporal images I_1 and I_2, and transformation $\mathcal{T}$, Grau et al. [113] have rigidly registered apical and parasternal ultrasound heart sequences to within a TRE of 2mm in

published	author (et al.)	feature	similarity measure	search space	search strategy
2009	Milko	vessel prob.	weighted product	rigid	Powell
2009	Legg	multiscale gradient magnitude	MI	rigid	manual search (rotations), Nelder-Mead simplex (translations)
2007	Dalvi	local phase	MI	rigid	visual, followed by constrained manual search
2006	Haber	normalised gradient	dot product	non-rigid	Gauss-Newton
2005	Blackall	vessel prob.	cross-correlation	rigid then B-spline displacements constrained by breathing to 1D	zeroth-order estimation then 1D search
2005	Jian	local freq.	Gaussian density of differences	B-spline displacements	nonlinear quasi-newton and pre-conditioned gradient descent
2004	Penney	vessel prob.	NCC	rigid	zeroth-order estimation scheme
2000	Blackall	intensity	NMI	semi-affine	multi-resolution search
1998	Roche	intensity	CR	rigid	Powell

Table 2.2: Intensity-based registration approaches for US-MR/CT driven by intensity-derived features which are *modality-independent*.

85% of trials, and 5mm for 100%. Though not a multi-modal problem, the presence of view-dependent image artifacts makes this, nonetheless, an impressive result. In the expression, $W(\mathbf{r},t) = \min(\sin^2(\zeta(I_1(\mathbf{r},t),s)), \sin^2(\zeta(I_2(\mathbf{r},t),s)))$ and s is a wavelength characteristic of a filtering operation involved in the calculation of the local phase, $\zeta(\cdot)$, of an image location $I(\mathbf{r},t)$. See App. F for details of this calculation and that of local orientation, $o(\cdot)$. In Eq. 2.12, the voxel locations belong to the image overlap region $\mathbf{r} \in \Omega_{I_1} \cap \Omega_{I_2}$, μ is a weighting scalar, and $N_{\mathbf{r}} = |\Omega_{I_1} \cap \Omega_{I_2}|$.

$$S(\mathcal{T}) = \sum_t \frac{\sum_{\mathbf{r}} W(\mathbf{r},t)[1 - o(I_1(\mathbf{r},t),s) \cdot o(I_2(\mathbf{r},t),s)]}{\sum_{\mathbf{r}} W(\mathbf{r},t)} + \mu \sum_t \frac{\sum_{\mathbf{r}}[1 - \cos(\zeta(I_1(\mathbf{r},t),s) - \zeta(I_2(\mathbf{r},t),s))]}{N_{\mathbf{r}}} \qquad (2.12)$$

Pre-processing of the images to be registered may, of course, seek to extract an anatomical feature, rather than an abstract one. In a rigid liver application, Penney et al. [114], process MR and US differently to produce vessel probability maps. Similarity is computed between the maps for a particular registration pose with the normalised cross-correlation (NCC) metric.

published	author (et al.)	feature	similarity measure	search space	search strategy
2009	Gill	(sim/real) US intensity	BCLC^2	rigid $\times n_{\text{vertebrae}}$	CMA-ES
2009	King	(prob/real) US intensity	likelihood	rigid	simple hill-climbing
2009	Kutter	(sim/real) US intensity	NCC	rigid	downhill simplex
2008	Wein	(sim/real) US intensity	LC^2	semi affine	amoeba simplex
2007	Wein	(sim/real) US intensity	LC^2	rigid	simple hill-climbing/Powell-Brent/exhaustive hill-climbing
2005	Wein	edges regions	correlation MI	rigid	simple hill-climbing/Powell-Brent/exhaustive hill-climbing
2001	King	liver surface	posterior prob.	rigid with breathing prior	MAP

Table 2.3: Intensity-based image registration approaches for US-MR/CT driven by intensity-drived features which *imitate ultrasound*. Biomechanically-constrained linear Correlation of Linear Combination (BCLC^2). Covariance Matrix Adaptation Evolution Strategy (CMA-ES). Maximum *A Posteriori* Probability (MAP)

2.5.2 Methods driven by ultrasound-imitating features

Since ultrasound image artifacts are highly dependent on the pose of the FOV with respect to anatomy, which is the independent variable of any rigid registration algorithm, this dependence can be exploited to enable a closer correspondence between intra-operative ultrasound and pre-operative images in registration; essentially, US characteristics are *simulated* from the CT or MR to improve similarity to the US image [115, 116, 117, 118, 119, 120].

Of particular interest for liver applications is the highly successful *linear combination of linear correlation* (LC^2) criterion adopted by Wein et al. [115, 116, 117]. A greatly simplified physical model of ultrasound imaging is combined with, arguably, a “tri-variate” extension to the *bivariate* correlation ratio of Roche et al. [107]. Refer to Sec. 5.2.3 for details of the method.

While this method achieved Target Registration Errors (TREs) of around 1mm in [116], there remain methodological questions about the occlusion of regions behind strongly reflecting interfaces. The echogenicity, p, is computed from μ, via a cubic polynomial mapping estimated from a few soft tissues, and would be extremely high for bone if bony regions were not excluded from the computation. This is dealt with in [115, 121], and later by Gill et al. for a spine application in [120], but not in [116].

Milko et al. have performed a comparison [122] of six criteria for rigid US-to-MR liver registration.

The criteria were combinations of mutual information or correlation ratio measures with US intensity and either MR intensity or gradient data, motivated by the broad observation that most B-mode US information is contained in interface reflections. Correlation ratio between US intensity and MR gradient norm outperformed the other metrics in terms of robustness, whilst maintaining good accuracy. However, comparison with other approaches in the literature is not straightforward, since accuracy was measured for each transformation parameter, rather than as a target registration error (TRE).

To the best of my knowledge, no comparison including the most popular registration criteria has been done for abdominal US-MR/CT applications. Crucially, such a comparison should test different criteria with the same data sets, and assess performance in the same manner.

Chapter 3

Recovery of acoustic properties in multi-compartment media

3.1 Introduction

3.1.1 Overview

Section **??** reviews the *adjoint state method* in a general setting, which is used in this chapter. Section 3.2 begins by summarising the numerical phantom experiments presented and explaining the rationale behind them, before giving full experimental details. The results are then discussed and conclusions drawn.

3.1.2 Purpose

Acoustic properties of human tissues, such as sound speed, c, density, ρ, absorption coefficient, μ_a, and non-linearity parameter, B/A, are of some interest for both diagnostic and engineering reasons. While diagnostic B-mode ultrasound imaging indicates impedance changes in a complicated and semi-quantitative fashion, the technique is not designed to quantitatively estimate any acoustic parameter, and alternative ultrasound processing techniques have arisen for quantitative parameter estimation or imaging in applications *ex vivo* and *in vivo*.

Conventional methods for measuring acoustic tissue properties, such as absorption, μ_a, attenuation μ, sound speed c, backscatter μ_{bs} and nonlinearity B/A, involve delicate temperature, voltage or time-of-flight (TOF) measurements on accurately prepared *ex vivo* tissue samples as described in Sec. **??** e.g. [56, 123, 124]. Several of these parameters have been shown to correlate with disease state of tissue, notably in the liver, prompting interest in *in vivo* measurement methods.

To my knowledge, it is not yet known how accurate an estimate of sound speeds, densities, absorptions, backscatters and non-linearities is needed for abdominal HIFU planning based on full-wave simulations. Nor are results on the inter-patient variability of such tissue parameters widely documented. Though the current clinical standard for HIFU planning typically involves an attenuation correction based on literature values, and no actual modelling, other scenarios where full-wave modelling is highly desirable, such as *trans-costal* HIFU, are under development. For these applications, the question of the superiority of patient-specific parameter estimatesover *ex vivo* literature values merits investigation. In this work, I have investigated the prinicple of a non-invasive *in vivo* technique using numerical phantom data. The reference, or "surrogate" data are obtained using a simulated diagnostic ultrasound probe, spatially co-registered to the patient phantom.

3.1.3 Related work

This work is based in the *full waveform inversion* family of seismic tomography methods as described in Chap. 2. The nearest published work is probably that of Liu et al. [125], Luo et al. [126] and Tarantola [127].

3.1.4 Modelling Sound propagation

The propagation of sound, generally of multiple frequencies, in a fluid can be described by an appropriate wave equation. Two important *field variables* are the *pressure*, P and *velocity*, $\mathbf{U}$ of the fluid medium, which depend on time and position as

$$P(\mathbf{x},t) = P_0(\mathbf{x}) + p(\mathbf{x},t) \qquad\qquad \mathbf{U}(\mathbf{x},t) = \mathbf{U}_0(\mathbf{x}) + \mathbf{u}(\mathbf{x},t)$$

Here, P_0 and $\mathbf{U}_0$ are the *ambient* pressure and velocity distributions that the medium would have in the absence of any sound waves. The perturbations p and $\mathbf{u}$ are called *acoustic variables*. Density, $\rho(\mathbf{x},t)$, will also contain perturbations about some equilibrium value, $\rho_0(\mathbf{x})$, for a given medium location. In this thesis, the acoustic media are assumed to be *quiescent*, i.e. to have background properties which do not change in time. An acoustic *wave equation* is a partial differential equation that describes the behaviour of an acoustic variable in the presence of a sound wave. One of the assumptions made in this work was that, regions of the tissue media in which waves propagate which are *homogeneous* are also *isotropic*, that is, sound propagates identically in all directions. Hence, the scalar *acoustic pressure*, p, is the acoustic variable of interest in this thesis.

Ultrasound waves employed in medical imaging, as distinct from HIFU, may be assumed to be of small amplitude, that is $p \ll P_0$. The wave equation describing small-amplitude pressure waves within a homogeneous, lossless fluid medium can be derived by beginning with conservation equations for mass and momentum (REFER TO APPENDIX):

$$\frac{D\rho}{Dt} + \rho\,(\nabla \cdot \mathbf{U}) = 0 \qquad (3.1) \qquad\qquad \frac{D(\rho\mathbf{U})}{Dt} + \rho\mathbf{U}\,(\nabla \cdot \mathbf{U}) = -\nabla P + \mathbf{g}\rho \qquad (3.2)$$

To obtain a combined equation in terms of pressure, the relationship between pressure and density in the material is needed. This is provided by an *equation of state*, which, in a general form linking pressure, density and entropy, takes the form

$$\begin{aligned} P &= P_0 + \left.\frac{\partial P}{\partial \rho}\right|_{s,\rho_0} (\rho - \rho_0) + \frac{1}{2!}\left.\frac{\partial^2 P}{\partial \rho^2}\right|_{s,\rho_0} (\rho - \rho_0)^2 + \frac{1}{3!}\left.\frac{\partial^3 P}{\partial \rho^3}\right|_{s,\rho_0} (\rho - \rho_0)^3 + \ldots \\ &= P_0 + \rho_0 \left.\frac{\partial P}{\partial \rho}\right|_{s,\rho_0} \left(\frac{\rho - \rho_0}{\rho_0}\right) + \frac{1}{2!}\rho_0^2 \left.\frac{\partial^2 P}{\partial \rho^2}\right|_{s,\rho_0} \left(\frac{\rho - \rho_0}{\rho_0}\right)^2 + \frac{1}{3!}\rho_0^3 \left.\frac{\partial^3 P}{\partial \rho^3}\right|_{s,\rho_0} \left(\frac{\rho - \rho_0}{\rho_0}\right)^3 + \ldots \end{aligned} \tag{3.3}$$

Conventionally ([128]) the coefficients in this expansion are named so that

$$P = P_0 + A\left(\frac{\rho - \rho_0}{\rho_0}\right) + \frac{B}{2!}\left(\frac{\rho - \rho_0}{\rho_0}\right)^2 + \frac{C}{3!}\left(\frac{\rho - \rho_0}{\rho_0}\right)^3 + \ldots \tag{3.4}$$

The speed of sound is defined by

$$c^2 \equiv \left.\frac{\partial P}{\partial \rho}\right|_s . \tag{3.5}$$

If the waves are assumed to propagate *adiabatically*, i.e. without transfer of heat, then the entropy in any part of the medium will remain constant, so that Eq. 3.1 becomes

$$\begin{aligned} \frac{\partial \rho}{\partial P}\frac{DP}{Dt} + \rho \nabla \cdot \mathbf{U} = 0 \\ \frac{DP}{Dt} + \rho c^2 \nabla \cdot \mathbf{U} = 0. \end{aligned} \tag{3.6}$$

This can be linearlised in the acoustic perturbations as follows:

$$\begin{aligned} \frac{D(P_0 + p)}{Dt} + (\rho_0 + \rho')(c_0 + c')^2 \nabla (\mathbf{U}_0 + \mathbf{u}) = 0 \\ \frac{\partial (P_0 + p)}{\partial t} + (\mathbf{U}_0 + \mathbf{u}) \cdot \nabla (P_0 + p) + (\rho_0 + \rho')(c_0 + c')^2 \nabla (\mathbf{U}_0 + \mathbf{u}) = 0 \\ \cancelto{0}{\left[\frac{\partial P_0}{\partial t} + \mathbf{U}_0 \cdot \nabla \rho_0 + \rho_0 c_0^2 \nabla \cdot \mathbf{U}_0\right]} + \frac{\partial p}{\partial t} + \mathbf{U}_0 \cdot \nabla p + \mathbf{u} \cdot \nabla P_0 + \cancelto{0}{\left[(\rho' c_0^2 + 2\rho_0 c_0 c')\nabla \cdot \mathbf{U}_0\right]} + \rho_0 c_0^2 \nabla \cdot \mathbf{u} = 0, \end{aligned}$$

so that

$$\frac{\partial p}{\partial t} + \rho_0 c_0^2 \nabla \cdot \mathbf{u} = 0, \tag{3.7}$$

where the two cancellations are, respectively, due to the equation holding in the ambient state, and to the absence of ambient flow, i.e. $\mathbf{U}_0 = 0$.

Meanwhile, the momentum conservation equation, Eq. 3.2, with the help Eq. 3.1, becomes Euler's equation:

$$
\begin{aligned}
\frac{D(\rho\mathbf{U})}{Dt} + \rho\mathbf{U}\nabla\cdot\mathbf{U} &= -\nabla P + \mathbf{g}\rho \\
\rho\frac{D\mathbf{U}}{Dt} + \mathbf{U}\frac{D\rho}{Dt} + \rho\mathbf{U}\nabla\cdot\mathbf{U} &= -\nabla P + \mathbf{g}\rho \\
\rho\frac{DU}{Dt} + \mathbf{U}\cancelto{=0}{\left[\frac{D\rho}{Dt} + \rho\nabla\cdot\mathbf{U}\right]} &= -\nabla P + \mathbf{g}\rho \\
\rho\frac{D\mathbf{U}}{Dt} &= -\nabla P + \mathbf{g}\rho.
\end{aligned}
\tag{3.8}
$$

Neglecting the effects of gravity, this too can be linearised in the acoustic variables, as follows:

$$
\begin{aligned}
(\rho_0+\rho')\frac{D(\mathbf{U}_0+\mathbf{u})}{Dt} &= -\nabla(P_0+p) \\
(\rho_0+\rho')\left[\frac{\partial(\mathbf{U}_0+\mathbf{u})}{\partial t} + \big((\mathbf{U}_0+\mathbf{u})\cdot\nabla\big)(\mathbf{U}_0+\mathbf{u})\right] &= -\nabla(P_0+p) \\
\cancelto{=0}{\rho'\frac{\partial\mathbf{U}_0}{\partial t}} + \cancelto{=0}{\rho'(\mathbf{U}_0\cdot\nabla)\mathbf{U}_0} + \rho_0\frac{\partial\mathbf{u}}{\partial t} + \cancelto{=0}{\rho_0(\mathbf{U}_0\cdot\nabla)\mathbf{u}} + \cancelto{=0}{\rho_0(\mathbf{u}\cdot\nabla)\mathbf{U_0}} &= \cancelto{=0}{-\nabla P_0} - \nabla p.
\end{aligned}
$$

In the last line above, only linear terms have been retained, and the cancellations are due to the absence of ambient flow and of ambient pressure gradients, so that

$$
\rho_0\frac{\partial\mathbf{u}}{\partial t} + \nabla p = 0. \tag{3.9}
$$

To combine this with Eq. 3.7 we divide by ρ_0 and take the divergence

$$
\nabla\cdot\frac{\partial\mathbf{u}}{\partial t} + \nabla\cdot\left(\frac{1}{\rho_0}\nabla p\right) = 0 \tag{3.10}
$$

while differentiating Eq. 3.7 with respect to time:

$$
\frac{\partial^2 p}{\partial t^2} + \rho_0 c_0^2\frac{\partial}{\partial t}\nabla\cdot\mathbf{u} = 0. \tag{3.11}
$$

Finally, on substituting Eq. 3.10 into Eq. 3.11,

$$
\frac{\partial^2 p}{\partial t^2} - \rho_0 c_0^2\nabla\cdot\left(\frac{1}{\rho_0}\nabla p\right) = 0, \tag{3.12}
$$

and, if the medium is also homogeneous,

$$
\frac{\partial^2 p}{\partial t^2} - c_0^2\nabla^2 p = 0. \tag{3.13}
$$

If the wave amplitude is *not* small, i.e. if p is comparable in size to P_0, and $\mathbf{u}$ is comparable in size to c_0, then the resulting wave equation is *nonlinear* in the acoustic variable or its derivatives, and the wave propagation it describes is also said to be nonlinear. The physical implications for the propagation arise in two ways. First, still assuming that $\mathbf{U}_0 = \mathbf{0}$, and recalling that c is the speed with respect to a *stationary* medium, the velocity of the wave at any point in space and instant in time varies according to

$$\left|\frac{d\mathbf{x}}{dt}\right| = c + u \tag{3.14}$$

where $u = |\mathbf{u}|$. This effect, where the wave begins to ’carry its own medium along’ is called *convective nonlinearity*.

Additionally, if $|\rho - \rho_0|$ is an appreciable fraction of ρ, c itself will no longer be approximated by $c_0 = \partial p / \partial \rho|_{s,\rho_0}$, and will begin to vary depending upon particle velocity. To derive an expression for this dependence, consider Eq. 3.5 together with 3.4:

$$\begin{aligned}
c^2 &= \frac{A}{\rho_0} + \frac{B}{\rho_0}\left(\frac{\rho - \rho_0}{\rho_0}\right) + \frac{C}{2!\rho_0^2}\left(\frac{\rho - \rho_0}{\rho_0}\right)^2 + \dots && (3.15)\\
&\approx \frac{A}{\rho_0}\left(1 + \frac{B}{A}\frac{\rho - \rho_0}{\rho_0}\right) && (3.16)\\
&\approx \frac{A}{\rho_0}\left(1 + \frac{B}{A}\frac{u}{c}\right). && (3.17)\\
& && (3.18)
\end{aligned}$$

Here I have used the relation $u/c = |\mathbf{u}|/c \approx (\rho - \rho_0/\rho_0)$ from [129]. Since this relation is valid only for $\rho - \rho_0 \ll \rho_0$, where $c \approx c_0$, and noting, via Eq. 3.5 that $A = \rho_0 c_0^2$,

$$c = c_0\left(1 + \frac{B}{A}\frac{u}{c_0}\right)^{1/2} \approx c_0\left(1 + \frac{B}{2A}\frac{u}{c_0}\right) = c_0 + \frac{B}{2A}u = c_0 + \beta u. \tag{3.19}$$

Hence, to second order in the acoustic variables p and ρ',

$$\left|\frac{d\mathbf{x}}{dt}\right| = c_0 + (1 + \beta)u. \tag{3.20}$$

3.1.5 The Adjoint State method

The *adjoint state method* for calculating the gradient of a summed-squared-residuals cost function for acoustic tomography is presented here in a general format, following Plessix et al. [130]. Given a vector of medium parameters, ϕ belonging to some space of possible parameters, $\mathbf{\Phi}$, and a *field variable* (e.g. pressure, p) belonging to a function space, Q, we can write a model-to-data error functional and a wave equation, respectively, as

$$\mathcal{E}(\boldsymbol{\phi}) = h(p(\boldsymbol{\phi}), \boldsymbol{\phi}) \tag{3.21}$$

$$F(p(\boldsymbol{\phi}), \boldsymbol{\phi}) = 0. \tag{3.22}$$

Here, $\mathcal{E}$, F and h are functionals that map

$$\begin{aligned} F &: Q \times \mathbf{\Phi} \to Q \\ h &: Q \times \mathbf{\Phi} \to \mathbb{R} \\ \mathcal{E} &: \mathbf{\Phi} \to \mathbb{R}, \end{aligned}$$

For example, in the case of a linear least-squares problem, we have, for data d,

$$\begin{aligned} F(p(\boldsymbol{\phi}), \boldsymbol{\phi}) &= p - A\boldsymbol{\phi} \\ h(p, \boldsymbol{\phi}) &= \frac{1}{2}||p - d||^2. \end{aligned}$$

Suppose that Q is a Hilbert space of time-dependent square-integrable functions on a spatial domain $\Omega \subset \mathbb{R}^k$, and that $\boldsymbol{\phi} = (\phi_1, \phi_2, \ldots, \phi_n)$ where each ϕ_i is a square-integrable function defined on Ω. Then $Q = L^2(\Omega \times [0, T])$ and $\Phi = (L^2(\Omega))^n$ and they are equipped with the inner products

$$\begin{aligned} \langle f, g \rangle_Q &:= \int f(\mathbf{r}, t) g(\mathbf{r}, t)\, d^3r\, dt, \\ \langle \phi, \psi \rangle_\Phi &:= \sum_{i=1}^{n} \int \phi(\mathbf{r}, t) \psi(\mathbf{r}, t)\, d^k r \end{aligned}$$

In the adjoint field method one finds, for some particular parameter $\phi_i(\mathbf{r})$ an expression for $\partial\mathcal{E}/\partial\phi_i(\mathbf{r})$ in terms of a computed field, p, and another field variable, $\tilde{p}$, to be defined shortly. On perturbing the medium parameters by an amount $\delta\boldsymbol{\phi}$, F becomes

$$\begin{aligned} F(p + \delta p, \boldsymbol{\phi} + \delta\boldsymbol{\phi}) &= 0 \\ F(p, \boldsymbol{\phi}) + \langle \partial_p F(p, \boldsymbol{\phi}), \delta p \rangle_Q + \langle \partial_{\boldsymbol{\phi}} F(p, \boldsymbol{\phi}), \delta\boldsymbol{\phi} \rangle_\Phi + \mathcal{O}(||(\delta p, \delta\boldsymbol{\phi})||^2) &= 0, \end{aligned} \tag{3.23}$$

so that, with 3.22,

$$\langle \partial_p F(p, \boldsymbol{\phi}), \delta p \rangle_Q = -\langle \partial_{\boldsymbol{\phi}} F(p, \boldsymbol{\phi}), \delta\boldsymbol{\phi} \rangle_\Phi + \mathcal{O}(||(\delta p, \delta\boldsymbol{\phi})||^2). \tag{3.24}$$

Also,

$$\begin{aligned}\mathcal{E}(\boldsymbol{\phi}+\delta\boldsymbol{\phi}) &= h(p+\delta p, \boldsymbol{\phi}+\delta\boldsymbol{\phi}) \\ &= h(p,\boldsymbol{\phi}) + \langle \partial_p h(p,\boldsymbol{\phi}), \delta p\rangle_Q + \langle \partial_{\boldsymbol{\phi}} h(p,\boldsymbol{\phi})\delta\boldsymbol{\phi}\rangle_\Phi + \mathcal{O}(||(\delta p, \delta\boldsymbol{\phi})||^2) \\ \Rightarrow & \\ \delta\mathcal{E} &= \langle \partial_p h(p,\boldsymbol{\phi}), \delta p\rangle_Q + \langle \partial_{\boldsymbol{\phi}} h(p,\boldsymbol{\phi})\delta\boldsymbol{\phi}\rangle + \mathcal{O}(||(\delta p, \delta\boldsymbol{\phi})||^2) \end{aligned} \tag{3.25}$$

where $||\cdot||$ is a norm defined on $Q\times\Phi$. The space of highest dimension by far here is Q, so that, to make a computation of $\delta\mathcal{E}$ tractable, one uses 3.24 to remove the dependence on δp from

$$\delta\mathcal{E} = -\left\langle \partial_p h(p,\boldsymbol{\phi}), \left\langle (\partial_p F(p,\boldsymbol{\phi}))^{-1}, \langle \partial_{\boldsymbol{\phi}} F(p,\boldsymbol{\phi}), \delta\boldsymbol{\phi}\rangle_\Phi \right\rangle_Q \right\rangle_Q + \langle \partial_{\boldsymbol{\phi}} h(p,\boldsymbol{\phi}), \delta\boldsymbol{\phi}\rangle_\Phi$$

Finally, to remove derivatives with respect to p, the *adjoint field*, $\tilde{p}$ is introduced as the solution to the *adjoint equation*,

$$\left\langle (\partial_p F(p,\boldsymbol{\phi}))^*, \tilde{p}\right\rangle_Q = \partial_p h(p,\boldsymbol{\phi}) \tag{3.26}$$

so that

$$\delta\mathcal{E} = -\left\langle \langle \tilde{p}, \partial_{\boldsymbol{\phi}} F(p,\boldsymbol{\phi})\rangle_Q, \delta\boldsymbol{\phi}\right\rangle_\Phi + \langle \partial_{\boldsymbol{\phi}} h(p,\boldsymbol{\phi}), \delta\boldsymbol{\phi}\rangle_\Phi$$

Equation 3.27 provides a template for calculating the derivative of $\mathcal{E}$ with respect to some $\boldsymbol{\phi}$. In the case of a functional $\mathcal{E}$ that measures only the dissimilarity between measured and modelled *signals*, which are restrictions of field variables like p onto suitable subsets of $\Omega\times[0,T]$, only the first term on the right hand side of Eq. 3.25 contributes, so that

$$\delta\mathcal{E} = -\left\langle \langle \tilde{p}, \partial_{\boldsymbol{\phi}} F(p,\boldsymbol{\phi})\rangle_Q, \delta\boldsymbol{\phi}\right\rangle_\Phi + \langle \partial_{\boldsymbol{\phi}} h(p,\boldsymbol{\phi}), \delta\boldsymbol{\phi}\rangle_\Phi . \tag{3.27}$$

3.1.6 Experimental summary and rationale

The experiments presented in this chapter were designed to investigate the feasibility of estimating density and bulk modulus in media with multiple compartments using *reflection data* acquired from a *limited angular range*. In some of the experiments, the aim was to examine the behaviour of relevant cost functions in order to understand potential problems in minimising them, and to help choose appropriate parameters for the optimisation algorithms. Table 3.2 summarizes the experiments performed, and details of the methods are given in the subsections that follow.

phantom	array	(N_j, N_k)	PDE	solver	estimating	minimising	speed constraint	optimiser	described in	results in
stripe	lines	(1,2)	Eq. 3.31	k-Wave	ρ, K	$\mathcal{E}$	–	–	Sec. 3.2.4	Fig. 3.4(a)
stripe	lines	(1,2)	Eq. 3.31	k-Wave	ρ, K	$\mathcal{E}_{\text{env}}$	–	–	Sec. 3.2.4	Fig. 3.4(b)
stripe	lines	(2,1)	Eq. 3.31	k-Wave	ρ, K	$\mathcal{E}$	–	–	Sec. 3.2.12	Fig. 3.6(a)
stripe	lines	(2,1)	Eq. 3.31	k-Wave	ρ, K	$\mathcal{E}$	–	–	Sec. 3.2.12	Fig. 3.6(b)
1D profile	end-point	(1,1)	Eq. 3.29	Alg. 1	ρ_2, ρ_3, ρ_4	$\mathcal{E}$	no	`lsqnonlin`	Sec. 3.2.9	Tab. 3.7, Fig. 3.7
1D profile	end-point	(1,1)	Eq. 3.29	Alg. 1	c_2, c_3, c_4	$\mathcal{E}$	no	`lsqnonlin`	Sec. 3.2.9	Tab. 3.8, Fig. 3.8
1D profile	end-point	(1,1)	Eq. 3.29	Alg. 1	$\rho_2, \rho_3, \rho_4, c_2, c_3, c_4$	$\mathcal{E}$	no	`lsqnonlin`	Sec. 3.2.9	Tab. 3.9, Fig. 3.9
stripe	lines	(1,2)	Eq. 3.31	k-Wave	ρ, K	$\mathcal{E}$	no	Alg. 2	Sec. 3.2.11	Fig. 3.10(a)
stripe	lines	(1,2)	Eq. 3.31	k-Wave	ρ, K	$\mathcal{E}_{\text{env}}$	no	Alg. 2	Sec. 3.2.11	Fig. 3.10(b)
stripe	lines	(2,1)	Eq. 3.31	k-Wave	ρ, K	$\mathcal{E}$	no	Alg. 2	Sec. 3.2.11	Fig. 3.12(a)
stripe	lines	(2,1)	Eq. 3.31	k-Wave	ρ, K	$\mathcal{E}_{\text{env}}$	no	Alg. 2	Sec. 3.2.11	Fig. 3.12(b)
stripe	lines	(2,1)	Eq. 3.31	k-Wave	ρ, K	$\mathcal{E}_{\text{NIM}} \rightarrow \mathcal{E}_{\text{env}} \rightarrow \mathcal{E}$	no	Alg. 2	Sec. 3.2.12	Fig. 3.13, Tab. 3.14
double stripe	lines	(1,2)	Eq. 3.31	k-Wave	ρ_1, ρ_2, K_1, K_2	$\mathcal{E}_{\text{env}}$	no	Alg. 2	Sec. 3.2.13	Fig. 3.15
stripe	lines	(1,1)	Eq. 3.31	k-Wave	ρ, K	$\mathcal{E}_{\text{env}} \rightarrow \mathcal{E}$	no	`fmincon` → Alg. 2	Sec. 3.2.12	Fig. 3.14, Tab. 3.15
double stripe	lines	(2,1)	Eq. 3.31	k-Wave	ρ_1, ρ_2, K_1, K_2	$\mathcal{E}_{\text{env}} \rightarrow \mathcal{E}$	yes	`fmincon` → Alg. 2	Sec. 3.2.14	Tab. 3.17, Fig. 3.16
circle	curvilinear	(1,5)	Eq. 3.31	k-Wave	ρ, K	$\mathcal{E}_{\text{NIM}} \rightarrow \mathcal{E}$	yes	`fmincon` → Alg. 2	Sec. 3.2.15	Tab. 3.18, Fig. 3.17
split circle	curvilinear	(1,5)	Eq. 3.31	k-Wave	ρ_1, ρ_2, K_1, K_2	$\mathcal{E}_{\text{NIM}} \rightarrow \mathcal{E}$	yes	`fmincon` → Alg. 2	Sec. 3.2.15	Tab. 3.19, Fig. 3.18

Table 3.1: Experiment list. In those entries above the horizontal dividing line, no estimation was done, and cost functions were *plotted* over parameter ranges of interest without minimising them. The cost functions are given by Eq. 3.32 ($\mathcal{E}$), Eq. 3.33 ($\mathcal{E}_{\text{env}}$) and Eq. 3.34 ($\mathcal{E}_{\text{NIM}}$). Arrows indicate changes from one optimisation phase (procedure) to another during the progress of an experiment.

3.2 Methods

3.2.1 Experimental summary and rationale

The experiments presented in this chapter were designed to investigate the feasibility of estimating density and bulk modulus in media with multiple compartments using *reflection data* acquired from a *limited angular range*. In some of the experiments, the aim was to examine the behaviour of relevant cost functions in order to understand potential problems in minimising them, and to help choose appropriate parameters for the optimisation algorithms. Table 3.2 summarizes the experiments performed, and details of the methods are given in the subsections that follow.

3.2.2 Numerical phanta

As test media, I used four phantoms - a four-compartment one-dimensional profile medium, (Fig's 3.1(a) and 3.1(b)), a “stripe” (Fig. 3.1(c)), a “double stripe” (Fig. 3.1(d)), a circle (Fig. 3.1(e)), and a “split-cricle” 3.1(f). The density and bulk modulus of the circle phantom are, respectively, 900 kg m^{-3} and 1.9981×10^9 kg $m^{-1}s^{-2}$, against a background of 1000 kg m^{-3} and 2.3716×10^9 kg $m^{-1}s^{-2}$.

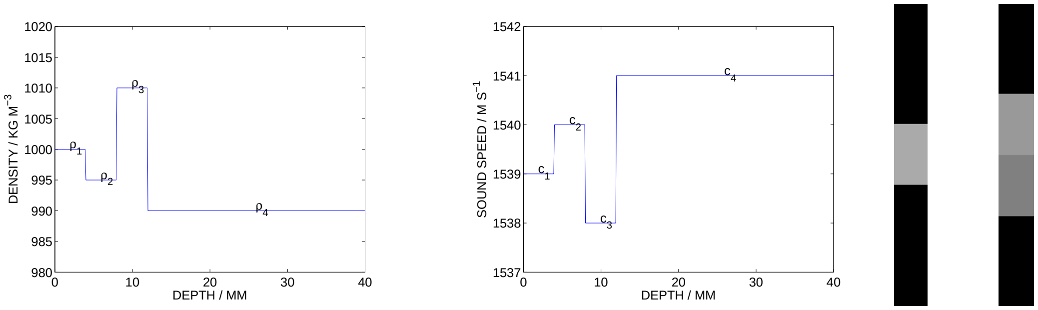

(a) 1D density profile

(b) 1D speed profile

(c) stripe

(d) ds

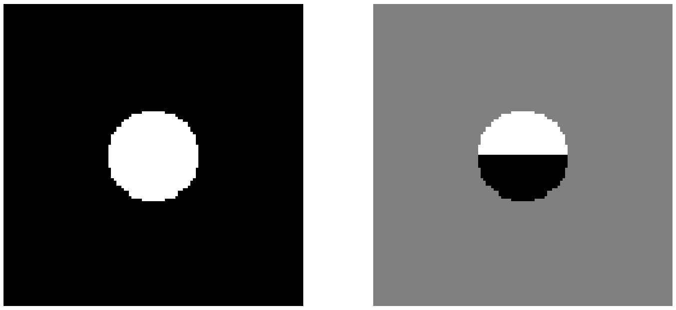

(e) circle

(f) split circle

Figure 3.1: Numerical phanta used in experiments. The “double stripe” phantom is labelled ’ds’. The ’stripe’ and ’double stripe’ phanta were 5mm × 2cm with pixel size $0.5mm^2$. The ’circle’ and ’split circle’ phanta were 20cm×20cm with pixel size $2mm^2$

phantom	array	(N_j, N_k)	PDE	solver	estimating	minimising	speed constraint	optimiser	described in	results in
stripe	lines	(1,2)	Eq. 3.31	k-Wave	ρ, K	$\mathcal{E}$	–	–	Sec. 3.2.4	Fig. 3.4(a)
stripe	lines	(1,2)	Eq. 3.31	k-Wave	ρ, K	$\mathcal{E}_{\text{env}}$	–	–	Sec. 3.2.4	Fig. 3.4(b)
stripe	lines	(2,1)	Eq. 3.31	k-Wave	ρ, K	$\mathcal{E}$	–	–	Sec. 3.2.12	Fig. 3.6(a)
stripe	lines	(2,1)	Eq. 3.31	k-Wave	ρ, K	$\mathcal{E}$	–	–	Sec. 3.2.12	Fig. 3.6(b)
1D profile	end-point	(1,1)	Eq. 3.29	Alg. 1	ρ_2, ρ_3, ρ_4	$\mathcal{E}$	no	`lsqnonlin`	Sec. 3.2.9	Tab. 3.7, Fig. 3.7
1D profile	end-point	(1,1)	Eq. 3.29	Alg. 1	c_2, c_3, c_4	$\mathcal{E}$	no	`lsqnonlin`	Sec. 3.2.9	Tab. 3.8, Fig. 3.8
1D profile	end-point	(1,1)	Eq. 3.29	Alg. 1	$\rho_2, \rho_3, \rho_4, c_2, c_3, c_4$	$\mathcal{E}$	no	`lsqnonlin`	Sec. 3.2.9	Tab. 3.9, Fig. 3.9
stripe	lines	(1,2)	Eq. 3.31	k-Wave	ρ, K	$\mathcal{E}$	no	Alg. 2	Sec. 3.2.11	Fig. 3.10(a)
stripe	lines	(1,2)	Eq. 3.31	k-Wave	ρ, K	$\mathcal{E}_{\text{env}}$	no	Alg. 2	Sec. 3.2.11	Fig. 3.10(b)
stripe	lines	(2,1)	Eq. 3.31	k-Wave	ρ, K	$\mathcal{E}$	no	Alg. 2	Sec. 3.2.11	Fig. 3.12(a)
stripe	lines	(2,1)	Eq. 3.31	k-Wave	ρ, K	$\mathcal{E}_{\text{env}}$	no	Alg. 2	Sec. 3.2.11	Fig. 3.12(b)
stripe	lines	(2,1)	Eq. 3.31	k-Wave	ρ, K	$\mathcal{E}_{\text{NIM}} \rightarrow \mathcal{E}_{\text{env}} \rightarrow \mathcal{E}$	no	Alg. 2	Sec. 3.2.12	Fig. 3.13, Tab. 3.14
double stripe	lines	(1,2)	Eq. 3.31	k-Wave	ρ_1, ρ_2, K_1, K_2	$\mathcal{E}_{\text{env}}$	no	Alg. 2	Sec. 3.2.13	Fig. 3.15
stripe	lines	(1,1)	Eq. 3.31	k-Wave	ρ, K	$\mathcal{E}_{\text{env}} \rightarrow \mathcal{E}$	no	`fmincon` → Alg. 2	Sec. 3.2.12	Fig. 3.14, Tab. 3.15
double stripe	lines	(2,1)	Eq. 3.31	k-Wave	ρ_1, ρ_2, K_1, K_2	$\mathcal{E}_{\text{env}} \rightarrow \mathcal{E}$	yes	`fmincon` → Alg. 2	Sec. 3.2.14	Tab. 3.17, Fig. 3.16
circle	curvilinear	(1,5)	Eq. 3.31	k-Wave	ρ, K	$\mathcal{E}_{\text{NIM}} \rightarrow \mathcal{E}$	yes	`fmincon` → Alg. 2	Sec. 3.2.15	Tab. 3.18, Fig. 3.17
split circle	curvilinear	(1,5)	Eq. 3.31	k-Wave	ρ_1, ρ_2, K_1, K_2	$\mathcal{E}_{\text{NIM}} \rightarrow \mathcal{E}$	yes	`fmincon` → Alg. 2	Sec. 3.2.15	Tab. 3.19, Fig. 3.18

Table 3.2: Experiment list. In those entries above the horizontal dividing line, no estimation was done, and cost functions were *plotted* over parameter ranges of interest without minimising them. The cost functions are given by Eq. 3.32 ($\mathcal{E}$), Eq. 3.33 ($\mathcal{E}_{\text{env}}$) and Eq. 3.34 ($\mathcal{E}_{\text{NIM}}$). Arrows indicate changes from one optimisation phase (procedure) to another during the progress of an experiment.

3.2.3 Data and forward models

Forward modelling is widely acknowledged to constitute the computing-time bottleneck in wave equation inversion. As a means of solving the wave equation with a given source term I initially implemented the *INCS* method, described in Sec. 2.4. This method was initially chosen because of its ability to converge in few iterations, and, looking forward, of its applicability to wave equations nonlinear in the acoustic variable. Some results using this method are presented in Sec. 3.3.1. However, the computation times turned out to be prohibitive in practice, due to the requirement to repeatedly access large arrays containing pressure at all points in the spatial and temporal intervals concerned, a point noted in [90]. The open-source *k-Wave* MATLAB toolbox uses a combined pseudo-spectral/k-space method which is suitable for linear modelling at small amplitudes and allows fewer points-per-wavelength for similar accuracy to more “traditional” methods such as finite-difference time domain solution (FDTD), leading to sped-up computation compared with these methods. Additionally it does not require storage of the acoustic variable across time points, conferring a practical speed advantage over INCS. As the capability to solve non-linear wave equations was built into the newest version of *k-Wave*, [95], it became a more viable choice of forward modelling technique, and was used for all subsequent experiments. The application of these two forward modelling techniques is described here.

In the experiments, numerical phantom media are interrogated using waves generated and received at arrays of N_k transceiver elements. A transceiver array as a whole may be placed in any of N_j positions. A receiving element has a position denoted by $\mathbf{x}_r$, and a transmitting, or source element likewise has position $\mathbf{x}_s$ where, in general, $r = 1, \ldots, N_j N_k$ and $s = 1, \ldots, N_j N_k$.

3.2.3.1 *INCS* implementation

The first set of experiments used an implementation of the INCS method with the phantom shown in Fig’s 3.1(a) and 3.1(b) to attempt to recover values of density and speed in each compartment from reflection data. The propagation is linear and lossless, and described by the wave equation Eq. 3.29, when the medium has small variations between compartments in density (a), and/or sound speed (b).

$$\left(\partial_z^2 - \frac{1}{c^2}\partial_t^2\right) p = S_t + \hat{S}(p) \tag{3.28}$$

$$\left(\partial_z^2 - \frac{1}{c^2}\partial_t^2\right) p = -\rho\,\partial_t[\Delta V \delta z] + \overbrace{\frac{1}{\rho}\partial_z \rho \partial_z p}^{\text{(a)}} + \overbrace{\left(\frac{1}{c^2} - \frac{1}{c_0^2}\right)\partial_t^2 p}^{\text{(b)}}\,. \tag{3.29}$$

The delta function here confines the contribution of the transducer excitation, S, to the front of the medium at zero depth, i.e. where $z = 0$. Under a plane wave assumption, as would hold at the transducer face, acoustic pressure, and particle velocity are related by $p = \rho_0 c_0 u_z$, where ρ_0 and c_0 denote *background* values of density and speed. With the boundary conditions for a rigid baffle applied at $z = 0$, particle velocity is also related to the velocity increment above by $\Delta V = 2u_z$, so that the excitation term, S_t, becomes

$$S_t = -2\partial_t[(p/c)|_{z=0}\,\delta(z)]. \tag{3.30}$$

Gaussian pulses were chosen for the desired input pressure $p|_{z=0}$.

The spatio-temporal filtering and windowing steps of the INCS method were applied to this source. I used analytical expressions for the relevant derivatives and Fourier transforms as far as feasible so as to avoid the need to perform numerical DFTs on large grids and sub-sample to smaller grids later. Algorithm 1 was used to compute pressure profiles in model and reference media, and hence the sum-of-squared-differences cost function $\mathcal{E}$. To compute the reference data, p_{obs}, which appear in the expression for $\mathcal{E}$ given in Eq. 3.32, I used *k-Wave*, as a convenient method independent from *INCS*.

Algorithm 1 INCS sub-algorithm to compute $\mathcal{E}(\rho_1, \rho_2, \ldots, \rho_{N_c}, c_1, c_2, \ldots, c_{N_c})$

```
set $j = 0$
repeat
    set $\delta p^i_{j+1} = G * \hat{S}(p^i_j; \zeta^i)$
    set $p^i_{j+1} = p^0 + \delta p^i_{j+1}$
    set $j = j + 1$
until $\delta p^i_j \leq p_{TOL}$
$\mathcal{E}^i = \|p^{GT} - p^i_{jfin}\|^2$
```

3.2.3.2 *k-Wave*

For experiments using *k-Wave* as a forward model computation, a curvilinear source-receiver (“Tx/Rx”) array of N_k elements, placed at varying positions and orientations in the ’0’ medium was intended to represent a diagnostic ultrasound imaging probe. Eight equally-spaced positions for the Tx/Rx array are shown, for $N_k = 5$, in Figure 3.2(c). For the stripe and double stripe phanta, a pair of line elements were used (Fig. 3.2(a)).

The wave equation used to constrain the optimisation is given by Eq. 3.31,

$$\left[\nabla \cdot \left(\frac{1}{\rho(\mathbf{x})}\nabla\right) - \frac{1}{K(\mathbf{x})}\partial_t^2\right]p = -S(\mathbf{x}, t). \tag{3.31}$$

Here, ρ is the density of the medium, and $K = \rho c^2$ is its *bulk modulus*, for sound speed c. For mathematical convenience, the two parameters recovered in the inversions described below are density and bulk modulus, for each of several compartments.

Reference data were obtained using the same model. A typical source term, $S(\mathbf{r}, t)$ was a Gaussian-modulated pulse at 500kHz, as pictured in Fig. 3.3. Dignostic pulse-echo imaging is normally carried out at pulse centre frequencies between 1 MHz and 20 MHz. This, lower value was chosen for this

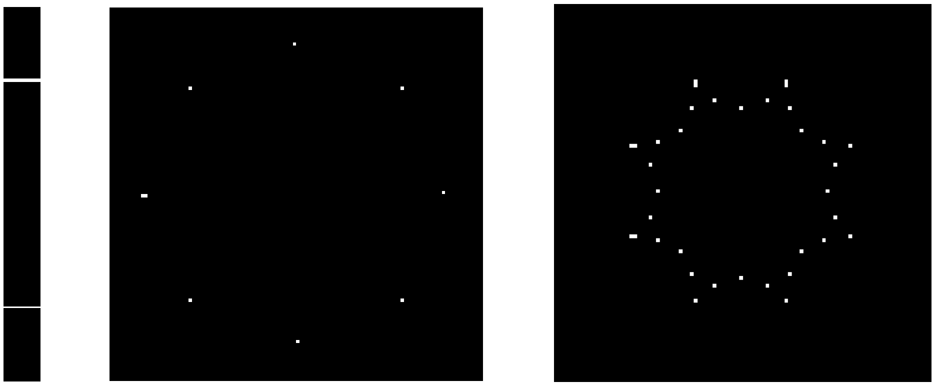

(a) lines (b) ring (c) curvilinear

Figure 3.2: Available source/receiver element positions under different array geometries. There are N_k elements in each 'probe' and N_j positions the probe can occupy. For the above, (N_k, N_j) are: (a) - (2,1), (b) - (1,8), (c) - (5,8).

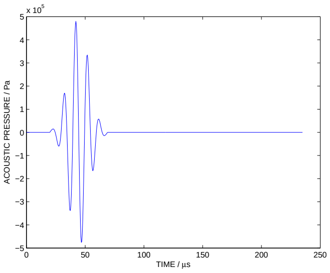

Figure 3.3: Input pressure pulse

concept demonstration work in order to reduce computation times. One of the anticipated challenges of future work – and a well-known one – is forward computation at diagnostic frequencies, owing to the large number of grid points and time steps required. However, there is not expected to be any difference in the efficacy of the methods due to the use of a low frequency beyond their speed, so that demonstration of the efficacy is still possible.

The *k-Wave* software accepts sources as additive pressure or velocity signals. For calculating the adjoint field I used an additive pressure signal defined from a model-to-data misfit (see Sec. 3.2.7).

3.2.4 Objective function and nonlinear minimisation scheme

The model parameter vector, $\boldsymbol{\phi} = \{\rho_1, \dots, \rho_{N_c}, K_1, \dots, K_{N_c}\}$ contains one value each of density and bulk modulus for each tissue compartment. Compartments are labelled with $i = 1, \dots, N_c$. In a medium characterized by acoustic properties $\boldsymbol{\phi}$, the acoustic pressure recorded at tiem t and position $\mathbf{x}_r$, resulting from an excitation at $\mathbf{x}_s$, is denoted $p(t, \mathbf{x}_r; \mathbf{x}_s, \boldsymbol{\phi})$. This will usually be abbreviated to $p_{sr}(t; \boldsymbol{\phi})$. Where $\boldsymbol{\phi}$ takes the *reference* or *true* value $\boldsymbol{\phi}^*$, p becomes the *reference* or *observed* signal, p^*, and $p_{sr}(t; \boldsymbol{\phi}^*)$ is usually (further) abbreviated to $p_{*sr}(t)$.

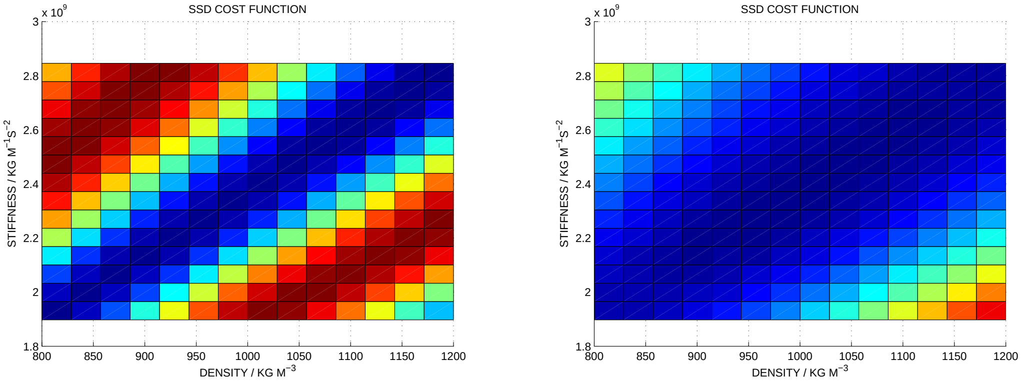

(a) $\mathcal{E}$

(b) $\mathcal{E}_{\text{ENV}}$

Figure 3.4: Cost functions in the “stripe” phantom using pressure signals in Eq. 3.32, (3.4(a)) and their envelopes in Eq. 3.33 (3.4(b))

Least-squares cost functions, Eq. 3.32, 3.33 and 3.34 quantify model misfit.

$$\mathcal{E}_{\text{SSD}}(\boldsymbol{\phi}) = \frac{1}{2}\sum_s \sum_r \int_0^T w_{sr}\Big[p_{sr}(t;\boldsymbol{\phi}) - p^*_{sr}(\mathbf{x}_r, t)\Big]^2 dt. \tag{3.32}$$

There are N_j array positions and N_k transceiver elements in the array, as shown in Fig. 3.2(c) for $N_j = 8$ and $N_k = 5$. Therefore there are $N_r = N_j N_k$ element positions in total. The two sums in Eq. 3.32 are over sources and receivers (r, s), where $r, s \in \{1, 2, \ldots, N_j N_k\}$, and a set of binary weights $\{w_{sr}\}$ with $|\{w_{sr}\}| = (N_j N_k)^2$ may be used to restrict to a subset of combinations. Different choices for $\{w_{sr}\}$ will result in different functional forms for $\mathcal{E}$, but all with the same global minimum in $\boldsymbol{\phi}$. The $\frac{1}{2}$'s are for mathematical convenience. Figure 3.4 shows plots of $\mathcal{E}$ and $\mathcal{E}_{\text{ENV}}$ with respect to medium perturbations in the central inclusion of the stripe phantom, Fig. 3.1(c), where both of the lines in Fig. 3.2(a) have been used to transmit and receive, $w_{11} = w_{12} = w_{21} = w_{22} = 1$. The “envelope” cost function, $\mathcal{E}_{\text{ENV}}$ is described by Eq. 3.33, following [125], where $E[.]$ denotes a signal envelope, as defined in App. C. The removal of the two local destructive interference maxima due to the use of the signal envelopes is clear in Fig. 3.4(b).

$$\mathcal{E}_{\text{ENV}}(\boldsymbol{\phi}) = \frac{1}{2}\sum_s \sum_r \int_0^T w_{sr}\Big[E[p_{sr}](t;\boldsymbol{\phi}) - E[p^*_{sr}](t)\Big]^2 dt. \tag{3.33}$$

Some results presented in later sections also make use of the full *Normalised Integration Method* (NIM) of [125], based on the cost function of Eq. 3.34. The relative sizes of reference and model signals always affects $\mathcal{E}_{\text{NIM}}$ irrespective of their temporal overlap, hence this cost function is not expected to suffer from “plateaux” regions of zero gradient, away from its minimum, as $\mathcal{E}_{\text{ENV}}$ does. The need for the integrated envelopes to be *normalised* arises from the initial and terminal boundary conditions of the adjoint method, and would appear to involve discarding useful amplitude information. However, if *transmitted* pulses are included together with the received ones in p and p^*, normalising two traces whose received echoes differ only in amplitude will not result in identical trances. Sections 3.3.2 and 3.3.7 present results in which this has been done, although I bear in mind that the amplitude contrast between transmitted and received ultrasound signals may be too large for this to practicable with real data.

$$\mathcal{E}_{\mathsf{NIM}}(\boldsymbol{\phi}) = \frac{1}{2}\sum_s\sum_r\int_0^T w_{sr}\Big[Q_{\mathsf{NIM}}[p_{sr}](t;\boldsymbol{\phi}) - Q[p^*_{sr}](t)\Big]^2\,dt. \tag{3.34}$$

where

$$Q[p](t) = \frac{\int_0^t E[p](t')\,dt'}{\int_0^T E[p](t')\,dt'} \tag{3.35}$$

For those experiments using the *INCS* method, minimisation of $\mathcal{E}$ was attempted using a trust-region reflective optimiser implemented in MATLAB's Optimisation Toolbox with the `fminunc` routine.

For later experiments using a *k-Wave* computation for both forward model and reference data, I implemented a conjugate gradient algorithm to minimise $\mathcal{E}$ in three different ways, dependent on how many of the source/receiver combinations are involved in each iteration. This report contains results obtained using one of them. I denote by $\mathcal{E}^{(n)}$ the version of the cost function resulting from the n^{th} restriction on $\mathcal{E}$, $\{w_{sr}\}^{(n)}$. Algorithm 2 shows how the total number, N_n of such restrictions are looped over until convergence.

This algorithm was implemented in three ways, with the results presented in Sec's 3.3.2 and 3.3.7 being produced from version iii.

i. Each iteration uses $\mathcal{E}^{(n)}$ computed from *one* probe position and *one* Tx element, i.e. $\{w_{sr}\}^{(n)} = \{\delta_{n,s}\delta_{\lfloor n/N_k\rfloor,\lfloor r/N_k\rfloor}\}$ and $N_n = N_kN_j$

ii. Each iteration uses $\mathcal{E}^{(n)}$ computed from *one* probe position and *all* Tx elements on that position, one after the other, i.e. $\{w_{sr}\}^{(n)} = \{\delta_{\lfloor n/N_k\rfloor,\lfloor s/N_k\rfloor}\delta_{\lfloor n/N_k\rfloor,\lfloor r/N_k\rfloor}\}$ and $N_n = N_j$

iii. Each iteration uses $\mathcal{E}^{(n)}$ computed from *all* probe positions and *all* Tx elements in each position, one after the other, i.e. $\{w_{sr}\}^{(n)} = \{\delta_{\lfloor r/N_k\rfloor,\lfloor s/N_k\rfloor}\}$, where $N_n = 1$

In the above, N_{pars} represents the number of quantities to be optimised, e.g. for all densities and bulk moduli in three compartments, $N_{\mathsf{pars}} = 6$.

In order to choose suitable values for *maxIter*, the maximum number of iterations and *maxLs*, the maximum number of steps in any line search, and initial values for $\alpha^{(dim)}$, rapid test optimisations were performed for each experiment in which the cost function gradient was interpolated cubically from a pre-computed "landscape".

Algorithm 2 Conjugate Gradients Minimisation of $\mathcal{E}$

```
$n = 0$
$\boldsymbol{\phi}^{(n)} = \boldsymbol{\phi}_0$
search direction $\mathbf{d}^{(n)} = \nabla\mathcal{E}(\boldsymbol{\phi}^{(n)})$
repeat
    select $n^{\text{th}}$ set of weights, $\{w_{sr}\}^{(n)}$
    $dim = 1$
    $\boldsymbol{\phi}^{(dim)} \leftarrow \boldsymbol{\phi}^{(n)}$
    repeat
        compute $\alpha^{(dim)}$ using $\mathcal{E}^{(dim)}$, i.e. perform line-search
        $\boldsymbol{\phi}^{(dim+1)} = \boldsymbol{\phi}^{(dim)} + \alpha^{(dim)}\mathbf{d}^{(dim)}$
        compute $\beta^{(dim)}$ using $\mathcal{E}^{(dim)}$
        $\mathbf{d}^{(dim+1)} = -\nabla\mathcal{E}^{(dim)}(\boldsymbol{\phi}^{(n+1)}) + \beta^{(dim)}\mathbf{d}^{(dim)}$
        $dim \leftarrow dim + 1$
    until $dim > N_{\text{pars}}$
    $\boldsymbol{\phi}^{(n)} \leftarrow \boldsymbol{\phi}^{(dim)}$
    $n \leftarrow n + 1 \pmod{N_n}$
until $\exists n : \; |\mathcal{E}^{(n)}(\boldsymbol{\phi}^{(n+1)}) - \mathcal{E}^{(n-1)}(\boldsymbol{\phi}^{(n)})| < \epsilon_{\mathcal{E}}$ or $|\boldsymbol{\phi}^{(n+1)} - \boldsymbol{\phi}^{(n)}| < \epsilon_{\boldsymbol{\phi}}$ or $n >$ maxIter
$\hat{\boldsymbol{\phi}} \leftarrow \boldsymbol{\phi}^{(n)}$
```

3.2.5 Model parameter scaling

In soft tissues, density and sound speed are typically on the same numerical order of magnitude of 10^3. However, bulk modulus is typically on the order of 10^9. The large difference between the numerical sizes of densities and bulk moduli made application of Alg. 2 difficult in early tests on estimating these two quantities simultaneously. A scaling scheme was therefore introduced for the update steps of Alg. 2 and used to appropriately modify the cost function gradient, computed as described in the next subsection, just prior to use in 2. Hence, instead of operating with $\boldsymbol{\phi}$, Alg. 2 operated with $\tilde{\boldsymbol{\phi}}$, where, for upper and lower limits $\boldsymbol{\phi}_U$ and $\boldsymbol{\phi}_L$,

$$\tilde{\boldsymbol{\phi}} = \frac{\boldsymbol{\phi} - \boldsymbol{\phi}_L}{\boldsymbol{\phi}_U - \boldsymbol{\phi}_L}. \tag{3.36}$$

In the density-bulk modulus estimation experiments presented in the rest of this chapter upper and lower values used were ρ_U = 2000kg m^{-3}, ρ_L = 500kg m^{-3}, K_U = 4.00$\times$10^9 kg m^{-1}s^{-2}, K_L = 5.0$\times$10^8 kg m^{-1}s^{-2}.

3.2.6 Stopping criteria

All estimations were subject to a maximum number of iterations, and some, additionally, to a minimum step size $\epsilon_{\tilde{\boldsymbol{\phi}}}$. Values for this tolerance on the *absolute* value of $|\tilde{\boldsymbol{\phi}}^{(n+1)} - \tilde{\boldsymbol{\phi}}^{(n)}|$ were worked out so as to effectively give a tolerance on the *relative* value of $|\boldsymbol{\phi}^{(n+1)} - \boldsymbol{\phi}^{(n)}|$ as follows.

If, for a single parameter with true value ϕ_0, an estimated value less than $\phi_0(1+\epsilon_m)$ is desired, where, for example, the relative error, ϵ_m is 0.01, for an overestimation less than 1%, then,

$$\frac{\phi_0(1+\epsilon_m) - \phi_L}{\phi_U - \phi_L} = \frac{\phi_0 - \phi_L}{\phi_U - \phi_L} + \frac{\phi_0 \epsilon_m}{\phi_U - \phi_L} \tag{3.37}$$

$$= \tilde{\phi}_0 + \frac{\phi_0 \epsilon_m}{\phi_U - \phi_L}. \tag{3.38}$$

Hence the bound on absolute error for $\tilde{m}$ is less than

$$\epsilon_{\tilde{m}} = \frac{\phi_0 \epsilon_m}{\phi_U - \phi_L}. \tag{3.39}$$

Since ϕ_0 is unknown to the optimiser, the stricter value of ϕ_L may be used in the above expression instead. For multiple parameters, we will have a relative increment in $\boldsymbol{\phi}$ with modulus less than $\epsilon_{\boldsymbol{\phi}}$ if

$$|\tilde{\boldsymbol{\phi}}^{(n+1)} - \tilde{\boldsymbol{\phi}}^{(n)}| < \text{min}_i \frac{m_L^i \epsilon_{\boldsymbol{\phi}}}{m_U^i - m_L^i}. \tag{3.40}$$

3.2.7 Objective functions gradient calculation

With the forward model given by Eq. 3.31, the adjoint pressure field, $p^{\dagger s}$ corresponding to the forward field from source point $\mathbf{x}_s$ satisfies

$$\left[\nabla \cdot \left(\frac{1}{\rho}\nabla\right) - \frac{1}{K}\partial_t^2\right] p^{\dagger s} = -\sum_r (p(\mathbf{x},t) - p^*(\mathbf{x},t))\delta(\mathbf{x}-\mathbf{x}_r). \tag{3.41}$$

Comparing model 3.31 with Eq. 3.22, Eq. 3.21 with Eq. 3.32, and Eq. 3.41 with Eq. 3.26, we recognise

$$F(p,m) = \left[\nabla \cdot \left(\frac{1}{\rho(\mathbf{x})}\nabla\right) - \frac{1}{K(\mathbf{x})}\partial_t^2\right] p^{\dagger s}, \quad h(p,m) = \frac{1}{2}\sum_s \sum_r \int_0^T w_{rs}\left[p^{rs}(t;\boldsymbol{\phi}) - p^{*rs}(t)\right]^2 dt.$$

With these choices, we have

$$\frac{\partial F}{\partial K(\mathbf{x})} = \frac{1}{K(\mathbf{x})^2}\partial_t^2 p \qquad \frac{\partial F}{\partial \rho(\mathbf{x})} = -\nabla\left(\frac{1}{\rho(\mathbf{x})^2}\nabla p\right)$$

and with $\boldsymbol{\phi} = (\rho(\mathbf{x}), K(\mathbf{x}))^T$, Eq.3.27 yields, for ρ and K at a given $\mathbf{x}$,

$$\delta\mathcal{E} = -\left\langle p^\dagger, \frac{1}{K^2}\partial_t^2 p\right\rangle_Q \delta K + \left\langle p^\dagger, \nabla\left(\frac{1}{\rho^2}\nabla p\right)\right\rangle_Q \delta\rho$$

If the first bracket in Eq. **??** is integrated by parts once in time, the boundary terms will vanish due the following conditions on p and $p^\dagger$,

$$\begin{aligned}\partial_t p(\mathbf{x},t)_{t=0} &= 0,\\ p^\dagger(\mathbf{x},t)_{t=T} &= 0.\end{aligned} \tag{3.42}$$

Computationally, in order to realise the second condition in Eq. 3.42, $p^\dagger$ is calculated by a numerical solver from a *time reversed* source, with an equivalent *initial* condition imposed, then the resulting field is itself time reversed to yield $p^\dagger$.

Meanwhile, if the second bracket in Eq. **??** is integrated by parts once in space, the boundary term will vanish given the following boundary condition, made explicit in [**?**]

$$\partial_n p(\mathbf{x},t)_{\mathbf{x}\in\delta\Omega} = 0. \tag{3.43}$$

This results in

$$\delta\mathcal{E} = \frac{1}{K^2}\left\langle \partial_t p^\dagger, \partial_t p\right\rangle_Q \delta K - \frac{1}{\rho^2}\left\langle \nabla p^\dagger, \nabla p\right\rangle_Q \delta\rho.$$

Expanding the notation, and defining a *gradient* function for $\mathcal{E}$ as

$$\delta\mathcal{E} = \int\int\int \nabla_m \mathcal{E}(\mathbf{x})\, d^3 r$$

we have, for ρ and K at an explicit location,

$$(\nabla_{\rho(\mathbf{x})}\mathcal{E})(\mathbf{x}) = -\frac{1}{\rho(\mathbf{x})^2}\sum_s \int_0^T \nabla p^s(\mathbf{x},t)\cdot\nabla p^{\dagger s}(\mathbf{x},t)\, dt \tag{3.44}$$

$$(\nabla_{K(\mathbf{x})}\mathcal{E})(\mathbf{x}) = \frac{1}{K(\mathbf{x})^2}\sum_s \int_0^T \partial_t p^s(\mathbf{x},t)\partial_t p^{\dagger s}(\mathbf{x},t)\, dt \tag{3.45}$$

.

Following [131], the gradient with respect to the value of medium parameters in one region of a piecewise homogeneous medium may be obtained by integrating the above expressions over this region.

$$(\nabla_{K_i}\mathcal{E})(\mathbf{x}) = \int_{C_i} (\nabla_{K(\mathbf{x})}\mathcal{E})(\mathbf{x})\, d\mathbf{x} \tag{3.46}$$

.

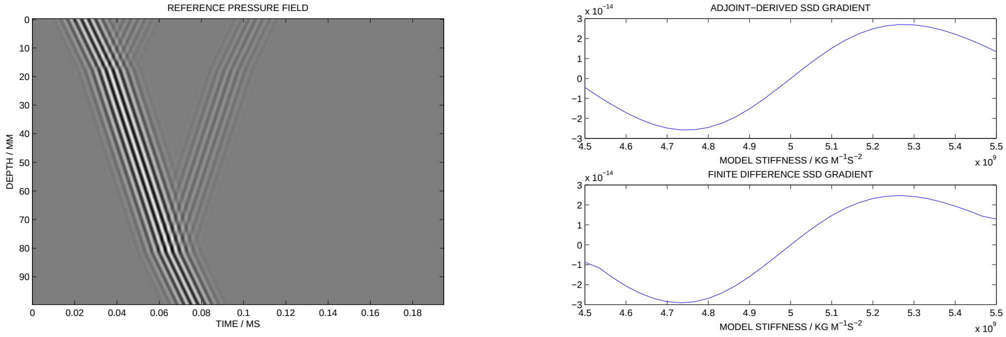

(a) p_{obs} (b) gradient plots

Figure 3.5: Analytical SSD gradient calculation in the 'stripe' phantom using p_{obs} (3.5(a)) compared with a finite difference approximation (3.5(b)). Only first echoes are considered, so that *three* signals are received (at the top and bottom edges) from each input pulse at the top edge.

Figure, 3.5 shows an analytical computation of $\nabla_K \mathcal{E}$ for one compartment of a one-dimensional medium, compared with a finite difference gradient.

In the computation illustrated in Fig. 3.5, the source term playing the role of the right hand side of Eq. 3.26 was

$$\begin{aligned}\tilde{S}_s(z,t) &= \frac{\partial \mathcal{E}}{\partial p^s(z,t)} \\ &= \sum_r \delta(z - z_r)\,(p^{rs}(z,t) - p^{*rs}(z,t))^2.\end{aligned} \tag{3.47}$$

This was converted into a form usable as input to *k-Wave* using d'Alembert's plane-wave solution to Eq. 3.31

$$p^\dagger(z,t) = \frac{\rho_0 c_0}{2} \int_0^t \int_{z-c(t-t')}^{z+c(t-t')} \tilde{S}_s(z',t')\,dz'\,dt' \tag{3.48}$$

See App. B for the general derivation of this solution. Note that, because $p^\dagger$ obeys a *ternminal condition* whereas p obeys an *initial conditio*, the computationally practical way to generate $p^\dagger(\mathbf{x},t)$ is propagate S_s 'backwards' in time, i.e. use the following integral instead of Eq. 3.48

$$p^\dagger(z,t) = \frac{\rho_0 c_0}{2} \int_0^t \int_{z-c(t-t')}^{z+c(t-t')} \tilde{S}_s(z',T-t')\,dz'\,dt'. \tag{3.49}$$

Then, the above expression is propagated by *k-Wave* with initial conditions $p^\dagger(z,0) = \partial_t p^\dagger(z,0) = 0$, and the resulting full field time reversed in time to obtain a $p^\dagger$ obeying the necessary *terminal* conditions.

Since $\tilde{S}$ is supported only at the receiver points, $\mathbf{x}_r$, the double integral is achieved by integrating the second bracket in Eq. 3.47 with respect to time only. In two spatial dimensions, the same reasoning was used, with a double delta function in Eq. 3.47. Then, since the physical source, S is a Gaussian-modulated sinusoidal pulse, and propagation is linear, $\tilde{S}$ will consist of a superposition of such pulses, with the same frequency support as S. The time integral of a Gaussian pulse is approximately another Gaussian pulse, the approximation improving the greater the number of cycles the pulse contains (see App. D),

$$\int e^{-\frac{t^2}{2\sigma^2}}\, e^{i\omega t}\, dt \approx \frac{1}{2} e^{it\omega} \left(-\frac{2i}{\omega} e^{-\frac{t^2}{2\sigma^2}} \right) \tag{3.50}$$

Equation 3.48 then gives, as the adjoint pressure field in the neighbourhood of the “adjoint source” positions, $\mathbf{x}_r$,

$$p^{\dagger}(z,t) \approx -\frac{\rho_0 c_0 i}{2\omega} \tilde{S}_s. \tag{3.51}$$

For the “stripe” phantom medium described in Sec. 3.2.2, this pressure corresponds to the signal assigned to the `source.p` field on running *k-Wave* to calculate the adjoint field.

In the case of the envelope-based cost function, Eq. 3.33, the adjoint source, Eq. 3.47, must be replaced with an alternative, as in [125], [132], [130].

$$\begin{aligned} \tilde{S}_{\mathsf{ENV},s}(z,t) &= \frac{\partial \mathcal{E}_{\mathsf{ENV}}}{\partial p^s(z,t)} \\ &= \sum_r \delta(z - z_r) \int_0^T \frac{\partial E[p^{rs}](\tau;\boldsymbol{\phi}))}{\partial p^{rs}(t;\boldsymbol{\phi})} \Big[E[p^{rs}](\tau;\boldsymbol{\phi}) - E[p^{*rs}](\tau) \Big]\, d\tau. \end{aligned} \tag{3.52}$$

where

$$\frac{\partial E[p](\tau)}{\partial p(t)} = \begin{cases} \frac{H[p](\tau)}{\pi(\tau - t) E[p](\tau)} & \text{if } t \neq \tau; \\ \frac{p(t)}{E[p](t)} & \text{if } t = \tau \end{cases}$$

For the “NIM” cost function, 3.34,

$$\begin{aligned} \tilde{S}_{\mathsf{NIM},s}(z,t) &= \frac{\partial \mathcal{E}_{\mathsf{NIM}}}{\partial p^s(z,t)} \\ &= \sum_r \delta(z - z_r) \int_0^T \frac{\partial \mathcal{E}_{\mathsf{NIM}}[p^{rs}](\tau;\boldsymbol{\phi})}{\partial p^{rs}(t;\boldsymbol{\phi})} \Big[\mathcal{E}_{\mathsf{NIM}}[p^{rs}](\tau;\boldsymbol{\phi}) - \mathcal{E}_{\mathsf{NIM}}[p^{*rs}](\tau) \Big]\, d\tau. \end{aligned} \tag{3.53}$$

where

$$\frac{\partial \mathcal{E}_{\mathsf{NIM}}[p](\tau)}{\partial p(t)} = \frac{\int_0^\tau \frac{\partial E[p](t')}{\partial p(t)}\,dt' - \mathcal{E}_{\mathsf{NIM}}[p](\tau)\int_0^T \frac{\partial E[p](t')}{\partial p(t)}\,dt'}{\int_0^T E[p](t')\,dt'}$$

3.2.8 Velocity model estimation

In the reflection-only case, recovery was expected to be more problematic, due to the relative weakness of information arriving from behind the second layer. Since the arrival times of echoes from *behind* the second compartment depend on sound speed in the first compartment, but not vice-versa, I restricted both reference and model signals to the time interval $[0, t_1]$, where t_1 was chosen to be shortly after the arrival of the *second* echo in the reference signal. The reference signal truncated in this way, $\{p^*(\mathbf{x}_r, t) : t \in [0, t_1]\}$ contains only information about the first compartment, C_1. The speed in C_1, denoted c_1, can be estimated by minimising SSD between the envelopes of $\{p^*(\mathbf{x}_r, t) : t \in [0, t_1]\}$ and $\{p(\mathbf{x}_r, t) : t \in [0, t_1]\}$ with respect to ρ_1, holding K_1 fixed. The resulting $\{\rho_1, K_1\}$ are then held fixed in a similar minimisation to estimate ρ_2, using signals $\{p^*(\mathbf{x}_r, t) : t \in [0, t_2]\}$ and $\{p(\mathbf{x}_r, t) : t \in [0, t_2]\}$. In this bootstrapping way, a velocity model is estimated. It is similar to the “velocity spectrum” technique used in reflection seismology, [133], and only applicable in this form for a layered medium. Optimisation of $\{\rho_i\}$ and $\{K_i\}$ can then be constrained to this model, $\{c_i\}$, reducing the likelihood that a model point become trapped in a local minimum or region of weak variation in a certain direction.

3.2.9 Experiments in 1-D profile phanta

Four-compartment profile media were constructed from combinations of those shown in Fig. 3.1(a) and Fig. 3.1(b) In these media, the compartments are labelled 1,2,3,4 from left to right, and the pressure signals were both transmitted and received from the left-hand end. I performed three parameter recovery experiments as follows.

i. With densities as in Fig. 3.1(a) and speeds homogeneous throughout, recovery of the densities in compartment 2, 3 and 4 was attempted.

ii. With speeds as in Fig. 3.1(b) and densities homogeneous throughout, recovery of speeds in compartment 2, 3 and 4 was attempted.

iii. With densities as in Fig. 3.1(a) and speeds as in Fig. 3.1(b), simultaneous recovery of both in compartments 2, 3 and 4 was attempted.

In all cases, density and speed in compartment 1 was assumed known as a “background” value. The transmitted pressure signal was a pulse of centre frequency 1.0 MHz, temporal envelope width $\sigma = 5.0 \times 10^{-7}$ s, and amplitude 5.0×10^{5} Pa. The medium was 4 cm long with grid spacing $dz = 0.1$ mm. In case i) temporal discretization was $dt = 3 \times 10^{-8}$ s, while in ii) and iii) it was $dt = 6 \times 10^{-8}$ s. Cost function and parameter tolerances were set to zero, so that the estimations terminated on N_{iter}.

Fig.	N_k	envelope	scheme	maxIter	maxLs	$\epsilon_{\mathbf{m}}$	$\epsilon_{\mathcal{E}}$	α_0
3.10(a)	2	no	iii	40	20	0.01	0	1.0×10^3
3.10(b)	2	yes	iii	20	20	0.01	0	1.0×10^5
3.12(a)	1	no	iii	20	20	0.01	0	1.0×10^6
3.12(b)	1	yes	iii	20	20	0.01	0	1.0×10^6

Table 3.3: Optimisation parameters for stripe phantom recovery tests

3.2.10 Experiments in “stripe” phanta

The numerical “stripe” phantom shown in Fig. 3.1(c) was used to develop and test the MATLAB implementation of the adjoint-field cost function gradient. It allows visualisation of propagation in one dimension only (plane waves). This can be done by setting the absorption coefficient in a *perfectly-matched layer* (PML), surrounding the medium, to zero on the left and right hand sides. The *periodic* boundary conditions inherent in *k-Wave* then cause the computed pressure field to “wrap” cylindrically so that the lateral extent of the medium (and the transmitter/sensor array) is essentially infinite. Outside the top and bottom edges, the PML is set to absorb perfectly. I have assumed that this is sufficient to mimic a *radiating* boundary condition, so that the medium is longitudially infinite.

3.2.11 Single-compartment inclusion with transmission data

I used Algorithm 2 under “scheme iii” to attempt simultaneous recovery of density and bulk modulus within the central stripe compartment, using two- and one-element “lines” arrays. The two-element version is shown in Fig. 3.2(a). Reference values for the compartment were set to ρ^* = 900 kg m^{-3} and K^* = 2.0000×10^9 kg m^{-1}s^{-2}. The background values were 1000 kg m^{-1}s^{-2} and 2.3716×10^9 kg m^{-1}s^{-2}. In minimising $\mathcal{E}$, and $\mathcal{E}_{\text{ENV}}$, twenty initial points $\boldsymbol{\phi}_{\text{init}} = (\rho_{\text{init}}, K_{\text{init}})^T$ were selected from a uniform random distribution within $(\rho^* \pm 20\%, K^* \pm 15\%)^T$. Optimisation parameters for the four cases are tabulated in Tab. 3.3.

To illustrate the benefit of the full NIM method over the “envelope-only” variant, I performed optimisations for each, initialised within $(\rho^* \pm 50\%, K^* \pm 50\%)^T$, where ρ^* = 1100 kg m^{-3} and K^* = 2.0000×10^9 kg m^{-1}s^{-2}.

3.2.12 Single-compartment inclusion with reflection data only

The one-element version of the “lines” array retains only the upper of the two elements (shown in Fig. 3.2(a)), so that only *reflection* data contribute to the cost function. In this case, the relationship between physical parameters in the *reference compartment* and in the *background* have a strong effect on the appearance of the cost function. Density, impedance, bulk modulus and small-signal sound speed are related by the equations

$$K = \rho c^2, \quad Z = \rho c, \tag{3.54}$$

so that

$$\rho K = Z^2 \tag{3.55}$$

Hence, the iso-speed curves on a $\rho - K$ plot, for a given compartment, are straight lines through the origin, whereas iso-impedance curves are rectangular hyperbolae. When echoes are small in the *reference* data, the arrival time of model echoes has little influence on the cost function, so that the effect of impedance change dominates that of speed change, leading to a hyperbolic valley, as illustrated by Fig. 3.6.

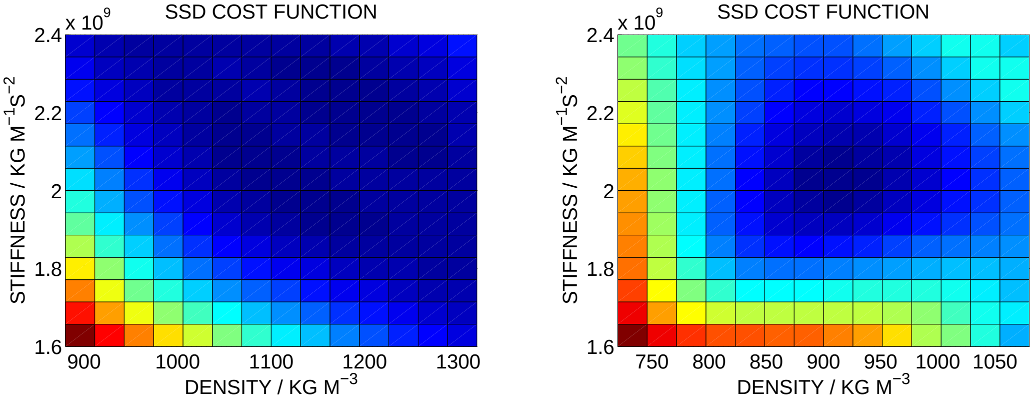

(a) $\mathcal{E}_{\text{ENV}}$ for $Z^* \approx Z_{\text{bkgd}}$

(b) $\mathcal{E}_{\text{ENV}}$ for Z^* far from Z_{bkgd}

Figure 3.6: The effect of impedance change in front of a compartment of interest upon $\mathcal{E}_{\text{ENV}}$. The influence of c_{model} is weaker when the impedance change in the reference medium is small.

Some optimisation results are presented for a case where $Z^* \ll Z_{\text{bkgd}}$, using the medium parameters given in the first experiment of Sec. 3.2.11, but concentrate on the more problematic case where $Z^* \approx Z_{\text{bkgd}}$.

Early results obtained using “NIM”, “envelope” and classic versions of the adjoint state method suggested a three-step approach exploiting the characteristics of each, to overcome the difficulty of using *reflection data* only, with no signals received after transmission *through* the medium. I attempted ten optimisations initialised within $(\rho^* \pm 50\%, K^* \pm 50\%)^T$ with ρ^* = 1100 kg m^{-3} and K^* = 2.0000$\times$10^9 kg m^{-1}s^{-2}. In the first stage, $\mathcal{E}_{\text{NIM}}$ is minimised, the a second optimisation is initialised from the model points estimated from the first, to minimise $\mathcal{E}_{\text{ENV}}$. Finally, a third optimisation is initialised from the end points of the second, to minimise $\mathcal{E}$.

The poor results of this experiment suggested that, when $Z^* \approx Z_{\text{bkgd}}$, $\mathcal{E}_{\text{ENV}}$ is unable to determine sound speed accurately, so that more of the available information should be exploited. This was done by first obtaining estimates $\{c_i^*\}$ of the sound speeds as described in Sec. 3.2.14, then performing the

Fig.	N_k	envelope	scheme	maxIter	maxLs	$\epsilon_{\mathbf{m}}$	$\epsilon_{\mathcal{E}}$	α_0
3.15	2	yes	iii	20	20	0.001	0	1.0×10^6

Table 3.4: Optimisation parameters for double stripe phantom recovery

layer	ρ / kg m^{-3}	K / kg m^{-1}s^{-2}
1	900	2.0×10^9
2	1100	2.5×10^9

Table 3.5: Medium parameters for two-compartment reflection-based recovery

optimisation of $\{\rho_i, K_i\}$ subjuect to the constraints $K_i = \rho_i c_i^{*2}$. Some results of applying this approach are presented in Sec's. 3.3.4 and 3.3.6.

3.2.13 Two-compartment inclusion with transmission data

Twenty density and bulk modulus recoveries were attempted in a two-stripe medium with reference values ρ^{*1} = 900 kg m^{-3}, ρ^{*2} = 1100 kg m^{-3}, K^{*1} = 2.0×10^9 kg m^{-1}s^{-2}, K^{*2} = 2.5×10^9 kg m^{-1}s^{-2}, with background values as in the one-stripe medium. The trials were initialised within 5% of reference values and optimised using $\mathcal{E}_{\text{ENV}}$ with the parameters given in Tab. 3.4.

3.2.14 Two-compartment inclusion with reflection data only

The restriction to reflection data can quickly lead to ill-posedness even in simple cases. In order to improve reduce the likelihood of optimisation trials leading to local minima of the objective function, I adopted an approach where sound-speeds were initially estimated independently, then density and bulk modulus were estimated while constraining to the speeds obtained in the first step. This method exploited the arrival times of the received signals to estimate compartment speeds *one at a time*, as explained in Sec. 3.2.8.

Forty optimisations were run on a two-compartment medium with a single transmitter/receiver. Reference values for the medium parameters were as given in Tab. 3.5. Twenty were constrained to a velocity model obtained as above, and twenty were constrained to the reference (true) velocity values. The optimiser for the constrained step was MATLAB's `fmincon`, executing a Sequential Quadratic Programming implementation. Termination tolerances were set to zero.

3.2.15 Experiments in circle phanta

The circular region in the medium shown in Fig. 3.1(e) was assigned properties of ρ^* = 900 kg m^{-3} and K^* = 2.0×10^9 kg m^{-1}s^{-2}, Recovery from ten random initialisations within 10% of these values was attempted, using a four-stage approach. After estimating speed in the circle as in 3.2.8. Termination tolerances were set to zero.

region	ρ_0 / kgm^{-3}	K_0 / kgm^{-1}s^{-2}
1	900	2.0×10^9
2	1100	2.5×10^9
0	1000	2.3716×10^9

Table 3.6: Medium parameters for the split circle

compartment	2	3	4
true ρ / kgm^{-3}	900	1100	940
initialised ρ / kgm^{-3}	850	1200	900
recovered ρ / kgm^{-3}	887.9	1115.8	945.3

Table 3.7: Estimating ρ_2, ρ_3, ρ_4 of $\rho_1, \rho_2, \rho_3, \rho_4$ in a 1D profile.

The same procedure was attempted for the "split circle" shown in Fig. 3.1(f), where reference acoustic properties were as in Tab. 3.6. A source/receiver array of five elements was placed in the "twelve o'clock" position of the eight positions shown in Fig. 3.2(c), so that $N_k = 5$ and $N_j = 1$. For phases 2 and 3, 0.002 and 0.01, respectively, were used for $\epsilon_{\tilde{\mathbf{m}}}$, with $\epsilon_{\mathcal{E}}$=0.

3.3 Results

3.3.1 Results in 1D profile phanta

Density recovery results, i.e. experiment i in Sec. 3.2.9 are summarized in Tab. 3.7 and Fig. 3.7. Speed recovery results from experiment ii are summarized in Tab. 3.8 and Fig. 3.7. Simultaneous recovery results from experiment iii are summarized in Tab. 3.9 and Fig. 3.9.

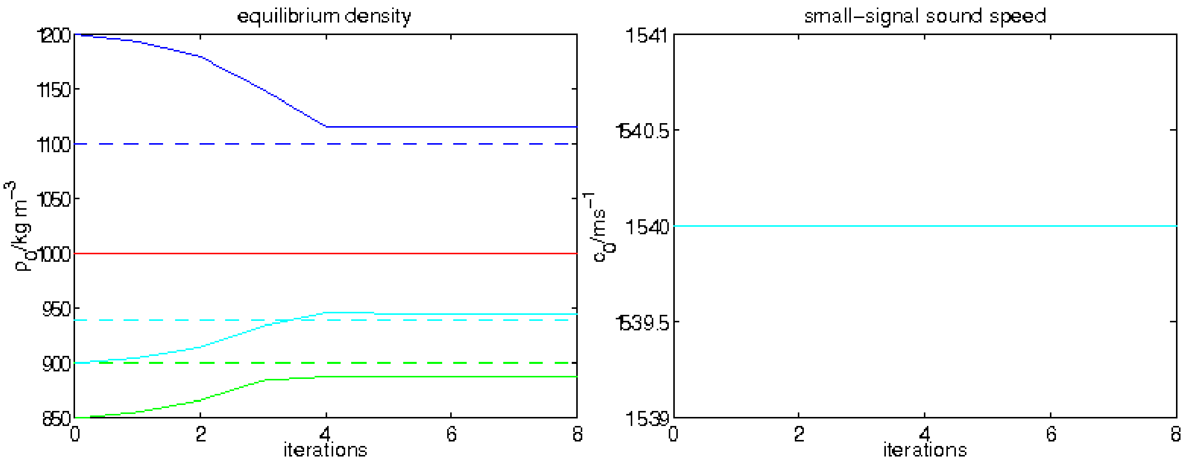

Figure 3.7: Estimating ρ_2, ρ_3, ρ_4 of $\rho_1, \rho_2, \rho_3, \rho_4$ in a 1D profile.

compartment	2	3	4
true c / ms^{-1}	1540.0	1538.0	1541.0
initialised c / ms^{-1}	1539.0	1539.0	1539.0
recovered c / ms^{-1}	1540.0	1538.0	1540.9

Table 3.8: Estimating c_2, c_3, c_4 of c_1, c_2, c_3, c_4 in a 1D profile.

	Initialisation 1			Initialisation 2		
Compartment	1	2	3	1	2	3
c_0 / ms^{-1}						
true	1539	1540	1538	1539	1540	1538
initialised	1537	1525	1540	1541	1538	1540
recovered	1554.1	1539.2	1538.9	1554.8	1538.6	1539.2
ρ_0 / kg m^{-3}						
true	1000	995	1010	1000	995	1010
initialised	1020	991	1012	998	999	1008
recovered	999.5	998.2	1012.7	995.9	995.6	1010.6
Z / kg m^{-2} s^{-1}						
true	1539000	1532300	1553380	1539000	1532300	1553380
initialised	1567740	1511275	1558480	1537918	1536462	1552320
recovered	1553300	1536400	1558400	1548400	1531800	1555500

Table 3.9: Results for simultaneous density/speed recovery

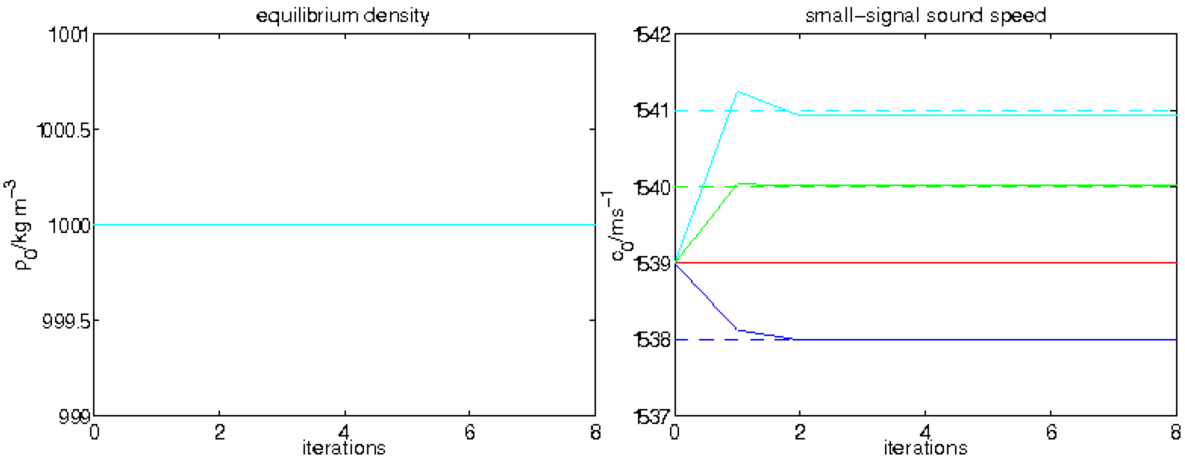

Figure 3.8: Estimating c_2, c_3, c_4 of c_1, c_2, c_3, c_4 in a 1D profile.

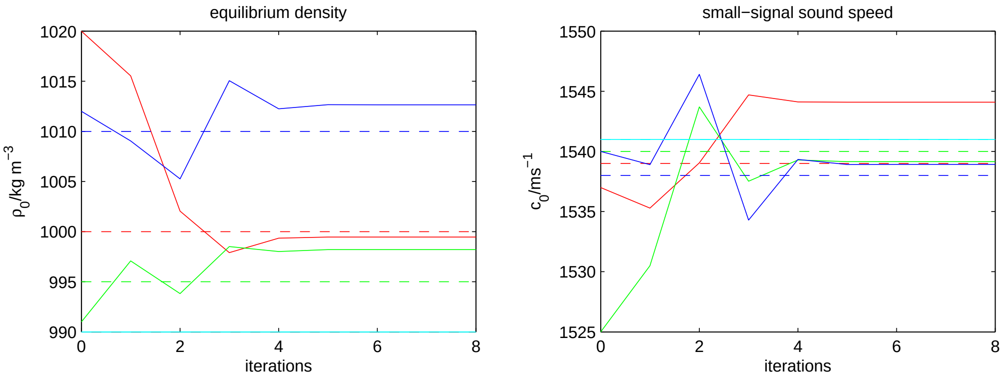

Figure 3.9: simultaneous optimisation in compartments 2,3,4 of 1D profile. Initialisation 1

3.3.2 Results in stripe phanta

3.3.3 Single-compartment medium with transmission data

Figures 3.10 and 3.12 show the progress of the optimisations described in Sec. 3.2.11. Black circles represent initial points and green circles final points. The points are superimposed on a two-dimensional cost function plot over model density and bulk modulus in the stripe compartment. The reference (target) position is in the centre.

The results are summarised in Tabs. 3.10-3.11.

	init. error / %	fin. error / %	≤1%
ρ	(6.43±5.19)	(10.35±11.22)	3/20
K	(7.81±4.57)	(10.29±10.50)	3/20

Table 3.10: mimimising $\mathcal{E}_{\text{SSD}}$ with $N_k = 2$, (3.12±3.40) mins

	init. error / %	fin. error / %	≤1%
ρ	(7.32±4.35)	(0.00±0.00)	20/20
K	(7.94±3.48)	(0.00±0.00)	20/20

Table 3.11: mimimising $\mathcal{E}_{\text{ENV}}$ with $N_k = 2$, (15.39±3.75) mins

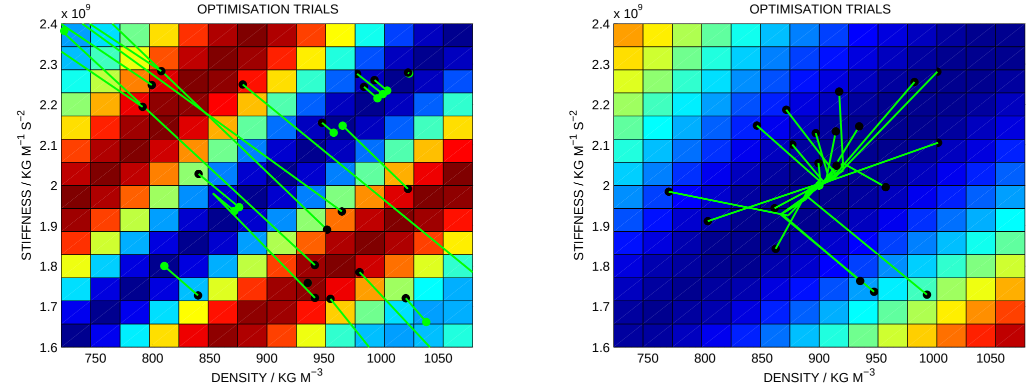

(a) minimising $\mathcal{E}_{\text{SSD}}$ (b) minimising $\mathcal{E}_{\text{ENV}}$

Figure 3.10: Simultaneous density, bulk modulus recovery for stripe phantom with “line” array and transmission data available ($N_k = 2$).

Figure 3.11 illustrates the benefit of using normalised integrated signals in the cost function (in $\mathcal{E}_{\text{NIM}}$), over using signal envelopes (in $\mathcal{E}_{\text{ENV}}$). The integral of the modelled signal will always overlap with some contribution to the integral of the reference signal, so that information about the arrival time of the second echo, which informs us about the speed in the compartment, can be obtained even when the modelled and reference second echoes do not overlap temporally. This eliminates the plateaux regions seen in Fig. 3.11(a). The magenta-coloured point in Fig. 3.11(a) is the initial point for a trial that went out of an acceptable (physical) range.

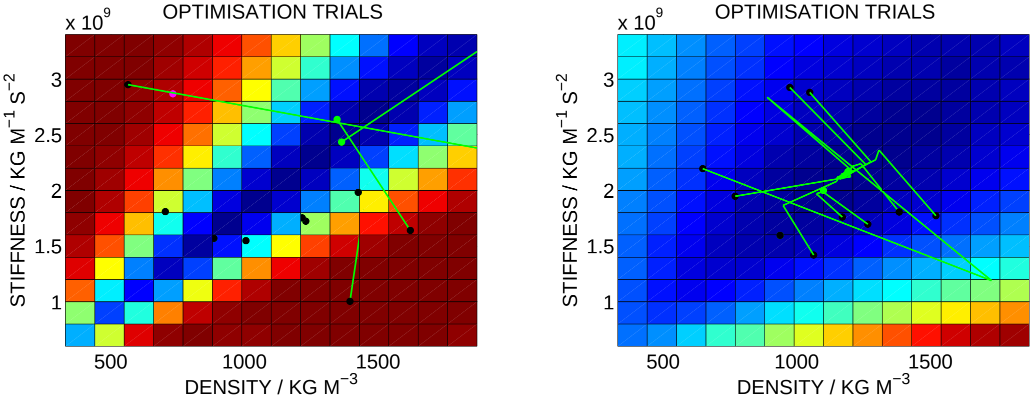

(a) minimising $\mathcal{E}_{\text{ENV}}$ (b) minimising $\mathcal{E}_{\text{NIM}}$

Figure 3.11: Simultaneous density, bulk modulus recovery for stripe phantom with “line” array ($N_k = 2$).

3.3.4 Single-stripe medium with reflection data only

Optimisation results are shown in Fig. 3.12, Tab. 3.12 and Tab. 3.13 for a case where $Z^* \ll Z^0$.

Results of three-step unconstrained optimisation for reflection-only data are illustrated in Fig. 3.13,

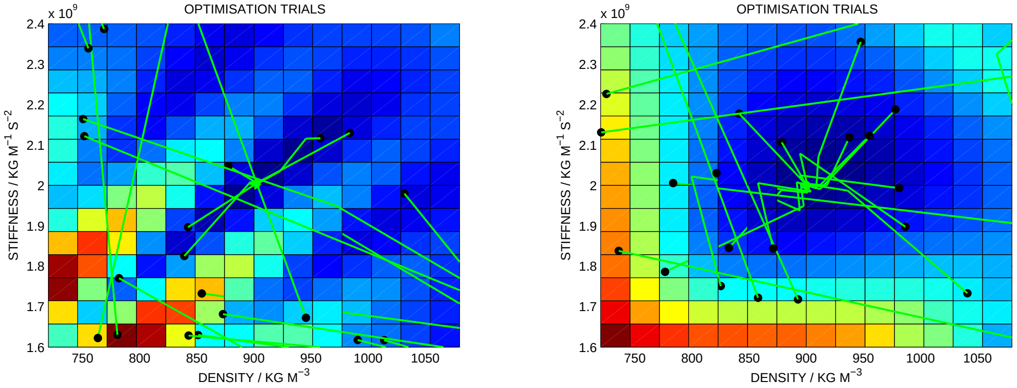

(a) minimising $\mathcal{E}_{\text{SSD}}$

(b) minimising $\mathcal{E}_{\text{ENV}}$

Figure 3.12: Simultaneous density, bulk modulus recovery for stripe phantom with “line” array with reflection data only ($N_k = 1$).

	init. error / %	fin. error / %	≤1%
ρ	(10.35±6.19)	(30.77±25.77)	5/20
K	(8.12±4.95)	(33.73±25.77)	5/20

Table 3.12: mimimising $\mathcal{E}_{\text{SSD}}$ with $N_k = 1$, running time = (10.74±4.48) mins

and Tab. 3.14 for a case where $Z^* \approx Z_0$.

Parameters for the same medium were recovered much more successfully by a constrained minimisation of $\mathcal{E}_{\text{ENV}}$, using a pre-estimated velocity model, followed by unconstrained minimisation of $\mathcal{E}$. The final stage of this is shown in Fig. 3.14, and summarised in Tab. 3.15

3.3.5 Two-stripe medium with transmission data

Figures 3.15 shows the progress of the optimisations described in Sec. 3.2.13, with results summarised in Tab. 3.15(c) and Fig. 3.15(d).

3.3.6 Two-stripe medium with reflection data only

Figure 3.16 shows the progress of the recoveries described in Sec. 3.2.14. The speed-constrained minimisation of $\mathcal{E}_{\text{ENV}}$ recovered all four parameters accurately within a few iterations in all but one case. The subsequent, unconstrained minimisation of $\mathcal{E}_{textsfSSD}$, shown to the right of the red line,

	init. error / %	fin. error / %	≤1%
ρ	(9.49±5.92)	(16.57±23.93)	12/20
K	(11.26±5.59)	(25.73±39.12)	12/20

Table 3.13: mimimising $\mathcal{E}_{\text{ENV}}$ with $N_k = 1$, running time = (7.45±1.73) mins

	init. error / %	fin. error / %	≤1 %	fin. error / %	≤1%	fin. error / %	≤1%
ρ	(23.46±16.02)	(26.88±24.86)	3/20	(25.70±24.67)	5/20	(23.49±24.03)	6/20
K	(22.31±14.56)	(19.12±29.41)	2/20	(19.23±29.90)	5/20	(22.10±30.39)	7/20

Table 3.14: Simultaneous density and bulk modulus recovery in a single-stripe phantom with reflection data only. Between columns 2 and 3, $\mathcal{E}_{\text{NIM}}$ was minimised without constraint (14.1±5.6)mins, column 4 shows the result of minimising $\mathcal{E}_{\text{ENV}}$ without constraint (14.10±6.49)mins, and column 5 the result of minimising $\mathcal{E}_{\text{SSD}}$ without constraint (13.8±7.7)mins

	init. error / %	fin. error / %	≤1%	init. error / %	fin. error / %	≤1%
ρ^1	(23.62±11.38)	(3.69±4.04)	10/19	(3.69±4.04)	(0.00±0.00)	18/19
K^1	(23.55±11.34)	(3.62±3.96)	10/19	(3.62±3.96)	(0.00±0.00)	18/19

Table 3.15: Columns 2 and 3 show the speed-constrained minimisation of $\mathcal{E}_{\text{ENV}}$ with $N_k = 1$, running time = (11.68±0.43) mins. Columns 4 and 5 show unconstrained minimisation of $\mathcal{E}$, running time = (4.67±0.01) mins.

	init. error / %	fin. error / %	≤1%
ρ	(3.73±4.04)	(0.08±0.00)	20/20
K	(3.66±3.96)	(0.06±0.02)	20/20

Table 3.16: mimimising $\mathcal{E}$ with $N_k = 2$, running time = (6.17±2.77) mins

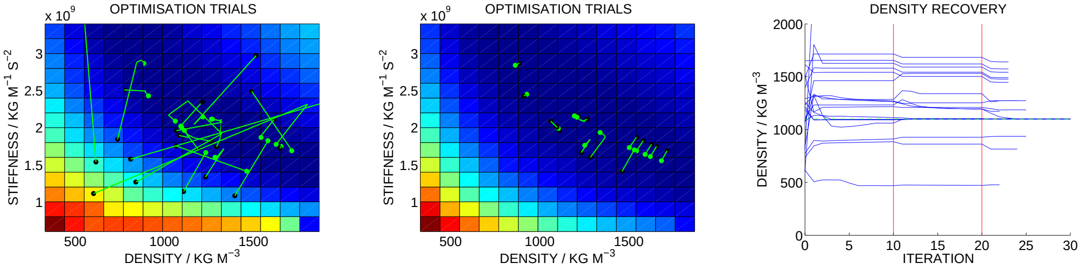

(a) minimising $\mathcal{E}_{\text{NIM}}$ (b) minimising $\mathcal{E}_{\text{env}}$ (c) overall ρ recovery

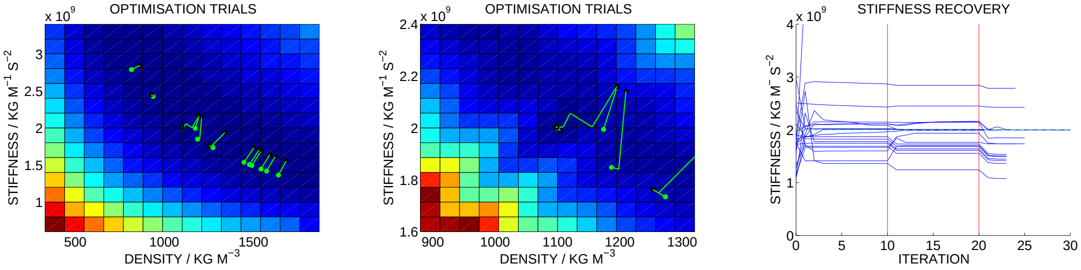

(d) minimising $\mathcal{E}$ (e) minimising $\mathcal{E}$, detail (f) overall K recovery

Figure 3.13: Attempted three-stage simultaneous recovery of density and bulk modulus for stripe phantom with “line” array ($N_k = 1$). In the first phase (between vertical axis and left-hand red line) $\mathcal{E}_{NIM}$ was minimised; in the second phase (between red lines) $\mathcal{E}_{\text{ENV}}$ was minimised; in the third phase (right of right-hand red line) $\mathcal{E}$ was minimised. The green dotted lines indicate the reference (true) parameter values.

made little further progress, terminating with an unfinished line search after the first iteration.

Table 3.17 summarises the optimisations illustrated in Fig. 3.16.

3.3.7 Results in circle phanta

Table 3.18 and Fig. 3.17 summarize the results from four-stage recovery with the circle phantom with $N_k = 5$ and $N_j = 1$.

Table 3.19 and Fig. 3.18 summarize recoveries on the split circle phantom where the last two stages have been terminated on exceeding tolerances in parameter vector norm change and in cost function change.

3.4 Discussion

The INCS method is applicable, in principle, to a possible extension of this work to acoustic parameter estimation under nonlinear propagation. However, although some of the long computation times it suffers from may be due to implementation, they are also due to the need to store and manipulate large arrays holding the pressure field at every time point, since most of the running time was spent performing convolution integrals, albeit using the Fast Fourier Transform. The relatively poor results

	init. error / %	fin. error / %	$\leq$1%	init. error / %	fin. error / %	$\leq$1%
ρ^1	(4.42±2.56)	(0.33±1.01)	19/20	(0.33±1.01)	(0.24±1.03)	19/20
ρ^2	(5.31±3.15)	(0.55±1.93)	19/20	(0.55±1.93)	(0.45±1.95)	19/20
K^1	(4.53±2.62)	(0.32±0.97)	19/20	(0.32±0.97)	(0.23±0.99)	19/20
K^2	(5.36±3.11)	(0.54±1.97)	19/20	(0.54±1.97)	(0.46±1.99)	19/20

Table 3.17: Columns 2 and 3 show the speed-constrained minimisation of $\mathcal{E}_{\text{ENV}}$ with $N_k = 2$, running time = (41.6±0.5) mins. Columns 4 and 5 show unconstrained minimisation of $\mathcal{E}_{\text{SSD}}$, running time = (13.4 ±0.7) mins.

	init. error / %	fin. error / %	$\leq$1 %	fin. error / %	$\leq$1%	fin. error / %	$\leq$1%
ρ	(4.26±2.61)	(1.01±0.00)	0/10	(0.09±0.00)	10/10	(0.00±0.00)	10/10
K	(4.32±2.95)	(0.33±0.00)	10/10	(0.02±0.00)	10/10	(0.00±0.00)	10/10

Table 3.18: Simultaneous density and bulk modulus recovery in a circle phantom with a “curvilinear” array ($N_k = 5$). Between columns 2 and 3, $\mathcal{E}_{\text{NIM}}$ was minimised with a constraint to a pre-estimated velocity model (175±8)mins, column 4 shows the result of minimising $\mathcal{E}_{\text{NIM}}$ without constraint (105.34±0.16)mins, and column 5 the result of minimising $\mathcal{E}$ without constraint (102.73±1.41)mins

	init. error / %	fin. error / %	$\leq$1 %	fin. error / %	$\leq$1%	fin. error / %	$\leq$1%
ρ^1	(5.07±2.79)	(6.63±0.00)	0/10	(0.55±0.23)	10/10	(0.26±0.21)	10/10
ρ^2	(6.58±2.80)	(5.19±2.12)	1/10	(0.87±0.51)	6/10	(0.21±0.14)	10/10
K^1	(13.83±4.64)	(9.80±0.00)	0/10	(0.36±0.31)	10/10	(0.22±0.15)	10/10
K^2	(6.57±3.00)	(5.15±2.12)	0/10	(0.31±0.23)	10/10	(0.22±0.16)	10/10

Table 3.19: Simultaneous density and bulk modulus recovery in the “split circle” phantom with a “curvilinear” array ($N_k = 5$). Termination tolerances were used to reduce computation time. Between columns 2 and 3, $\mathcal{E}_{\text{NIM}}$ was minimised with a constraint to a pre-estimated velocity model (284.4±0.8)mins, column 4 shows the result of minimising $\mathcal{E}_{\text{NIM}}$ without constraint (66.2±1.4)mins, and column 5 the result of minimising $\mathcal{E}$ without constraint (35.6±1.12mins

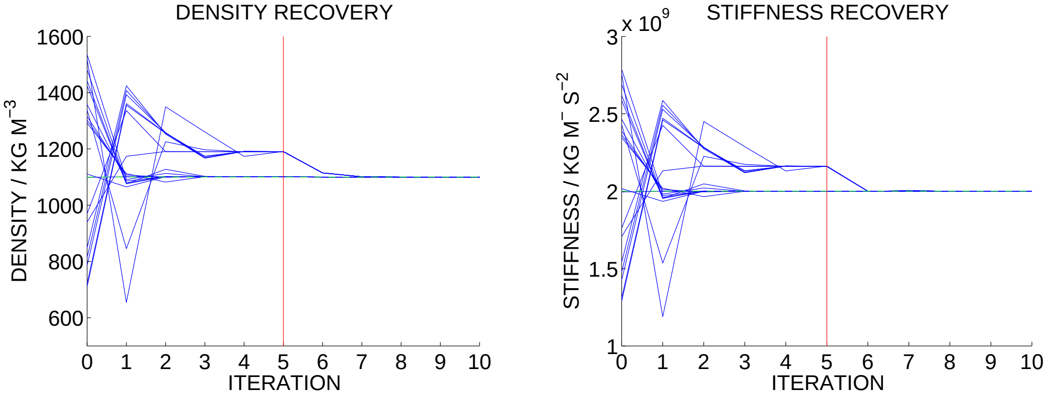

(a) estimating ρ

(b) estimating K

Figure 3.14: Simultaneous density and bulk modulus recovery for stripe phantom with “line” array ($N_k = 1$). Using $\mathcal{E}_{\text{env}}$ with velocity model constraint (left of red line), and using $\mathcal{E}$ unconstrained (right of red line).

produced using this method for simultaneous estimation of ρ and K, shown in Tab. 3.9 and Fig. 3.9, was probably due to the same ill-posedness that affected the k-Wave recovery similarly in Fig. 3.13, even when $\mathcal{E}_{NIM}$ and $\mathcal{E}_{\text{ENV}}$ had been previously used. The improvement shown when the first (ρ, K) estimate is constrained to a pre-estimated speed is apparent between Tables 3.14 and 3.15. In both of these experiments the reference values were the same: ρ^* = 1100 kg m^{-3} and K^* = 2.0000$\times$10^{9} kg m^{-1}s^{-2}, i.e. Z^* bore the same relationship to Z_0 in both cases. The improvement is slightly surprising, since both the speed-constraint and the NIM cost function are designed to ensure that measured and modelled signals overlap in time. The improvement due to a hard *constraint* is immediate, however, so perhaps has a stronger effect. In two spatial dimensions, with more sensors, more ray paths are available, so that the data contain signals with a wider spread of arrival times. This too has the effect of widening the cost function global minimum, resulting in the successful recoveries in Tables 3.15(c) and 3.17.

3.5 Conclusions

The results indicate that denstiy and bulk modulus estimation using *reflection data alone* is feasible, in principle, when combined with a novel technique from the seismology literature to regularise the estimation by defining the cost function in terms of normalised, integrated signal envelopes. Of great interest is the question of whether this remains possible in ill-posed cases made using compartment models *misaligned* with reference media. That is, whether intra-organ mean tissue parameter values can be successfully recovered using an organ-wise homogeneous model mis-aligned to an extent comparable to target registration errors (TRE’s) produced by current multi-modal registration algorithms. A possible computational speed-up when a Newton-type optimisation algorithm is used together with a Hessian derived from the adjoint operator formulation as in [134] might also be inves-

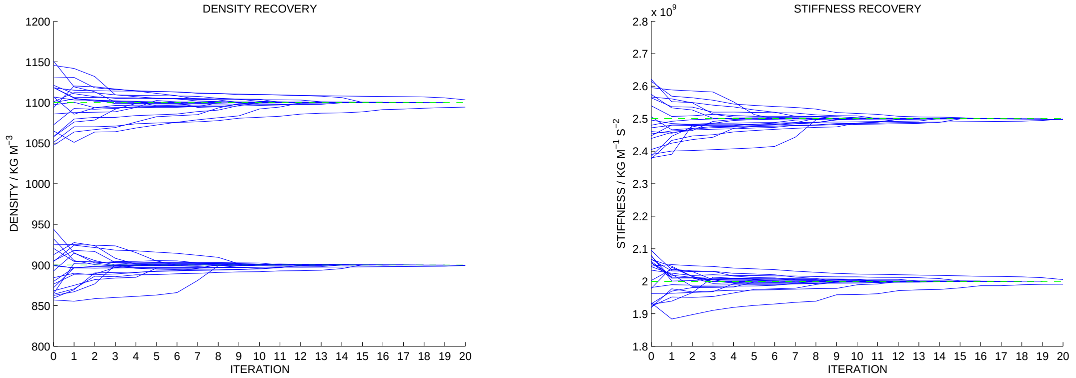

(a) density

(b) bulk modulus

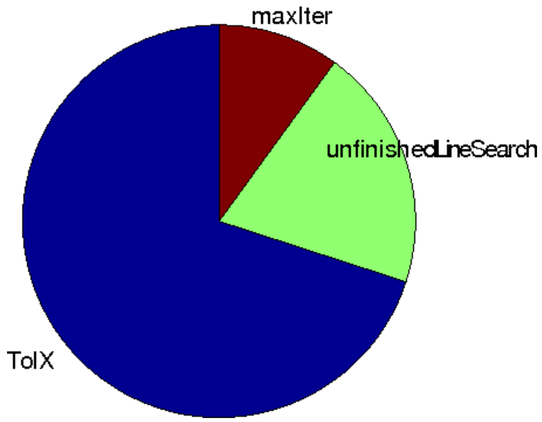

(d) stopping cond'ns

	init. error / %	fin. error / %	≤1%
ρ^1	(2.58±1.57)	(0.01±0.02)	20/20
ρ^2	(2.22±1.59)	(0.05±0.13)	20/20
K^1	(2.84±1.16)	(0.05±0.11)	20/20
K^2	(2.80±1.56)	(0.01±0.02)	20/20

(c) summary statistics

Figure 3.15: Simultaneous estimation of density and bulk modulus in the two-stripe medium with transmission data included: estimation progress, (a), (b); summary statistics, (c); stopping conditions, (d)

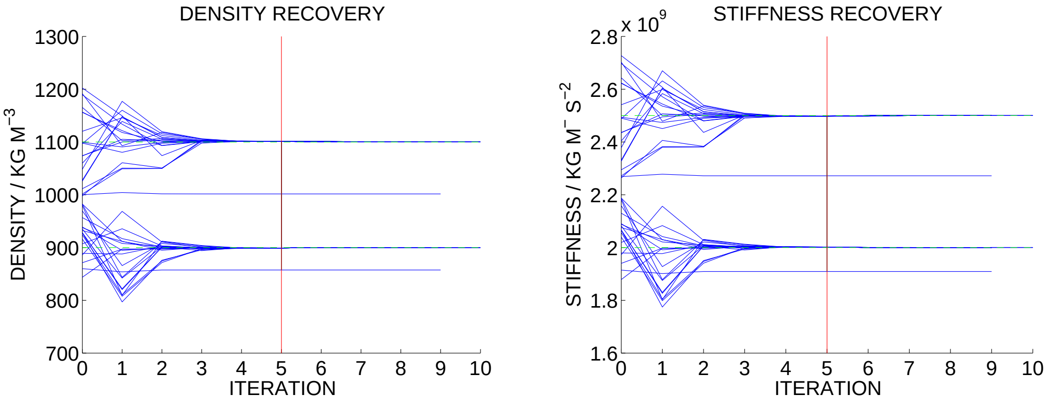

(a) recovering ρ_1, ρ_2

(b) recovering K_1, K_2

Figure 3.16: Density and bulk modulus recovery for two-stripe phantom with “line” array ($N_k = 1$). Using $\mathcal{E}_{\text{ENV}}$ with velocity model constraint (left of red line), and using $\mathcal{E}_{\text{ENV}}$ unconstrained (right of red line).

tigated.

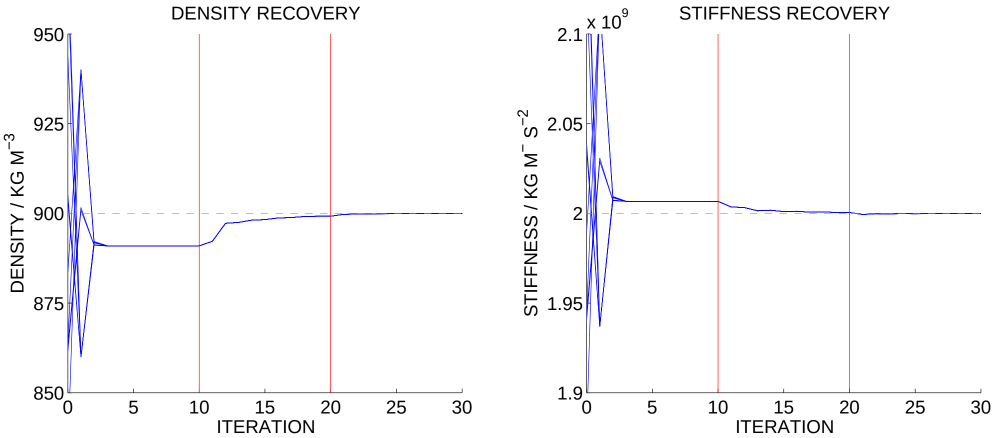

Figure 3.17: Simultaneous density and bulk modulus recovery in a circle phantom with a “curvilinear” array ($N_k = 5$). Iterations 1-10 minimise $\mathcal{E}_{\text{NIM}}$ constrained to a pre-estimated velocity model (175±8)mins, 11-20 minimise $\mathcal{E}_{\text{NIM}}$ without constraint (105.34±0.16)mins, and 21-30 minimise $\mathcal{E}$ without constraint (102.73±1.41)mins

.

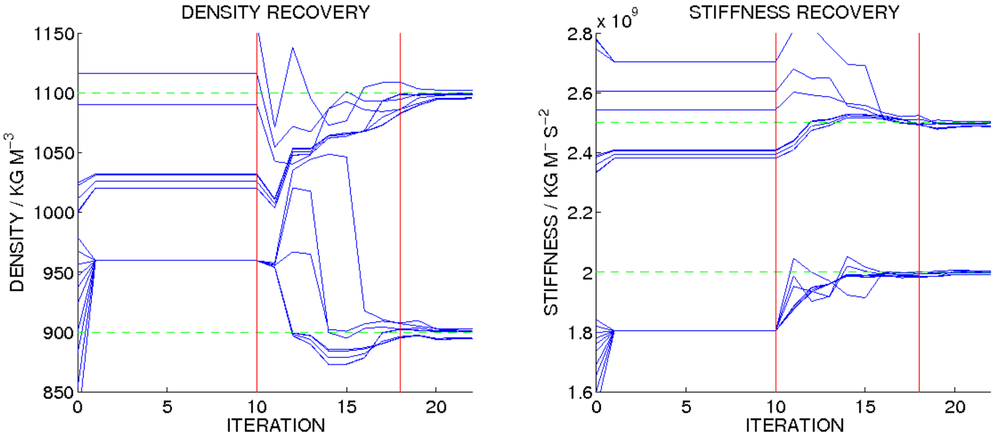

Figure 3.18: Simultaneous density and bulk modulus recovery in the split circle phantom with a “curvilinear” array ($N_k = 5$). Termination tolerances were used to reduce computation time

Chapter 4

A signal dissimilarity criterion resistant to coincident reflection arrivals

4.1 Introduction

4.1.1 Overview

Section 4.1 explains the motivation for this piece of work in terms of the main problem of the thesis, and summarises other work in the literature that I have drawn on. On tackling the “main problem” in a manner which is suited to its constraints of signal data, time and computing resources, and to the availability of prior information, one may enounter a specific subproblem, which is explained in detail in Section 4.2.1. The method developed for solving this subproblem, and experiments performed to demonstrate it, are described in Sec’s 4.2.2 and 4.2.4. Results of these are presented and discussed in Sec’s 4.3 and 4.4, concluding with Sec. 4.5.

4.1.2 Purpose

The problem of estimating acoustic properties of abdominal tissues *in vivo*, including speed-of-sound and density, necessitates the interrogation of the anatomy with ultrasound waves without the ability to isolate samples of single tissues of known size and position with respect to the transducer. A great many geometric and acoustic properties of the medium combine to influence acquired ultrasound signals, so that some kind of comparison to signals containing responses to a *model* medium becomes necessary. The property estimation goal is then converted to the surrogate goal of finding property values that minimise some *dissimilarity* criterion between measured and modelled signals. Many choices for such a criterion are generally possible. A criterion whose global minimum occurs very close to the true property values may, on the other hand, have local minima elsewhere, in which an optimisation algorithm could become trapped. The computation of model signals to evaluate a signal dissimilarity criterion is generally a time-consuming process, so that it is preferable to evaluate it as few times as possible. This means that gradient-based optimisation algorithms are preferred where possible, but these are the kind most likely to become trapped in local minima. A local minimum will always be accompanied by the presence of a local *maximum* between it and the global minimum, and the cause of such a maximum is commonly both specific and comprehensible. A criterion which is a convex function on the parameter space is guaranteed to be free of local maxima. Convexity means that, between any two points in parameter space, the criterion has a value at most equal to the value linearly interpolated from those at the two points, i.e. $\mathcal{E}$ is convex on a parameter space, Ω if, for any two points (parameter vectors), $\boldsymbol{\phi}_a, \boldsymbol{\phi}_b \in \Omega$,

$$\forall t \in [0,1]: \quad \mathcal{E}\left((1-t)\boldsymbol{\phi}_a + t\boldsymbol{\phi}_b\right) \leq (1-t)\mathcal{E}(\boldsymbol{\phi}_a) + t\mathcal{E}(\boldsymbol{\phi}_b).$$

An ultrasound signal dissimilarity criterion with this property — for as many parameters as would be practically considered for inclusion in the vector $\boldsymbol{\phi}$ — is therefore desirable. Its use in optimisation may be either as the sole criterion during minimisation, or in an early stage of an optimistion process, in order to be confident of having moved to the “right side” of any local maxima of some faster-to-compute and more accurate alternative. The purpose, and contribution, of this work in this chapter was to develop a signal dissimilarity criterion *which is convex both with respect to acoustic properties and to parameters describing position and orientation of the medium with respect to an ultrasound transducer array, where a prior model of medium geometry is available, but the only reflected signal data (not transmitted ones) are available*.

4.1.3 Related work

The dissimilarity criterion of the *Normalised Integration Method* was presented by Liu and Chauris et al. for potential use in seismological surveys in which *transmitted* signals were available ([125]). The potential applicability of the *NIM* to *reflected* signals was mentioned in [125], though I am not aware of any subsequent publications in which this is done. However, With medium compartments largely pre-determinable in medical applications, e.g. from MR or CT images — a crucial advantage in medical ultrasound not so readily available in seismology — the dimensionality of the parameter space can be reduced drastically, so that such usage becomes feasible, as was demonstrated in Chapter 3. The method developed in this chapter, called the *Echo-wise Normalised Integration Method*, or *ENIM*, goes further than *NIM* to meet the aim above. It does this by incorporating a sequence of additional pre-processing steps, as described in Section .

One of these steps involves the detection of the arrival times of individual wave packets or “echoes” in reference and modeled signals. This problem has been addressed for other ultrasound applications in, e.g. medical imaging, non-destructive testing and underwater exploration e.g. [135], [136], [137]. Methods for doing this include

- locating the first peak in the signal using a threshold,
- locating the onset of support in, or maxima in the signal envelope,

- locating maxima in the correlation of the signal with a reference waveform,
- locating maxima in the L_1 or L_2 norms of the signal with a shifted reference waveform,
- locating maxima in an “energy” function defined as the sum of the squared magnitude of the cross-correlation of the signal with an ’expected signal’ reference waveform, and the squared magnitude of the cross-correlation of the signal with the Hilbert transform of that reference waveform.

Another step involves the simultaneous fitting of multiple surfaces to a set of points in a 3-D space, without prior knowledge of which points should be fitted to each surface, and with omitted or erroneous points. For this I have used a combination of the well-known *RANdom SAmple Consensus* (*RANSAC*) algorithm, [138], and an adaptation of the *Simultaneous Robust Multiple Fitting* (*SRMF* or ”*SMRF*”) algorithm [139]. The latter was developed for the problem of automatically detecting road markings for the steering of driverless cars, by fitting *curves* to segmentations of the road markings from video images. Adaptating this method to the fitting of surfaces is computationally fairly straightforward.

4.2 Methods

From now on I set $N_j = 1$ and let $N_r = N_k$. Also, the transceiver array is a horizontal, linear array of N_r receivers, $N_{\tilde{s}}$ of which act as sources. The $N_{\tilde{s}}$ sources are regularly spaced along the array with $\tilde{s} = 1, \ldots, N_{\tilde{s}}$ so that

$$w_{sr} = \delta_{s,(\tilde{s}-1)(N_r-1)/(N_{\tilde{s}}-1)+1}.$$

4.2.1 Rationale

The simplest functional of measured and modelled signals whose global minimum occurs when true and modelled values of medium parameters coincide, is the sum-of-squared-differences (SSD). It suffers from *“cycle-skipping”* local maxima which give rise to local minima that frustrate gradient-based optimisation schemes. An alternative functional known as the Normalised Integration Method (NIM) overcomes the most important of the local maxima of SSD, but both SSD and NIM still suffer from local maxima that arise in a different way, due to *mutual interference* between reflected signals.

4.2.1.1 “Cycle-skipping” local maxima

The simpler obstacle to convexity was illustrated for the function $\mathcal{E}_{\text{SSD}}$ in Section 3.2.4. In the notation of Chapter 3, if, for one or more r and s and for some ϕ, the signals $p^{rs}(t;\phi)$ and $p^{*}_{sr}(t)$ differ approximately by a time translation of half a period, then comparison in Eq. 3.32, may result in a local maximum of $\mathcal{E}_{\text{SSD}}$. In seismology literature this phenomenon is commonly known as “cycle-skipping”.

4.2.1.2 Mutual interference local maxima

Plots of $\mathcal{E}_{\text{NIM}}$, defined in Eq. 3.34, and its gradient, shown in [125], indicated that, with transmission data, it could be used to locate a velocity perturbation more accurately and with fewer artifacts than $\mathcal{E}_{\text{SSD}}$ (Eq. 3.32) or either of two alternative versions of NIM that were presented, in which one of the two quantities

$$Q_1[p](t) = \frac{\int_0^t |p(t')|\,dt'}{\int_0^T |p(t')|\,dt'} \qquad Q_2[p](t) = \frac{\int_0^t p(t')^2\,dt'}{\int_0^T p(t')^2\,dt'}.$$

was substituted for the ratio in Eq. 4.1,

$$Q_{\text{NIM}}[p](t) = \frac{\int_0^t E[p](t')\,dt'}{\int_0^T E[p](t')\,dt'} \tag{4.1}$$

.

However, $\mathcal{E}_{\text{NIM}}$ can suffer from local maxima arising in a different way, in a situation where a constraint to a piece-wise constant medium is used, to reduce the dimensionality of the optimisation space, and the reference and model media are *misaligned*:

$$\mathcal{E}_{\text{NIM}}(\boldsymbol{\phi}) = \frac{1}{2}\sum_{s=1}^{N_s}\sum_{r=1}^{N_r}\int_0^T w_{rs}\Big[Q_{\text{NIM}}[p_{sr}](t;\boldsymbol{\phi}) - Q_{\text{NIM}}[p^*_{sr}](t)\Big]^2\,dt, \tag{4.2}$$

where

$$Q_{\text{NIM}}[p](t) = \frac{\int_0^t E[p](t')\,dt'}{\int_0^T E[p](t')\,dt'}.$$

For a given $\mathbf{x}_s$ and $\mathbf{x}_r$, the signal measured at $\mathbf{x}_r$ will be, in general, a sum of contributing signals travelling along different ray-paths from $\mathbf{x}_s$ to $\mathbf{x}_r$. *Mutual interference* between these contributions will clearly occur *before* application of the functional Q_{NIM}. A simple demonstration shows the effect that this can have on $\mathcal{E}_{\text{NIM}}$ when considered as a function of misalignment between model and reference media.

Figure 4.1 shows the set-up for the numerical demonstration. A line of source points send Gaussian pulses of centre frequency 1MHz and envelope standard deviation 1μs into a lossless, homogeneous medium. Reflections from two point scatterers, at depth d and spacing $2s$ are compared, for lateral displacements, Δx, to those for $\Delta x = 0$. The six plots in Fig. 4.2 show that the NIM cost function does not increase monotonically with deviation of Δx about 0. This is due to interference between echoes arriving at the same receiver from distinct reflection events. The envelope of the blue signal in the top middle plot has a smaller integral than those in the top left and top right. The three scenarios depicted in Fig. 4.2 correspond to the three points highlighted with black dots in Fig. 4.3.

To summarise, although $\mathcal{E}_{\text{NIM}}$ is designed to be

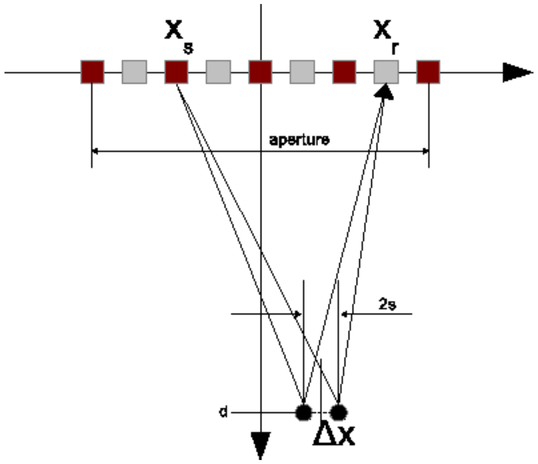

Figure 4.1: Geometry used to demonstrate the effect of mutual interference on the NIM

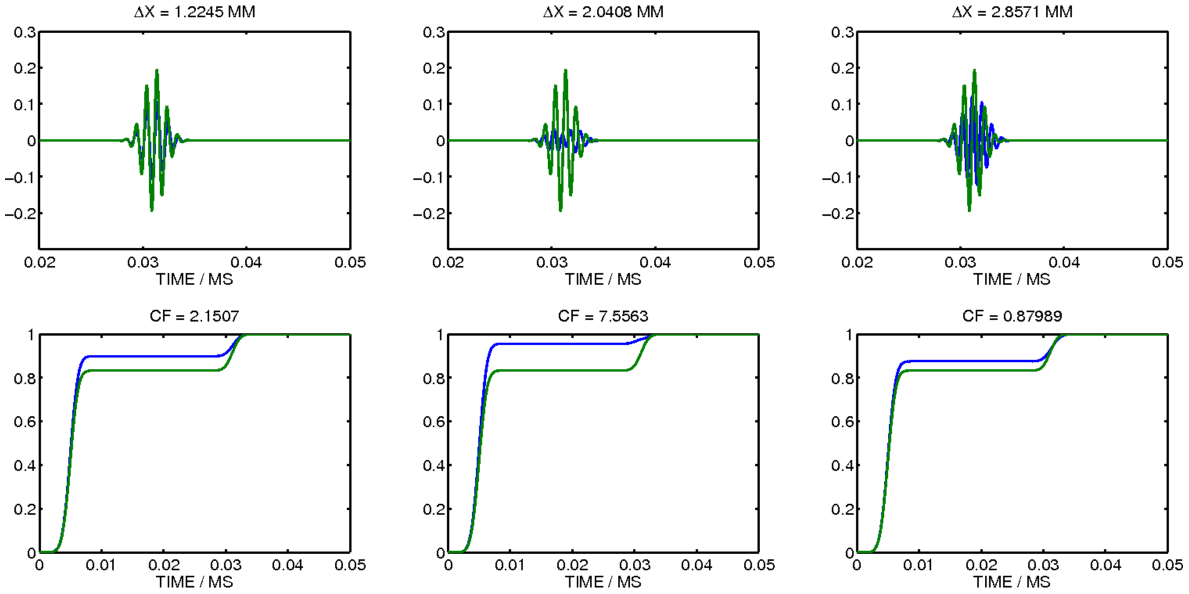

Figure 4.2: Top row: received echoes from two point scatterers at lateral displacement Δx (blue) and 0 (green). Bottom row: normalised integrated envelopes of displaced (blue) and reference (green) signals

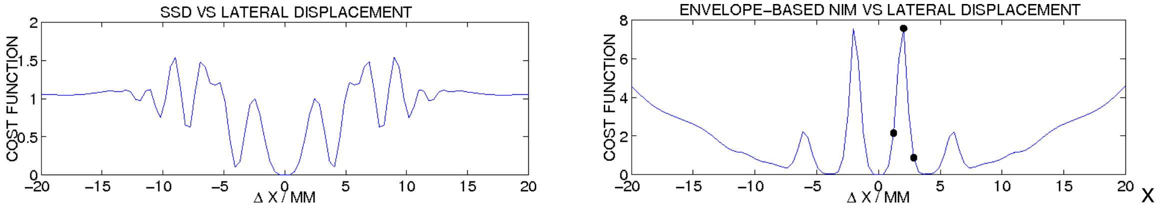

(a) $\mathcal{E}_{\text{SSD}}$

(b) $\mathcal{E}_{\text{NIM}}$

Figure 4.3: Model-reference misfit functions vs lateral displacement of scatterer pair. Left: summed-squared differences, Right: envelope-based Normalised Integration Method showing the three points corresponding to the three columns of Fig. 4.2

- convex in some neighbourhood of the sought model parameters, ϕ^*, due to the squaring operation, as seen for both $\mathcal{E}_{\mathsf{NIM}}$ and $\mathcal{E}_{\mathsf{SSD}}$ around $\Delta x = 0$ in both parts of Fig. 4.3,
- invariant with respect to changes in the phase of p_{sr}, due to the enveloping, which results in the absence, in Fig. 4.3(b), of most of the local minima seen in Fig. 4.3(a), and
- sensitive to the difference between the arrival time of a given individual reflected pulse in p_{sr}, and the corresponding pulse in p^*_{sr}, *even when these have no temporal overlap*, due to the integration, which results in the near-convexity seen in Fig. 4.3(b) for $|\Delta x| > 12mm$ compared to the corresponding near-plateaux seen in Fig. 4.3(a),

it is not convex with respect to deviations in model parameters (of the acoustic properties of the medium, or of its geometry) from their optimal values where these cause, say, the amplitude of p_{sr} to vary non-monotonically with respect to the deviations concerned. I show below how, by exploiting information from all receivers simultaneously, a more 'nearly convex' cost function can be constructed by attempting to *undo* the mutual interference such as that in seen in the top middle plot of Fig. 4.2, *before* the evaluation of a cost function similar to Eqn. 4.2.

4.2.2 The Echo-wise Normalised Integration Method

In this section, a mathematical definition of the *ENIM* signal dissimilarity criterion is given, and the novel steps involved in its computation are described in detail.

4.2.2.1 Cost function

Throughtout this section I use $p(t)$ to denote both $p(t;\boldsymbol{\phi})$ and $p^*(t)$ where the point being discussed applies equally to either. For source and receiver points as notated in Sec. 4.2.1, the ENIM signal dissimilarity cost function is defined by

$$\mathcal{E}_{\mathsf{ENIM}}(\boldsymbol{\phi}) = \frac{1}{2}\sum_{r,s}\sum_{m=1}^{M}\int_0^T \left| Q_{\mathsf{NIM}}[p_{sr\pi(m)}](t;\boldsymbol{\phi}) - Q_{\mathsf{NIM}}[p^*_{srm}](t)\right|^2 dt. \tag{4.3}$$

Here, π is a permutation, to be described shortly, and I call p_{srm} an *echo* signal received from one of M distinct *reflection events*, where M is a small pre-determined integer such that

$$p_{sr}(t) \approx \sum_{m=1}^{M} p_{srm}(t) \tag{4.4}$$

By 'reflection event' I mean a reflection of one or more acoustic rays from one side of a particular compartment interface within the medium, after a particular (possibly empty) sequence of "downward" transmissions of the ray(s) across a particular set of interfaces, and before a particular (possibly empty) sequence of "upward" transmissions across another (possibly different) particular set of interfaces. Multiple reflections are not considered. The attempt to separate each received signal trace,

$p_{sr}(t)\colon t \in [0,T]$ into such 'echoes', with labels $1 \leq m \leq M$ assigned so that the echoes labelled with the same m, i.e.

$$\{p_{srm}(t)\colon s = 1,\ldots,N_s,\ r = 1,\ldots,N_r,\ t \in [0,T]\}$$

all contain information about *the same reflection event*, is central to the approach.

(a)(b)(c)(d)(e)(f) (g)(h) (i) (j)

Figure 4.4: Illustrative (idealised) signal decomposition for $\mathrm{E}_{\mathrm{ENIM}}$

Echo pulses are estimated, for a complete set of received signals, in two stages for reference signals, and in three stages for modelled signals. For reference (i.e. “observed”) signals, $\{p^*_{sr}(t)\colon t \in [0,T]\}_{s=1,r=1}^{N_s,N_r}$, the first stage estimates the *arrival times* of reflections from each of M distinct interfaces in the medium. The second stage estimates the echo amplitudes using information from all signals at once. For the modelled signals, $\{p_{sr}(t;\boldsymbol{\phi})\colon t \in [0,T]\}_{s=1,r=1}^{N_s,N_r}$, an intermediate stage attempts to choose a permutation $\boldsymbol{\pi}$ so that, for each m, the sets of signals $\{p_{sr\boldsymbol{\pi}(m)}\}_{s,r}^{N_s,N_r}$ and $\{p^*_{srm}\}_{s,r}^{N_s,N_r}$ correspond to the same reflection event.

4.2.2.2 “Echo” arrival time estimation

The output of this stage is a set of initial estimates of times, $\{\tilde{t}_{srm}\}$ at which reflected signals either are detected in $p_{sr}(t)$, for each s and r, or *would have been detected* had not propagating wavefronts contributing to $\{p_{sr}\}_r^{N_r}$ (for some s) interfered (constructively or destructively) *at* one or more of the $\mathbf{x}_r$. Recalling that $\mathbf{x}_s = (x_s, 0)$ and $\mathbf{x}_r = (x_r, 0)$, I mostly label the transceiver positions by their lateral co-ordinates in the following. Each $\{p_{sr}(t)\colon t \in [0,T]\}$ is referred to as a *trace*. The first step searches for reflection arrival times trace-by-trace, i.e. (s,r)-by-(s,r). Since the arrival times estimated at this step were to be refined subsequently, the following relatively simple and well-established method was used to estimate them (see also [135] and Alg. 3). An “energy” function, W, is defined as the squared modulus of the correlation of the signal $p_{sr}(t)$ with the *analytic* version, $q_a(t)$, of a template pulse, $q(t)$:

$$\begin{aligned}
W(t) &= \left| \int_0^T p_{sr}(t+\tau) q_a(\tau)\, d\tau \right|^2 \\
&= \left| \int_0^T p_{sr}(t+\tau)(q + iH[q])(\tau)\, d\tau \right|^2 && (4.5)\\
&= \left| \int_0^T p_{sr}(t+\tau) q(\tau)\, d\tau \right|^2 + \left| \int_0^T p_{sr}(t+\tau) H[q](\tau)\, d\tau \right|^2 && (4.6)
\end{aligned}$$

Figure 4.5: example signal plot

where q is a Gaussian-modulated sinusoidal pulse, with a relatively simple Hilbert transform:

$$q(t) = e^{\frac{(t-T/2)^2}{2\sigma^2}} \sin[2\pi f_0(t - T/2)], \quad t \in [0, T],$$

and

$$\begin{aligned} H[q](t) &= -e^{\frac{(t-T/2)^2}{2\sigma^2}} \cos[2\pi f_0(t - T/2)], \\ q_a(t) &= e^{\frac{(t-T/2)^2}{2\sigma^2}} \exp[(2\pi i f_0(t - T/2) - \pi i/2)], \quad t \in [0, T]. \end{aligned}$$

The analytical pulse is used in order to ensure that the point of maximum amplitude of a given pulse within p_{sr} is identified independently of its phase: if p_{sr} contained a pulse which was an *even* function, such as an enveloped cosine, translated to be centred on $t = T/2$, a correlation with q alone would produce *zero* at the pulse centre:

$$\begin{aligned} \left| \int_0^T p_{sr}(0+\tau) q(\tau)\, d\tau \right|^2 &= \left| \int_0^T \Big(f_+(0+\tau - T/2) \cos[2\pi f_0(0+\tau - T/2)] \Big) \Big(e^{\frac{(\tau-T/2)^2}{2\sigma^2}} \sin[2\pi f_0(\tau - T/2)] \Big)\, d\tau \right|^2 \\ &= 0 \end{aligned}$$

for any f_+ with $f_+(-t - T/2) = f_+(t - T/2)$.

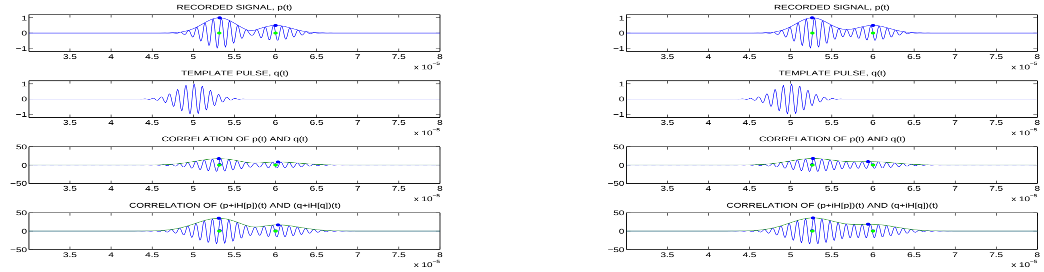

(a) $t_{\text{sep}} = 6.84\mu s$

(b) $t_{\text{sep}} = 7.37\mu s$

Figure 4.6: Numerical signals comprising the sum of two pulses, with a template pulse and correlations with that template. Plot sets (a) and (b) show two different values for the temporal separation of the original pulses. Blue dots show maxima in envelopes and green dots show pulse centre times.

The times of the M highest peaks in $W(t)$, for a pre-determined number M, estimate the arrival times of the M maximal echo pulses at $\mathbf{x}_r$ following transmission from $\mathbf{x}_s$. The echo arrival times found in this way, $\{t_{srm}\}_{s=1,r=1,m=1}^{N_s,N_r,M}$, may be corrupted where echoes arrive suffciently close together to interfere; they may *omit* some underlying but hidden arrival times, or include spurious ones. To ameliorate this, they are refined by combining information across multiple traces.

4.2.2.3 Arrival time clustering and refinement

The output of this stage is a matrix of fitting coefficients, $(a_{i,m})_{i=1,m=1}^{6,M}$, describing M surfaces in $(\mathbf{x}_s, \mathbf{x}_r, t)$-space fitted to the squared *travel* times. These are denoted $\{\tilde{t}^{sq}_{srm}\}$, for mathematical etiquette so as to provide a name, divorced from the squaring operation, for the image points of the mapping below. Subsequent to this fitting, the $\{\tilde{t}^{sq}_{srm}\}$ themselves are re-estimated as the intersections of the $N_s N_r$ lines $\{(\mathbf{x}_s, \mathbf{x}_r, t) : t \in [0, T]\}$ with the surfaces. The raw travel times are transformed as

$$\tilde{t}^{sq}_{srm} := \tilde{t}^2_{srm} = (t_{srm} - t_0)^2,$$

and a travel-time *surface*, $\mathcal{T}_m$, is assumed to exist for each m with

$$\mathcal{T}_m : \mathbb{R}^2 \to \mathbb{R}, \tag{4.7}$$

$$\mathcal{T}_m : (x_s, x_r) \mapsto \tilde{t}^{sq}_{srm}; \tag{4.8}$$

that is, $\mathcal{T}_m$ maps transceiver co-ordinates to squared travel times. To a good approximation, each $\mathcal{T}_m$ may be described as a linear combination of simple functions of x_s and x_r. I assume that:

- Each reflection event may be treated as having occurred at a point scatterer or a straight line reflector
- $\mathcal{T}_m(x_s, x_r) = \mathcal{T}_m(x_r, x_s)$, owing to the principle of acoustic reciprocity

The dependence of the two-way travel times, $\tilde{t}$, of reflected acoustic signals on source and receiver co-ordinates, for ray-based propagation with constant speed and simple reflector geometries, are given in introductory texts on reflection seismology, e.g. [140, 141, 142] and Appendix E. In the present notation we have, for a horizontal reflecting interface at depth y_D below $\mathbf{x}_s$ and $\mathbf{x}_r$,

$$c^2\tilde{t}^2 = 4y_D^2 + |x_r - x_s|^2. \tag{4.9}$$

For a straight reflecting interface at an angle, ξ, to the horizontal (the line joining $\mathbf{x}_s$ and $\mathbf{x}_s$), at a normal distance y_D from $\mathbf{x}_s$,

$$c^2\tilde{t}^2 = (2y_D \cos\xi)^2 + (|x_r - x_s| + 2y_D \sin\xi)^2. \tag{4.10}$$

Finally, considering a point scatterer with co-ordinates $\mathbf{x}_D = (x_D, y_D)^T$,

$$
\begin{aligned}
\tilde{t} &= \frac{1}{c}\sqrt{|x_D - x_s|^2 + y_D^2} + \frac{1}{c}\sqrt{|x_r - x_D|^2 + y_D^2} \\
c^2\tilde{t}^2 &= |x_D - x_s|^2 + y_D^2 + |x_r - x_D|^2 + y_D^2 + \\
&\sqrt{|x_D - x_s|^2 \cdot |x_r - x_D|^2 + y_D^2\Big(|x_D - x_s|^2 + |x_r - x_D|^2\Big) + y_D^4}
\end{aligned}
\tag{4.11}
$$

I seek a relatively simple parametrization of the $\tilde{t}^{sq}$ from Eqn 4.7 that generalises all of Eqns 4.9, 4.10 and 4.11, noting that it must be symmetric with respect to the exchange $s \leftrightarrow r$. With the assumption that $|x_r - x_s| < y_D$, one may rewrite the square root of Eqn 4.11 and use a binomial approximation:

$$
\begin{aligned}
c^2\tilde{t}^2 &= 2x_D^2 + 2y_D^2 - 2x_D(x_s + x_r) + y_D^2\left(1 + \frac{(x_D - x_s)^2}{y_D^2} + \frac{(x_r - x_D)^2}{y_D^2} + \frac{(x_D - x_s)^2(x_r - x_D)^2}{y_D^4}\right)^{1/2} \\
&= 2x_D^2 + 2y_D^2 - 2x_D(x_s + x_r) + y_D^2\left(1 + \frac{(x_D - x_s)^2}{2y_D^2} + \frac{(x_r - x_D)^2}{2y_D^2} + \cancelto{\approx 0}{\frac{(x_D - x_s)^2(x_r - x_D)^2}{2y_D^4}} + \dots\right) \\
&\approx 2x_D^2 + 2y_D^2 - 2x_D(x_s + x_r) + y_D^2\left(1 + \frac{(x_D - x_s)^2 + (x_r - x_D)^2}{2y_D^2}\right) \\
&= 2x_D^2 + 2y_D^2 - 2x_D(x_s + x_r) + y_D^2\left(1 + \frac{1}{2y_D^2}\left(\frac{1}{2}\left[(x_r + x_s)^2 + (x_r - x_s)^2\right] - x_D(x_r + x_s) + 2x_D^2\right)\right)
\end{aligned}
\tag{4.12}
$$

On comparing the forms of 4.12 with those of Eqns 4.9 and 4.10, it will be seen that the following linear combination of quadratic functions of $|x_r + x_s|$ and $|x_r - x_s|$ suffices to describe, to the quadratic approximation in $|x_r - x_s|/y_D$, any of the three arrival-time “surfaces”, for fixed x_D, y_D:

$$
\begin{aligned}
\tilde{t}^{sq}_{srm} = a_{0,m} + a_{1,m}|x_s - x_r| + a_{2,m}|x_s + x_r| + a_{3,m}|x_s - x_r|^2 + \\
a_{4,m}|x_s - x_r| \cdot |x_s + x_r| + a_{5,m}|x_s + x_r|^2.
\end{aligned}
\tag{4.13}
$$

The estimation of the coefficients, $\{a_{k,m}\}_{k=0,m=1}^{5,M}$, is done in two stages. In the first stage, a set of initial estimates is found by alternately fitting one surface using the Random Sample Consensus Algorithm (RANSAC), and excluding the points deemed to lie in that surface from the remaining points to be fitted until M surfaces have been fitted. The estimates are used to initialise an adaptation of the Simultaneous Robust Multiple Fitting algorithm (SRMF or ’SMRF’) described in [139]. In early tests, the SMRF algorithm was found to give highly reproducible $\{a_{k,m}\}_{k=0,m=1}^{5,M}$, but also to require a close initialisation. The RANSAC algorithm, on the other hand, appeared to produce visually sensible surface fits from poor starting estimates, but with less reproducibility (see Fig’s **??** and **??**). Algorithms 4 (the RANSAC stage) and 5 (the SMRF stage) refer to X, a Vandermonde-type matrix for use in Eqn. 4.13:

$$\mathsf{X} \equiv \begin{bmatrix} 1 & |x_1 - x_1| & |x_1 + x_1| & |x_1 - x_1|^2 & |x_1 - x_1| \cdot |x_1 + x_1| & |x_1 + x_1|^2 \\ 1 & |x_1 - x_2| & |x_1 + x_2| & |x_1 - x_2|^2 & |x_1 - x_2| \cdot |x_1 + x_2| & |x_1 + x_2|^2 \\ \vdots & \vdots & \vdots & \vdots & \vdots & \vdots \\ 1 & |x_s - x_r| & |x_s + x_r| & |x_s - x_r|^2 & |x_s - x_r| \cdot |x_s + x_r| & |x_s + x_r|^2 \\ \vdots & \vdots & \vdots & \vdots & \vdots & \vdots \\ 1 & |x_{N_s} - x_{N_r}| & |x_{N_s} + x_{N_r}| & |x_{N_s} - x_{N_r}|^2 & |x_{N_s} - x_{N_r}| \cdot |x_{N_s} + x_{N_r}| & |x_{N_s} + x_{N_r}|^2 \end{bmatrix}. \tag{4.14}$$

Algorithm 3 Extraction of initial echo arrival times

```
define $q$ and $q_a = q + iH[q]$
for $(s, r) \in \{1, \dots, N_s\} \times \{1, \dots, N_r\}$ do
    compute cross-correlation,$R_{sr}(t)$, between $p_{sr}(t))$ and $q_a(t)$
    compute $\{W(t) = |R_{sr}(t)|^2 : t \in [0, T]\}$
    identify the locations of the $M$ highest maxima of $W$ using MATLAB's findpeaks routine
end for
```

In Alg. 5, the function ϕ is defined by

$$\phi(\cdot) = \frac{1}{a}\left(\left(\frac{1}{\cdot}\right)^a - 1\right)$$

and F is a block-diagonal matrix whose M blocks are the 6×6 matrices $\sum_{i=1}^{N_s N_r} \lambda^k_{im} \mathsf{X}^T_{i,:} \mathsf{X}_{i,:}$.

4.2.2.4 Echo amplitude and phase estimation

The 'echoes' are pulses defined by

$$\begin{aligned} p_{srm}(t) &:= x_m \, \hat{p}_{srm} \\ &= x_m \, \psi(\tilde{t}_{srm}) \, \tilde{p}_{srm}, \end{aligned} \tag{4.15}$$

where, x_m is a fitting parameter and the function ψ is a simple pulse amplitude model, to account approximately for cylindrical spreading loss (i.e. 'spherical' spreading in 2-D):

$$\psi(t) \equiv \begin{cases} 1/\sqrt{t} & \text{for} \quad t \neq 0 \\ 1 & \text{for} \quad t = 0 \end{cases} \tag{4.16}$$

and $\tilde{p}_{srm}$ is a unit-amplitude Gaussian pulse centred on $\tilde{t}_{srm}$ given by

$$\tilde{p}_{srm}(t) = e^{\frac{(t - \tilde{t}_{srm})^2}{2\sigma^2}} e^{2\pi i f_0 (t - \tilde{t}_{srm})}, \quad t \in [0, T] \tag{4.17}$$

Algorithm 4 Clustering of echo arrival times by linear least-squares paraboloid surface fitting

```
Let $S$ be the set of correlation peaks found in Alg. 3: $P = \{(x_r, x_s, t_{srm})\}$, and let $N = |P|$
transform the $t$-components of these points, so that $P = \{(x_r, x_s, \tilde{t}^{sq}_{srm})\}$
Let X be as defined in Eq. 4.14
set maxIter, threshDist and num for RANSAC clustering/fitting
for $m = 1, \ldots, M$ do
  set RANSAC inlierRatio to $1/4(M - m + 1)$
  set $\{a_{k,m}\}_{k=0}^{5}$ to NaN
  set bestInNum=0
  for $i = 1, \ldots,$ maxIter do
    select, at random, points, $P_i = \{(x_r, x_s, \tilde{t}_{srm})\}$, with $P_i \subset S$ and $|P_i|$ =num
    define $\mathsf{X}_{P_i}$ as the submatrix of X corresponding the points in $P_i$
    define $\tilde{\mathbf{t}}_{P_i}$ as the vector of $\tilde{t}$-co-ordinates of the points in $P_i$
    compute $\tilde{\mathbf{a}} = (\mathsf{X}_{P_i}^{\mathsf{T}} \mathsf{X}_{P_i})^{-1} \mathsf{X}_{P_i}^{\mathsf{T}} \tilde{\mathbf{t}}_{P_i}$
    compute temporal distances of all points in $P$ from the surface defined by $\tilde{\mathbf{a}}$ as $|\mathsf{X}\tilde{\mathbf{a}} - \tilde{\mathbf{t}}|$
    set $P' = \{(x_r, x_s, \tilde{t}_{srm})\colon |\mathsf{X}\tilde{\mathbf{a}} - \tilde{\mathbf{t}}| <$ threshDist$\}$, with inlierNum$= |P'|$
    if inlierNum$>$inlierRatio$\cdot N$ and inlierNum$>$bestInNum and $\tilde{a}_{3,m} > 0$ and $\tilde{a}_{5,m} > 0$
    then
      set bestInNum = inlierNum
      set $\{a_{k,m}\}_{k=0}^{5}$ to the elements of $\tilde{\mathbf{a}}$
    end if
  end for
  set $\tilde{\mathbf{t}}_{P'}$ to the time co-ordinates of points in $P'$, and recompute $\{a_{k,m}\}_{k=0}^{5}$ as the elements of
  $\mathbf{a} = (\mathsf{X}_{P'}^{\mathsf{T}} \mathsf{X}_{P'})^{-1} \mathsf{X}_{P'}^{\mathsf{T}} \tilde{\mathbf{t}}_{P'}$
  set $P = P \setminus P'$
end for
compute $\{t_{srm}\}_{s=1,r=1,m=1}^{N_s,N_r,M}$ as XA with A $= (a_{k,m})$
```

Algorithm 5 Final estimation of echo arrival times using the Simultaneous Robust Multiple Fitting algorithm, adapted from [139]

```
set maxIter, change, $\epsilon'$, $\epsilon$, $\sigma$, $a$
set $\mathsf{A}^{(0)}$ to the A found by Alg. 4
for $k = 1 :$ maxIter do
  while change $> \epsilon'$ do
    for $i = 1 : N_s N_r$ do
      $s = \lfloor i/N_r \rfloor + 1$
      $r = i/N_r - \lfloor i/N_r \rfloor$
      let $y_i = \tilde{t}_{srm}$
      for $m = 1 : M$ do
        set $w_{im}^k = \left( \frac{\mathsf{X}_{i,:} \mathsf{A}_{:,m}^{(k-1)} - y_i}{\sigma} \right)^2$
        set $\lambda_{im}^k = \frac{\epsilon + \exp(-\frac{1}{2}\phi(w_{im}^k))}{m\epsilon + \sum_{m=1}^{M} \exp(-\frac{1}{2}\phi(w_{im}^k))} \phi'(w_{im}^k)$
      end for
    end for
    compute $\mathsf{A}^{(k)} = \mathsf{F}^{-1} \begin{bmatrix} \sum_{i=1}^{N_s N_r} \lambda_{i1}^k y_i \mathsf{X}_{i,:} \\ \vdots \\ \sum_{i=1}^{N_s N_r} \lambda_{iM}^k y_i \mathsf{X}_{i,:} \end{bmatrix}$
    set change$= \|A^{(k)} - A^{(k-1)}\|_2$
  end while
end for
```

From Eq'ns 4.15 and 4.4, we have

$$\begin{aligned} p_{sr}(t) &= \sum_{m=1}^{M} x_m\,\hat{p}_{srm}(t) \\ &= \sum_{m=1}^{M} x_m\,\psi(\tilde{t}_{srm})\,\tilde{p}_{srm}(t). \end{aligned} \tag{4.18}$$

The ψ and $\tilde{p}_{srm}(t)$ having been determined via the fitted $\tilde{t}_{srm}$ for s, r, and m, the x_m can be found by a second fitting procedure. Since the m-label of each reflection event present in the signals is now known from the fitting of their arrival times, $\tilde{t}_{srm}$, no further clustering is needed, so that a relatively simple linear least-squares fitting suffices for this step. Owing to residual inaccuracy in the $\tilde{t}_{srm}$ and to phase differences between echoes present in the $\{p_{sr}\}$, this was found to work best in two stages, fitting the echoes' amplitudes in the first stage, and their phases in an independent second stage. With the discretization $t_n = n\Delta t\colon n = 0, \ldots, N_t$, where $(N_t - 1)\Delta t = T$, and $L = N_s N_r N_t$, the $L \times M$ matrices T_1, T_2 and $L \times 1$ vectors S_1, S_2 are defined as follows, with $H[.]$ again, denoting the Hilbert transform:

$$\mathsf{T}_1 \equiv \begin{bmatrix} \uparrow & \uparrow & & \uparrow \\ |\hat{p}_{111}| & |\hat{p}_{112}| & \cdots & |\hat{p}_{11M}| \\ \downarrow & \downarrow & & \downarrow \\ \uparrow & \uparrow & & \uparrow \\ |\hat{p}_{121}| & |\hat{p}_{122}| & \cdots & |\hat{p}_{12M}| \\ \downarrow & \downarrow & & \downarrow \\ \vdots & \vdots & \vdots & \vdots \\ \uparrow & \uparrow & & \uparrow \\ |\hat{p}_{N_sN_r11}| & |\hat{p}_{N_sN_r12}| & \cdots & |\hat{p}_{N_sN_r1M}| \\ \downarrow & \downarrow & & \downarrow \end{bmatrix}, \quad \mathsf{T}_2 \equiv \begin{bmatrix} \uparrow & \uparrow & & \uparrow \\ x_1^1\hat{p}_{111} & x_2^1\hat{p}_{112} & \cdots & x_M^1\hat{p}_{11M} \\ \downarrow & \downarrow & & \downarrow \\ \uparrow & \uparrow & & \uparrow \\ x_1^1\hat{p}_{121} & x_2^1\hat{p}_{122} & \cdots & x_M^1\hat{p}_{12M} \\ \downarrow & \downarrow & & \downarrow \\ \vdots & \vdots & \vdots & \vdots \\ \uparrow & \uparrow & & \uparrow \\ x_1^1\hat{p}_{N_sN_r11} & x_2^1\hat{p}_{N_sN_r12} & \cdots & x_M^1\hat{p}_{N_sN_r1M} \\ \downarrow & \downarrow & & \downarrow \end{bmatrix},$$

$$\mathsf{S}_1 \equiv \begin{bmatrix} \uparrow \\ |p_{11} + iH[p_{11}]| \\ \downarrow \\ \uparrow \\ |p_{12} + iH[p_{12}]| \\ \downarrow \\ \vdots \\ \uparrow \\ |p_{N_sN_r} + iH[p_{N_sN_r}]| \\ \downarrow \end{bmatrix}, \quad \mathsf{S}_2 \equiv \begin{bmatrix} \uparrow \\ p_{11} + iH[p_{11}] \\ \downarrow \\ \uparrow \\ p_{12} + iH[p_{12}] \\ \downarrow \\ \vdots \\ \uparrow \\ p_{N_sN_r} + iH[p_{N_sN_r}] \\ \downarrow \end{bmatrix}.$$

Equation 4.19, over and above Eqn 4.18, though not valid in general, was found in early tests to yield sensible values for the $\{x_m\}$ in Eqn 4.18, and was used to estimate echo *amplitudes*, in outline, via Eqn 4.20

$$E[p_{sr}](t) = \sum_{m=1}^{M} x_m \, \psi(\tilde{t}_{srm}) \, E[\tilde{p}_{srm}](t), \tag{4.19}$$

$$\mathsf{T_1 x^1 = S_1} \quad \text{as} \quad \mathsf{x^1 = (T_1{}^T T_1 + \alpha I)^{-1} T_1{}^T S_1}, \tag{4.20}$$

where $\alpha \ll 1$. Then echo phase information is incorported via Eqn 4.21:

$$\mathsf{T_2 x^2 = S_2} \quad \text{as} \quad \mathsf{x^2 = (T_2{}^T T_2 + \alpha I)^{-1} T_2{}^T S_2}, \tag{4.21}$$

with the $\{x_m\}$ in Eqn 4.18 finally estimated as the elements of

$$\mathsf{x} = \frac{\mathsf{x_2}}{|\mathsf{x_2}|}. \tag{4.22}$$

In practice, because $1/\sqrt{\tilde{t}_{srm}}$ is undefined for $r = s$ (where $\tilde{t}_{srm} = 0$), ψ is given the second definition in Eqn 4.16 for these cases, and Eqn's 4.20 and 4.21 must be similarly split into “finite travel time” and “zero travel time” cases. Submatrices $\mathsf{T_i{}^{ft}}$ and $\mathsf{T_i{}^{zt}}$ contain those rows of $\mathsf{T_i}$ where, respectively, $r \neq s$ and $r = s$. Assuming that the “zero travel time” pulse present in each p_{ss} overlaps negligibly with any other pulse in the same p_{ss}, Eqn's 4.20, 4.21 may be restated in the form

$$\mathsf{T_i{}^{ft} x^{i^{ft}} + T_i{}^{zt} x^{i^{zt}} = S_i}, \tag{4.23}$$

where

$$\mathsf{T_i{}^{ft} x^{i^{ft}} = S_i}, \quad \text{and} \quad \mathsf{T_i{}^{zt} x^{i^{zt}} = S_i} \tag{4.24}$$

give

$$\mathsf{x^{i^{ft}} = (T_i{}^{ftT} T_i{}^{ft} + \alpha I)^{-1} T_i{}^{ftT} S_i}, \quad \text{and} \quad \mathsf{x^{i^{zt}} = (T_i{}^{ztT} T_i{}^{zt} + \alpha I)^{-1} T_i{}^{ztT} S_i}. \tag{4.25}$$

4.2.2.5 Arrival time surface matching

Even when the echo arrival times initially estimated, for the (s, r)-th trace, with a given set of model parameters, correspond to the same M reflection events as those for the (s, r)-th trace with a different set of model parameters, the order in which they are recorded depends, in each case, upon the size order of the M highest peaks in $W(t)$, and so may differ if two or more reflection events produce echoes which are close in amplitude. This fact, combined with the stochastic nature of Alg.

4, means that modelled echoes, $\{p_{srm}\}$, and reference/observed echoes, $\{p^*_{srm}\}$, may not contain information about the 'mth' reflection event. Consider $\{\mathcal{T}_m \colon m = 1, \ldots, M\}$ to be the set of arrival time surfaces extracted from the modeled pressure signals, and similarly for reference/observed signals $\{\mathcal{T}^*_m \colon m = 1, \ldots, M\}$. To correct any mis-ordering, I seek the permutation, π of $\{1, 2, \ldots, M\}$ so that the *ordered* set $\left(\mathcal{T}_{\pi(m)}\right)_{m=1}^{M}$ corresponds to $(\mathcal{T}^*_m)_{m=1}^{M}$ as well as possible: specifically, so that the sum of absolute differences between the surfaces' constant paraboloid coefficients be minimal. For a small M it is computationally trivial to search the $M!$ permutations exhaustively:

$$\boldsymbol{\pi} = \mathrm{argmin}_{\boldsymbol{\pi}' \in S_M} \sum_{m=1}^{M} \left| a_{0,\boldsymbol{\pi}'(m)} - a^*_{0,m} \right|. \tag{4.26}$$

4.2.3 Computation of $\nabla\mathcal{E}_{\mathsf{ENIM}}$ by the adjoint field method

Working along similar lines to those of Section 3.2.7, I have attempted to compute the gradient of the *ENIM* criterion with respect to density and bulk modulus using the adjoint method. To recap, derivatives of the field computed for each source, $p(\mathbf{x}, t; \mathbf{x}_s, \boldsymbol{\phi})$ are correlated in time with those of another field, $p^\dagger(\mathbf{x}, t; \{\mathbf{x}_r\}_{r=1}^{N_r}, \boldsymbol{\phi})$ computed as the solution to an "adjoint" wave equation. Most of the work involved is in the calculation of the correct source term for this equation: $\sum_{r=1}^{N_r}(\mathbf{x}_r, t; \mathbf{x}_s)$. An expression for the rth summand is derived below.

$$\begin{aligned}
S(\mathbf{x}_r, t; \mathbf{x}_s) &= \frac{\partial \mathcal{E}_{\mathsf{ENIM}}}{\partial p_{sr}(t)} \\
&= \sum_{s'} \sum_{r'} \sum_{m} \int_0^T \frac{\partial \mathcal{E}_{\mathsf{ENIM}}}{\partial p_{s'r'\pi(m)}(t')} \frac{\partial p_{s'r'\pi(m)}(t')}{\partial p_{sr}(t)}\, dt' \\
&= \sum_{s'} \sum_{r'} \sum_{m} \int_0^T \int_0^T \overbrace{\frac{\partial \mathcal{E}_{\mathsf{ENIM}}}{\partial Q_{\mathsf{NIM}}[p_{s'r'\pi(m)}](t'')}}^{\mathsf{C}} \overbrace{\frac{\partial Q_{\mathsf{NIM}}[p_{s'r'\pi(m)}](t'')}{\partial p_{s'r'\pi(m)}(t')}}^{\mathsf{B}}\, dt'' \overbrace{\frac{\partial p_{s'r'\pi(m)}(t')}{\partial p_{sr}(t)}}^{\mathsf{D}}\, dt'
\end{aligned} \tag{4.27}$$

Since echo is estimated using all traces, $p_{s'r'm}$ clearly depends, in practice, on p_{sr} for which $s \neq s'$ and $r \neq r'$. However, under the assumption that the echo fitting described in the previous sections works perfectly, it can be shown that,

$$\frac{\partial p_{s'r'\pi(m)}(k'\Delta t)}{\partial p_{sr}(k\Delta t)} = \delta_{ss'}\delta_{rr'}\delta_{kk'}. \tag{4.28}$$

To see this, consider that, with perfect echo fitting, the following relation holds.

$$\left(\sum_{m=1}^{M} p_{srm}(t) \right) - p_{sr}(t) = 0, \quad \forall 1 \leq s \leq n_s, 1 \leq r \leq n_r, t = k\Delta t : 1 \leq k \leq n_t.$$

Also, considering the tuples of quantities $(p_{srm}(t))_{s=1,r=1,k=1,m=1}^{n_s,n_r,n_t,M}$ and $(p_{sr}(t))_{s=1,r=1,k=1}^{n_s,n_r,n_t}$ to be elements of the finite-dimensional vector spaces $\mathbb{R}^{n_s n_r n_t M}$ and $\mathbb{R}^{n_s n_r n_t}$, respectively, the following function can be defined:

$$F : \mathbb{R}^{n_s n_r n_t M} \times \mathbb{R}^{n_s n_r n_t} \to \mathbb{R}^{n_s n_r n_t}$$

$$F : (\mathbf{x}, \mathbf{y}) \mapsto \left(\sum_{m=1}^{M} x_\alpha \right) - y_\alpha,$$

where α is a multi-index representing (s, r, k), so that the output of F is $n_s n_r n_t$-valued. Clearly F is continuously differentiable with respect to its arguments. The implicit function theorem states that, given a particular $(\mathbf{a}, \mathbf{b})$ for which $F(\mathbf{a}, \mathbf{b}) = \mathbf{0}$, if the Jacobian matrix,

$$J_{F,\mathbf{y}}(\mathbf{a}, \mathbf{b}) = \frac{\partial F_\alpha}{\partial y_\beta}_{(\mathbf{a},\mathbf{b})},$$

is invertible, then there exists an open set $U \subset \mathbb{R}^{n_s n_r n_t M}$ containing $\mathbf{a}$, and a unique continuously differentiable function $g : U \to \mathbb{R}^{n_s n_r n_t}$ such that $g(\mathbf{a}) = \mathbf{b}$, and its partial derivatives are given by

$$\frac{\partial g}{\partial x_\beta}(\mathbf{x}) = -J_{F,\mathbf{y}}(\mathbf{x}, g(\mathbf{x}))^{-1} \frac{\partial F}{\partial x_j}(\mathbf{x}, g(\mathbf{x})).$$

With the F above,

$$\frac{\partial F_\alpha}{\partial y_\beta} = -\delta_{\alpha\beta}$$

so that

$$-J_{F,\mathbf{y}}(\mathbf{x}, \mathbf{y})^{-1} = \delta_{\alpha\beta}.$$

Provided that this can be extended validly to infinite-dimensional spaces, Eq. 4.28 becomes

$$\frac{\partial p_{s'r'\pi(m)}(t')}{\partial p_{sr}(t)} = \delta_{ss'}\delta_{rr'}\delta(t - t'), \tag{4.29}$$

so that, finally, from Eq. 4.27,

$$S(\mathbf{x}_r, t; \mathbf{x}_s) = \sum_m \int_0^T \frac{\partial \mathcal{E}_{\text{ENIM}}}{\partial Q_{\text{NIM}}[p_{sr\pi(m)}](t'')} \frac{\partial Q_{\text{NIM}}[p_{sr\pi(m)}](t'')}{\partial p_{sr\pi(m)}(t)}\, dt'' \tag{4.30}$$

4.2.4 Experiments with simulated data

4.3 Results

4.4 Discussion

4.5 Conclusions

Chapter 5

Image-based registration of US to CT/MR abdominal images

5.1 Introduction

5.1.1 Overview

The work in this chapter is intended to address the subsidiary aim given in Chap. 1 in as well-controlled an environment as possible. Section 5.2.1 explains the technique I have used to simulate ultrasound images, and the rest of Sec. 5.2 describes two sets of experiments performed to evaluate the accuracy and robustness of a registration algorithm based on this against others current in the literature. This technique is based on the approach of Wein et al. [116] with two key stipulations in mind: first, that the finished system be applicable for *any* available pre-operative imaging modality that contains sufficient anatomical information to build a geometrical model of the organ(s) of interest through which the US beam passes, and, secondly, that any (acoustic) model parameters be physically meaningful and explicit. I include, also, a generalisation of Grau and Noble's *local phase and orientation* image similarity criterion.

5.1.2 Purpose

Accurate and robust registration between ultrasound and either CT or MR images is an important task in the guidance of abdominal soft tissue HIFU. The acoustic ray paths from any ultrasound transducer involved need to be localised within the planning anatomy. This includes both the therapeutic transducer array and any device used to acquire reflection signals for use in a reflection tomography scheme such as that outlined in the preceding two chapters. Multimodal image registration is a very active field of research but, to my knowledge, there are few comparisons of the most popular methods for US-CT or US-MR registration on the same task.

5.1.3 Related work

Perhaps the first proposal to address the problems discussed in 2.5 via a physically-based ultrasound image *simulation* was presented by Wein et al. in [116]. Using a simple model of ultrasound beam propagation based on diffuse reflection directly anti-parallel to the incidence direction at boundaries of changing acoustic impedance, the authors generated simulations representing the components of B-mode ultrasound sectors due to reflection and to the consequent attenuation (shadowing). The X-ray attenuation coefficients given by CT data, are assumed to be proportional to density, and so, assuming a constant sound speed, to acoustic impedance. Thus a sector-shaped re-sliced region from the CT data is used as a surrogate acoustic impedance map for each required field-of-view, since only ratios of these impedances are required in the physical equations. The assumption of constant sound speed across tissues is not explicitly justified, although the fact that ultrasound machines assume a constant speed of 1540ms^{-1} in soft tissues is mentioned. Additionally, the proportion of incident intensity that is transmitted across a boundary is assumed to be independent of incidence direction, since refraction is ignored. Ignoring refraction to assume straight-line propagation introduces spatial distortion in the resulting simulated image, but justified for this purpose since real US image construction also makes this assumption. After a log-compression step, the resulting image intensity, as a function of mapped position within the sector field-of-view (FOV) and with respect to the CT volume, μ. is given by equation 5.1. This mimics the transmission/reflection component of an ultrasound image that would have resulted had the anatomy represented in the sliced CT sector been probed with a transducer in B-mode. Equation 5.1 describes the log-compression step, for parameter a, where $I(\mathbf{x})$ is the value of a reflected intensity image at a point whose distance from the nearest point on simulated US probe face, $\mathbf{x}_0$, is $\lambda_{\mathbf{x}}$. The CT image, as mentioned, is μ, and the transmitting ray direction is $\mathbf{d}$.

$$r(\mathbf{x}) = \frac{\log(1 + aI(\mathbf{x}))}{\log(1 + a)} \tag{5.1}$$

$$I(\mathbf{x}) = I_0 \exp\left(- \int_0^{\lambda_{\mathbf{x}}} \left(\frac{|\nabla\mu(\mathbf{x_0} + \lambda\mathbf{d})|}{2\mu(\mathbf{x_0} + \lambda\mathbf{d})} \right)^2 d\lambda \right) \left(\mathbf{d}^T \nabla\mu(\mathbf{x})\right) \frac{|\nabla\mu(\mathbf{x})|}{2\mu(\mathbf{x})^2} \tag{5.2}$$

A great part of the intensity information present in a real ultrasound image derives from backscattered signals from small structures, not just large interface reflections, as has been assumed in other work. In addition to the log-compressed reflection component, the authors of [116] incorporated an additional intensity component, $p(\mathbf{x})$, derived, again, from the CT data, to represent this tissue-specific *echogeneity*. This derivation is based on the fitting of simple polynomials to plotted correspondences between X-ray attenuation coefficient, in CT and CTA, and ultrasound intensity, p, for a few pieces of anatomy, from a simple comparison of average typical image intensities.

To complete a particular B-mode slice simulation, a weighted sum of $r(\mathbf{x})$, $p(\mathbf{x})$ and an overall constant intensity level, γ, is formed,

$$f(\mathbf{x}) = \alpha p(\mathbf{x}) + \beta r(\mathbf{x}) + \gamma, \tag{5.3}$$

where p depends on CT intensity at the mapped position only, $p_i = p(\mu(\mathcal{T}(\mathbf{x})))$.

While exploitation of the proportionality between X-ray attenuation coefficient and acoustic impedance allows these impedances to be assigned on a voxel-wise basis, it is perhaps not clear that this fine a degree of impedance discrimination is *necessary* for good registration, especially since the images used in the experiments of [116] contain strong reflections from the diaphragm, whose relative contribution to intensity in the simulated images, may well have dwarfed that from much smaller features.

A different approach to ultrasound image simulation developed during the 1990s is implemented in the freely available *Field II* software of J. A. Jensen, [143, 81]. Linear-systems theory is used to calculate the raw radio frequency (RF) pressure field received by a given transducer by convolving its excitation function with impulse-response functions for its transmitting and receiving apertures, where the latter are calculated from the scattering structures to be imaged. The simplifying concept of impedance boundary reflections is not used, and all physical aspects of the ultrasound propagation are treated as the consequences of scattering in the time domain. On a 64-bit PC with four 2.33GHz processors and 8Gb of RAM, Field II takes around twenty minutes to produce an image simulation, given a typical number of input scatterers (10000), for which reason alone it is not suitable for use in the problem of registration for procedural guidance. However, in 2006, a newer linear-systems-based model of backscattered RF trace appeared in [144] which may perhaps, if implemented as a method of numerical image *simulation*, greatly outperform Field II in terms of computational speed, since it operates, instead, in the frequency domain. I am not aware of any such implementation to date, although the model has been applied to ultrasound image restoration and speckle removal, [145].

5.2 Methods

5.2.1 Ultrasound image simulation

The core component of the scheme outlined in Figure 5.1 is the simulation of ultrasound images, given spatial and anatomical information. As in [116], the technique for this is based on a model of diffuse reflection antiparallel to incident beam direction at interfaces between regions of differing acoustic impedance, Z, though, here, values for Z are explicity assigned to different regions (tissues) of the phantom (patient), rather than relying on the assumption of a simple relationship between anatomical image intensity and acoustic impedance. This is done by pre-operatively segmenting the anatomical image into a map of discrete tissues, and assigning a book value of acoustic impedance to each. As numerical phantom data were used in some of this work, the ground-truth geometry of the anatomical structure of interest was known here, but in the work involving real image data, delineation of the organ interfaces (segmentation) was necessary, and a source of error.

The fields-of-view (FOVs) for the simulated ultrasound images are shaped as truncated sectors, mimicking typical B-mode geometry. At each update of spatial parameters in the control loop shown in Figure 5.1, a new rigid transformation is defined to transform the pixel coordinates of a reference sector (see Figure 5.3) into the space of the 'anatomical' map of tissue regions (see Sections 5.2.2.2, 5.2.3.1), and this map is linearly interpolated at the transformed points to yield a sector of acoustic impedances, absorption coefficients and 'scatter' coefficients. The radial beam geometry of a curvilinear transducer is mimicked, as in [146], by warping the sectors into rectangles (see Section 5.2.2.2). Synthetic ultrasound beams are then propagated vertically down the columns of the rectangular image from the location of the artificial transducer head at the top, and the response of the anatomy to the numerical beams is modelled as a source component together with depth-dependent attenuation due to both reflections and absorption. Refraction is neglected for simplicity, with the same justification as was mentioned in [116].

First, the proportion of beam intensity which penetrates a boundary between regions with acoustic impedance Z_1 and Z_2 is modelled by

$$\Delta t(Z_1, Z_2) = 1 - \left(\frac{Z_2 - Z_1}{Z_2 + Z_1}\right)^2, \tag{5.4}$$

so that we may define a fractional transmission coefficient for each sector pixel location, $\mathbf{x}$, as

$$\Delta t(\mathbf{x}) = 1 - \left(\frac{Z(\mathbf{x} + \epsilon\mathbf{d}) - Z(\mathbf{x} - \epsilon\mathbf{d})}{Z(\mathbf{x} + \epsilon\mathbf{d}) + Z(\mathbf{x} - \epsilon\mathbf{d})}\right)^2, \tag{5.5}$$

where ϵ is a small constant and $\mathbf{d}$ is the unit vector pointing in the beam propagation direction.

By integrating equation 5.5, in the same manner as was used in [116] to derive equation 5.2, the proportion that *transmits* to the point $\mathbf{x}$ along a scanline originating from $\mathbf{x_0}$ can be modelled as

$$t(\mathbf{x}) = \exp\left(-\int_0^{\lambda_x} \left(\frac{|\nabla Z(\mathbf{x_0} + \lambda\mathbf{d})|}{2Z(\mathbf{x_0} + \lambda\mathbf{d})}\right)^2 d\lambda\right), \tag{5.6}$$

while an "image source" term is constructed, for each $\mathbf{x}$, as a weighted sum of a reflection term and a separate scatter term from that point (c.f. Eq. 5.32),

$$s(\mathbf{x}) = w_r r(\mathbf{x}) + (1 - w_r)\tilde{p}(\mathbf{x}). \tag{5.7}$$

Here, the reflection component is given by

$$r(\mathbf{x}) = \left(\mathbf{d}^T \nabla Z(\mathbf{x})\right) \frac{|\nabla Z(\mathbf{x})|}{2Z(\mathbf{x})^2}, \tag{5.8}$$

and $\tilde{p}(\mathbf{x})$ is related by a simple function—to be described in Section 5.2.2.1—to a pre-assigned parameter, $p(\mathbf{x})$, representing scattering strength, given at the anatomical location $\mathbf{x}$, with $0 \leq w_r \leq 1$.

The total absorption factor of the tissue between $\mathbf{x_0}$ and $\mathbf{x}$ is given by an expression similar to Eq. 5.6,

$$A(\mathbf{x}) = \exp\left(-(\ln 10)\int_0^{\lambda_x} 0.1\alpha(\lambda\mathbf{d})d\lambda\right), \tag{5.9}$$

where $\alpha(\mathbf{x})$ is the power absorption coefficient of the tissue at $\mathbf{x}$ in dBcm^{-1}.

The overall expression for received intensity, is, finally,

$$I(\mathbf{x}) = I_0\, A(\mathbf{x})^2\, t(\mathbf{x})^2\, s(\mathbf{x}), \tag{5.10}$$

where the squaring accounts for attenuation of the beam energy on both its outward and return journeys.

For my implementation in MATLAB, I have discretised Eqs 5.5, 5.8 and 5.6 to the following forms, for the n^{th} pixel along a scanline:

$$\Delta t(\mathbf{x}_n) = 1 - \left(\frac{Z(\mathbf{x}_n) - Z(\mathbf{x}_{n-1})}{Z(\mathbf{x}_n) + Z(\mathbf{x}_{n-1})}\right)^2, \tag{5.11}$$

$$r(\mathbf{x}_n, \theta) = \cos\theta \left(\frac{Z(\mathbf{x}_n) - Z(\mathbf{x}_{n-1})}{Z(\mathbf{x}_n) + Z(\mathbf{x}_{n-1})}\right)^2 \tag{5.12}$$

$$t(\mathbf{x}_n) = \prod_{k=1}^{n-1} \Delta t(\mathbf{x}_k) \tag{5.13}$$

Eqn 5.9 is discretised as

$$A(\mathbf{x}_n) = \prod_{k=1}^{n} e^{-0.1(\ln 10)\alpha(\mathbf{x}_k)|\mathbf{x}_k - \mathbf{x}_{k-1}|}, \tag{5.14}$$

where the distance $|\mathbf{x}_n - \mathbf{x}_{k-1}|$ is given in mm. The discrete version of 5.10 follows:

$$I(\mathbf{x}_n) = I_0\, A(\mathbf{x}_n)^2\, t(\mathbf{x}_n)^2\, s(\mathbf{x}_n), \tag{5.15}$$

More realistically however, the echoes returned from a beam sent by a single element will be received by an active *group* of elements, and the effect of this on the rectangular image can be modelled by applying a simple triangular horizontal line filter to the image ([146]). This was feature was implemented, but not, in fact, used in the experiments (i.e. the group size was set to 1 throughout), as the data used as surrogate ultrasound images did not involve the effect, and my aim was to keep the test environment as simple as possible.

Finally, the received intensities are log-compressed with parameter a,as given by Eq 5.16. This is done as the *final* step of the simulation, to mimic real B-mode image formation more closely, and to interact with the contributions of the parameters Z, α, p in a clearer way. It may be thought that performing a log-compression would only undo any attenuation that had already been simulated, but, in fact, the effect is to make intensities that decay exponentially (with depth, for instance) decay linearly instead.

$$S(\mathbf{x}) = \log(1 + aI(\mathbf{x}))/\log(1 + a). \tag{5.16}$$

Figure 5.1, below summarises the algorithm.

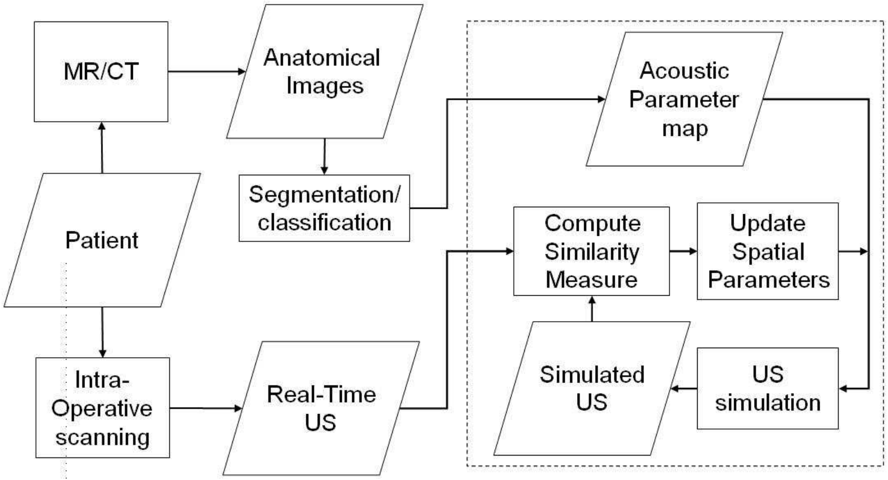

Figure 5.1: system block diagram

5.2.2 Data and geometry

5.2.2.1 Numerical phantom ‘anatomical’ data

These data were designed to represent a situation in which strong ultrasound-specific artefacts of edge reflection and acoustic shadowing were present, while the second was designed to test the technique where there were fewer artefacts, and neighbouring ‘anatomical’ structures were subtly — and for many applications, more realistically — distinguished from one another.

Using MATLAB, a highly simplified two-dimensional representation of human abdominal anatomy, P (see Figure 5.2(a)) was created, and from this, a representation of an anatomical image modality, X

Table 5.1: Acoustic parameters for strong-artefact phantom (M^1). Literature values of Z and α were used for: human liver parenchyma (A); bone, to represent 'calcifications' (B); kidney, to represent 'tumour' (C); skeletal muscle, to represent 'stomach' and 'pancreas' (D and E); fat (F). Echogenicity values are assigned arbitrarily.

'tissue'	$Z/10^6\mathrm{kgs}^{-1}\mathrm{m}^{-2}$	$\alpha/\mathrm{dBcm}^{-1}$	echogenicity/arb units
A	1.65	0.94	120
B	7.80	20.00	500
C	1.62	1.00	90
D	1.70	3.30	2000
E	1.70	3.30	2000
F	1.38	0.63	60

(see Fig. 5.2(b)) was derived by assigning new intensities arbitrarily to the six regions of P, which are labelled A-F in Figure 5.2(a).

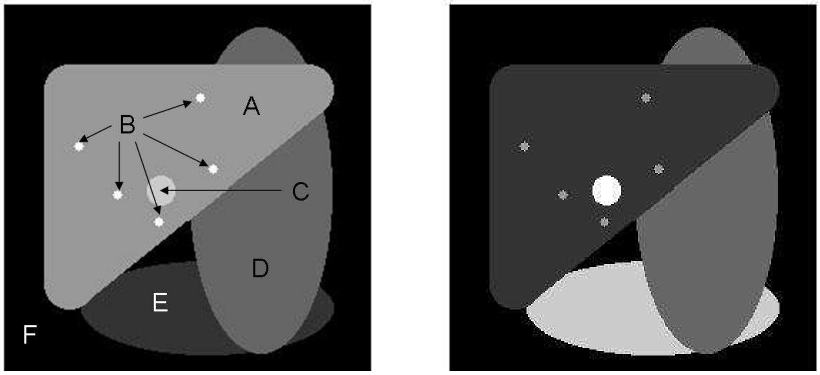

(a) P (b) X

Figure 5.2: Synthetic "patient", P and "anatomical image", X.

By assigning values to the three acoustic parameters mentioned in Section **??** in each of the six regions, two anatomical map images, denoted M^1 and M^2 were derived , as shown in Tables 5.1 and 5.2

5.2.2.2 Numerical phantom 'ultrasound' data and ground truth localisation

A smaller image, U which acts as a *surrogate* for a real B-mode ultrasound slice through the patient (P), was generated from each of M^1 and M^2 using an adapted version of *Field II*'s `cyst_phantom` example software ([147], [148]), together with components from my own simulation method presented in Section **??**. The pixel coordinates within the field-of-view of each of the two Us were defined with respect to the centre of a 2D reference slice, R after the polar-to-cartesian transformation of Eqs 5.18. Figure 5.3 depicts a binary image of R, showing the sector pixels, at coordinates in Ω_R, with respect to the image centre, in white.

Table 5.2: Acoustic parameters for subtle-artefact Phantom (M^2). Literature values of Z and α were used for: human liver parenchyma (A); blood, to represent vessels (B); kidney, to represent 'tumour' (C); skeletal muscle, to represent 'stomach' and 'pancreas' (D and E); fat (F). Echogenicity values are assigned arbitrarily.

'tissue'	$Z/10^6 \mathrm{kgs}^{-1}\mathrm{m}^{-2}$	$\alpha/\mathrm{dBcm}^{-1}$	echogenicity/arb units
A	1.65	0.94	500
B	1.61	0.18	10
C	1.62	1.00	90
D	1.70	3.30	26
E	1.70	3.30	35
F	1.38	0.63	2

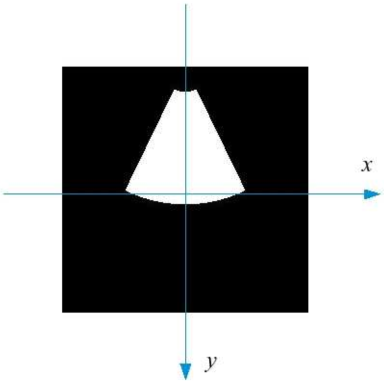

Figure 5.3: Reference sector, R, representing the shape of a B-mode US image obtained with a typical curvilinear array transducer used for abdominal imaging

$$\Omega_R^{\mathsf{POL}} = \left\{ (r,\theta) \in \mathbb{R}^2 : \left\{ \begin{array}{c} 25.8421\mathsf{mm} \leq r \leq 143.9671\mathsf{mm} \\ -32.7474^\circ \leq \theta \leq 32.7474^\circ \end{array} \right\} \right\}. \tag{5.17}$$

$$\Omega_R := \Omega_R^{\mathsf{CART}} \tag{5.18}$$

$$= \left\{ (x,y) : \left\{ \begin{array}{l} x = r\sin\theta \\ y = r\cos\theta - 128\mathsf{mm} \end{array} \right\}, (r,\theta) \in \Omega_R^{\mathsf{POL}} \right\} \tag{5.19}$$

The anatomical location of the FOV of U with respect to the centre of P was chosen by rigidly transforming the cartesian coordinates of points in Ω_R, the domain of R, into the appropriate locations as defined with respect to the coordinate system of X, with $\mathcal{T}^{\mathsf{GT}} : \Omega_R \rightarrow \Omega_X$. Parameters $\zeta^{\mathsf{GT}} = \{\theta^{\mathsf{GT}}, x^{\mathsf{GT}}, y^{\mathsf{GT}}\}$ defined the matrix representation, $\mathsf{T}(\zeta^{\mathsf{GT}})$, of this transformation as follows, for $(x_{\mathsf{ref}}, y_{\mathsf{ref}})^T \in \Omega_R$:

$$\begin{pmatrix} x \\ y \\ 1 \end{pmatrix} = \mathsf{T}(\zeta^{\mathsf{GT}}) \begin{pmatrix} x_{\mathsf{ref}} \\ y_{\mathsf{ref}} \\ 1 \end{pmatrix}, \tag{5.20}$$

where

$$\mathsf{T}(\zeta^{\mathsf{GT}}) = \begin{pmatrix} \cos(\theta^{\mathsf{GT}}) & -\sin(\theta^{\mathsf{GT}}) & 0 \\ \sin(\theta^{\mathsf{GT}}) & \cos(\theta^{\mathsf{GT}}) & 0 \\ 0 & 0 & 1 \end{pmatrix} \begin{pmatrix} 1 & 0 & x^{\mathsf{GT}} \\ 0 & 1 & y^{\mathsf{GT}} \\ 0 & 0 & 1 \end{pmatrix}.$$

Each of M_Z^i, M_α^i and M_p^i, having been assigned the same ‘anatomical’ coordinate system as P and X, were sampled at the mapped locations with linear interpolation, yielding ‘map sectors’. These were then warped ‘back’ into rectangles, essentially by inverting Eqs 5.18. *Field II* was then used to place 10000 scatterering sources within each sector and generate scatter images using the values of the p parameter at the scatterer locations as amplitudes. In some preliminary tests, the mean intensity of such a scatter image within a region of constant p was found to vary approximately linearly with the logarithm of p, and, by fitting a straight line to two regions appropriately spaced in intensity, the following relationship was estimated for mean speckle intensity, $\tilde{p}$

$$\tilde{p}(\mathbf{x}) \approx 40.9216 \log_{10}(p(\mathbf{x})) - 35.0834. \tag{5.21}$$

The surrogate ‘real’ ultrasound images U^1 and U^2 were completed by applying reflections, attenuations and log-compression to the respective outputs from *Field II*, in the same way as has been described for the simulated images in Sec. **??**. This was done by substituting these outputs for $\tilde{p}$ in Eq. 5.7. By visual inspection, the values: $a = 5000$, $w_r = 0.965$ were found to produce surrogate ultrasound images with a useful variety of features, shown in Figure 5.4.

5.2.2.3 3D ’anatomical’ data sets

The CT data for these experiments were obtained from the Harvard Abdominal CT Atlas, Fig. 5.5(a), while the MR data comprised a T1-weighted abdominal volume image from one volunteer, Fig 5.6(a). .

The space inside the body was segmented into bone, liver, blood, muscle, kidney and fat for both the CT and MR images, where all other tissues were labelled as fat. The atlas data provided this information for the CT image, whereas the MR segmentation was done using itk-SNAP. In the MR image, the inferior vena cava (IVC) and hepatic vasculature were segmented using a Hessian filter and surface renderings generated in Slicer (Fig. 5.6(a)). An affine pre-warping step was also applied to the MR image prior to use in registration, as explained in Sec. **??**.

Figure 5.4: Strongly and subtly artifactual U images. Circular 'calcifications' in 5.2.2.2 show strong surface reflection and shadowing; 'vessel' inclusions in 5.2.2.2 show weaker backscatter than the surrounding 'liver' parenchyma, but less reflection and shadowing.

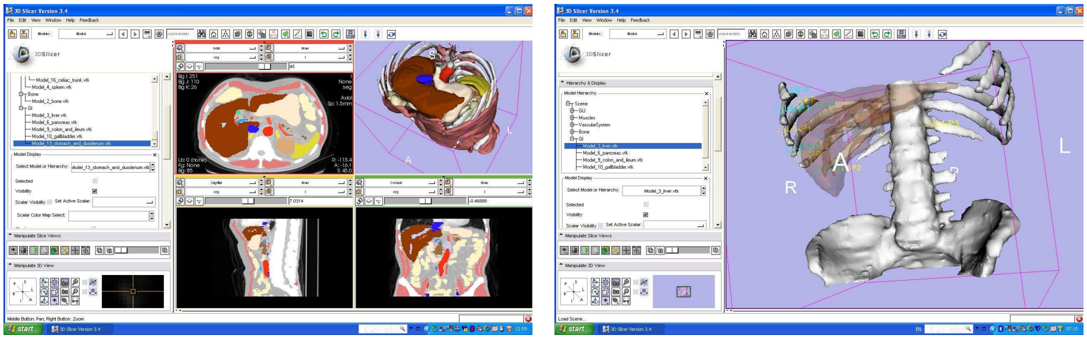

(a) atlas segmentation

(b) intercostal landmarks

Figure 5.5: 3D Slicer 3.2: Harvard abdominal CT Atlas

5.2.2.4 Intercostal US surrogate image data

Six synthetic US sector images were generated for intercostal FOV's within the Harvard CT Atlas using the technique of Sections 5.2.2.2 and **??** and the acoustic parameters given in Tab. 5.2.2.4. Each FOV was selected so as to include liver parenchyma and overlying tissues using a set of three points picked on the atlas using Slicer (Fig. 5.5(b)). For each set of three points, two points lay inside one of the intercostal spaces and one was located deeper within the liver. This third 'liver point' was the same for all sets. To obtain the i^{th} FOV, the Reference sector coordinates (Fig. 5.3) were mapped rigidly into the CT space with map $\mathcal{T}_i$ so that the two intercostal points of a set lay along the top edge of $\mathcal{T}_i(R)$, and the 'liver' point also lay in $\mathcal{T}_i(R)$. In this way, the whole collection of points defined a fan of mapped planes, $\{\mathcal{T}_i(R) : i = 1, 2, \ldots, 6\}$ radiating from the 'liver point' through six intercostal spaces. Within each plane, the white truncated sector region of $\mathcal{T}_i(R)$ defined the i^{th} FOV. The FOV's through segmented regions of the atlas were warped into rectangles by linearly interpolating their points' polar co-ordinates, (θ, r) onto rectangular grids. In this format, the anatomical FOV's were

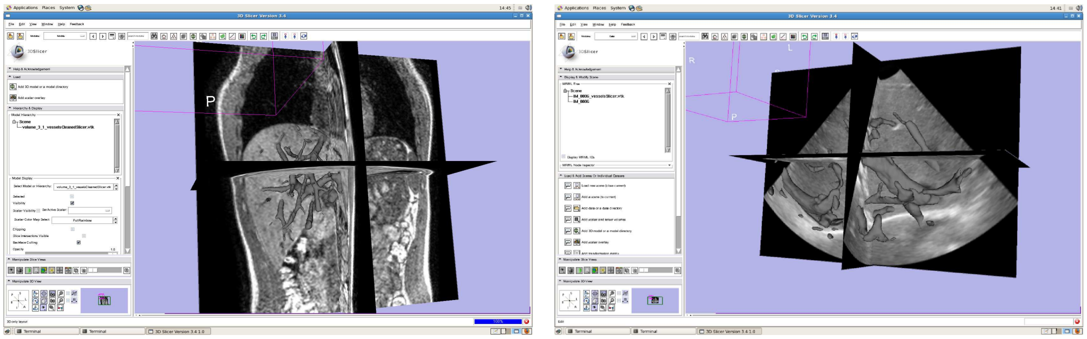

(a) MR (b) US

Figure 5.6: Slicer screenshots: corresponding MR and US volunteer images, with liver vessel renderings. The vessel surface renderings were obtained using a Hessian filtering technique.

tissue	$Z/10^6$kgs^{-1}m^{-2}	α/dBcm^{-1}	echogenicity/arb units
bone	7.80	20	1000
liver	1.65	0.94	500
blood	1.61	0.18	10
muscle	1.70	3.3	35
kidney	1.62	1.0	26
fat	1.38	0.63	2

Table 5.3: Acoustic Parameters for 3D Numerical Phantom

processed as described in Sec. 5.2.2.2,5.2.1 to produce synthetic US images $U_1, ..., U_6$.

Figure 5.7 shows these slices in the rectangular geometry in which they were also used during registration.

5.2.2.5 Sub-costal US surrogate image data

Ultrasound liver examinations are commonly performed via an acoustic window *underneath* the rib-cage, imaging in a superior-posterior direction. I produced a second set of nine surrogate US images in this orientation — referred to here as "sub-costal" images. To avoid inverse crime as far as possible, these were generated using characteristics of real images alone, bypassing any of the modelling used for the simulated "S" images, as follows. The process is illustrated by Fig. 5.8(a) and one of the images by Fig. 5.8(b).

i. warp a real B-mode US liver image sector to a rectangle

ii. segment the liver region

iii. fit a quartic polynomial surface to the points within the liver region

iv. normalise (divide) the liver region intensities by the fitted polynomial values

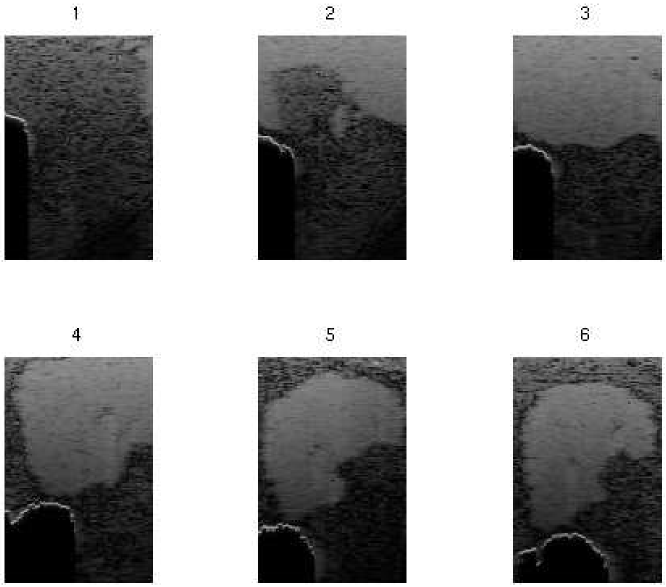

Figure 5.7: $U_1, ..., U_6$, warped into rectangles. The images were generated from slices through the Harvard CT Atlas segmentations with the geometry of Fig. 5.3, which were warped by interpolating polar co-ordinates onto a cartesian grid using Eq. 5.18

v. choose a representative patch of normalised liver texture and use it to synthesize a larger texture image

vi. repeat steps 2-5 for kidney

vii. sample a 1D vertical profile across the diaphragm in the warped US image

viii. sample FOV's through the CT segmentation similarly to Sec. 5.2.2.4, using a reference sector, r measured from a real US image (rather than Fig. 5.3)

ix. apply the texture images to the relevant parts of the FOV's

x. convolve the diaphragm profile with a one-pixel-thick binary image of the liver/lung border in each FOV

The fitting function was a fourth-degree polynomial in the lateral (angular) co-ordinate and an eighth-degree polynomial in the axial (radial) co-ordinate. This was chosen as the lowest degree polynomial that appeared to capture the large-scale intensity variation across the liver, and for its lateral symmetry (even degree). Its coefficients were found by a linear least squares fit.

Most liver FOV's looking under the ribcage intersected a loop of colon, since the atlas remained undeformed when selecting FOV's, whereas a patient's abdominal skin, fat and muscle would have deformed under probe pressure in a real examination. This would be problematic for any US simulation, owing to the very low impedance of bowel gas, but since it usually does not happen in suitable acquisitions with live subjects, I gave the tissue parameters of fat to the colon, effectively ignoring it.

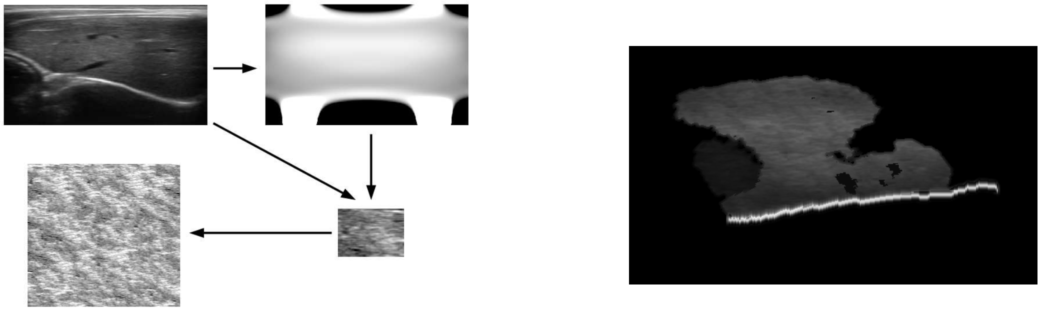

(a) process

(b) representative slice

Figure 5.8: Surrogate generation through texture/intensity synthesis. A volunteer US liver image was warped to a rectangle by linear interpolation (5.8(a) top left), a polynomial function of cartesian coordinates was fitted to the segmented liver parenchyma (5.8(a) top right), and used to normalise the image. A sample of liver parenchyma texture was taken from the normalised parenchyma (5.8(a) bottom right), and used to synthesize a larger patch (5.8(a) bottom left). Completed synthetic subcostal image, 5.8(b).

5.2.2.6 Volunteer US image data

The abdomen of a volunteer was scanned beneath the right-hand ribcage using a Philips X3-1 2D xMATRIX phased array probe. The liver and kidney were segmented in itk-SNAP and all major vasculature were segmented and surface-triangulated as for the MR, as shown in Fig. 5.6(b). No attempt was made to synchronise the breathing phase between the MR and US acquisitions, which occurred on different days. I extracted nine equally-spaced 2D sector images from the reconstructed volume for use in registration.

I determined a ground-truth global affine transformation (12 degrees-of-freedom (dof)) between the nine US slices and corresponding MR volume corresponding anatomical landmarks using the following procedure.

i. Choose five corresponding vessel bifurcations from the two renderings (Fig. 5.9)

ii. Choose a larger set of points from corresponding *lines* in the vessel renderings (Fig. 5.10), and add to the five landmark points

iii. Use the Procrustes algorithm ([149, 97])to estimate the best rigid-plus-scaling (7 dof) transformation between the US bifurcation points onto the MR bifurcation points

iv. Use the Iterative Closest Point algorithm (ICP) to estimate the best rigid plus 3 scalings plus 3 shears (12 dof) transformation from

   - the US bifurcation and vessel line points, *after* applying the result of step 2

- the MR bifurcation and vessel line points

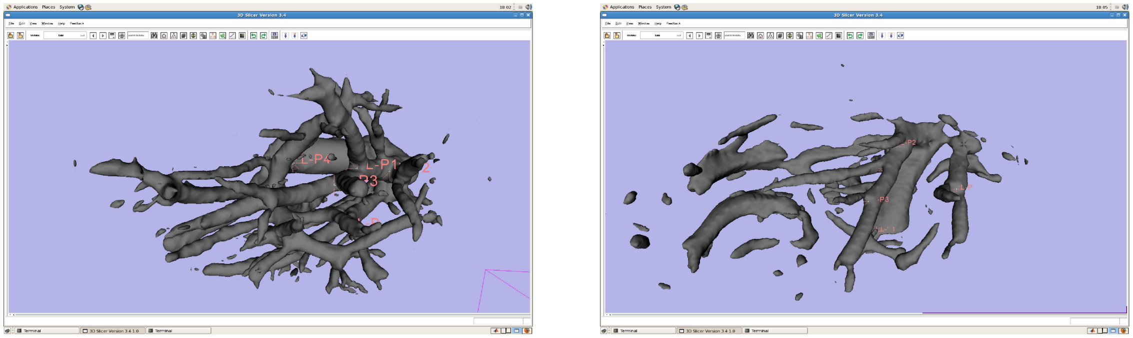

(a) MR (b) US

Figure 5.9: Slicer screenshots: corresponding vessel bifurcation points

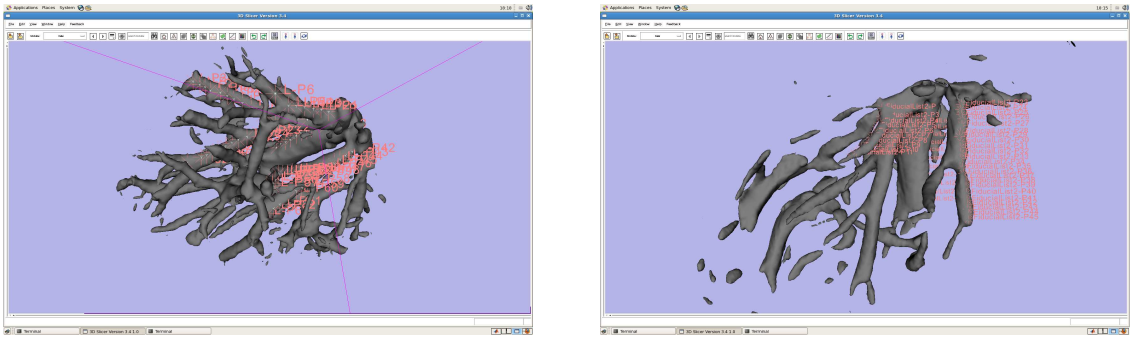

(a) MR (b) US

Figure 5.10: Slicer screenshots: points chosen on corresponding vessel lines

The transformation obtained was applied to the voxel co-ordinates of nine US slices, and the MR volume was sampled at the transformed points, producing the alignment shown in Fig. 5.11

The misregistration of the diaphragm visible in Fig. 5.11 was corrected by incorporating the liver surface into the alignment. A number of points were chosen over regions of liver surface beneath the diaphragm that approximately corresponded after the images were aligned as above (Fig. 5.12). Fig. 5.13 shows the ground-truth alignment obtained when these diaphragm points are amalgamated with the bifurcation and vessel line points for the ICP stage of the procedure.

To focus on comparing the behaviour of the different registration criteria, I artificially simplified the registration task so as to seek a rigid transformation, by pre-deforming the MR volume. If steps 3 and 4 above yield transformation matrices $\mathsf{T}_{\mathsf{rig}}$ and $\mathsf{T}_{\mathsf{aff}}$, we may indicate the anatomical correspondence by writing, for any spatial location with co-ordinates $\mathbf{x}$ in the US image frame,

$$MR(\mathsf{T}_{\mathsf{aff}}\mathsf{T}_{\mathsf{rig}}\mathbf{x}) \sim US(\mathbf{x}). \tag{5.22}$$

Then the deformed image, defined by $\widetilde{\mathsf{MR}}(\mathbf{y}) \equiv MR(\mathsf{T}_{\mathsf{aff}}\mathbf{y})$, Fig. 5.14 registers rigidly to the US, since

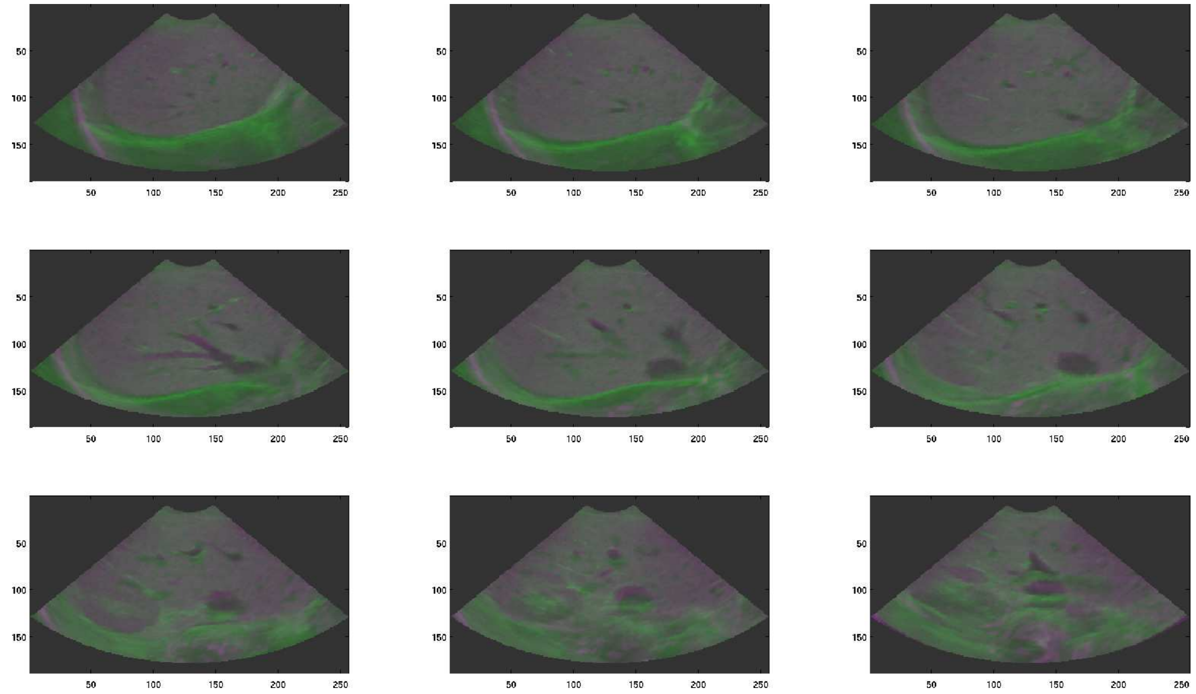

Figure 5.11: 12 degree-of-freedom affine alignment (ground-truth) based vessel points and lines

$$\begin{aligned}\widetilde{\mathsf{MR}}(\mathsf{T}_{\mathsf{rig}}\mathbf{x}) &= \mathsf{MR}(\mathsf{T}_{\mathsf{aff}}\mathsf{T}_{\mathsf{rig}}\mathbf{x})\\ &\sim \mathsf{US}(\mathbf{x}).\end{aligned}$$

5.2.2.7 Rigid transformation geometry

The spatial relationships, true and estimated, between the sets of US slices detailed above and the relevant anatomical co-ordinate systems, are described as follows.

The coordinates of the ith FOV in the atlas space are found by applying transformation $\mathcal{T}_i$ to the coordinates of R. In order to determine six rigid transformation parameters for a *set* of FOVs, the matrix of *one of* the $\mathcal{T}_i$ (I used no. 4 for one set) is decomposed as

$$\mathsf{T}_4 \equiv \mathsf{T}(\zeta^{\mathsf{GT}}) = \mathsf{R}_z^{\mathsf{GT}}\,\mathsf{R}_x^{\mathsf{GT}}\,\mathsf{R}_y^{\mathsf{GT}}\,\Delta^{\mathsf{GT}}, \tag{5.23}$$

where

$$\mathsf{R}_z^{\mathsf{GT}} = \begin{pmatrix} \cos(\theta_z^{\mathsf{GT}}) & -\sin(\theta_z^{\mathsf{GT}}) & 0 & 0\\ \sin(\theta_z^{\mathsf{GT}}) & \cos(\theta_z^{\mathsf{GT}}) & 0 & 0\\ 0 & 0 & 1 & 0\\ 0 & 0 & 0 & 1 \end{pmatrix}, \qquad \mathsf{R}_x^{\mathsf{GT}} = \begin{pmatrix} 1 & 0 & 0 & 0\\ 0 & \cos(\theta_x^{\mathsf{GT}}) & -\sin(\theta_x^{\mathsf{GT}}) & 0\\ 0 & \sin(\theta_x^{\mathsf{GT}}) & \cos(\theta_x^{\mathsf{GT}}) & 0\\ 0 & 0 & 0 & 1 \end{pmatrix}, \tag{5.24}$$

$$\mathsf{R}_y^{\mathsf{GT}} = \begin{pmatrix} \cos(\theta_y^{\mathsf{GT}}) & 0 & \sin(\theta_y^{\mathsf{GT}}) & 0\\ 0 & 1 & 0 & 0\\ -\sin(\theta_y^{\mathsf{GT}}) & 0 & \cos(\theta_y^{\mathsf{GT}}) & 0\\ 0 & 0 & 0 & 1 \end{pmatrix}, \qquad \Delta^{\mathsf{GT}} = \begin{pmatrix} 1 & 0 & 0 & x^{\mathsf{GT}}\\ 0 & 1 & 0 & y^{\mathsf{GT}}\\ 0 & 0 & 1 & z^{\mathsf{GT}}\\ 0 & 0 & 0 & 1 \end{pmatrix}. \tag{5.25}$$

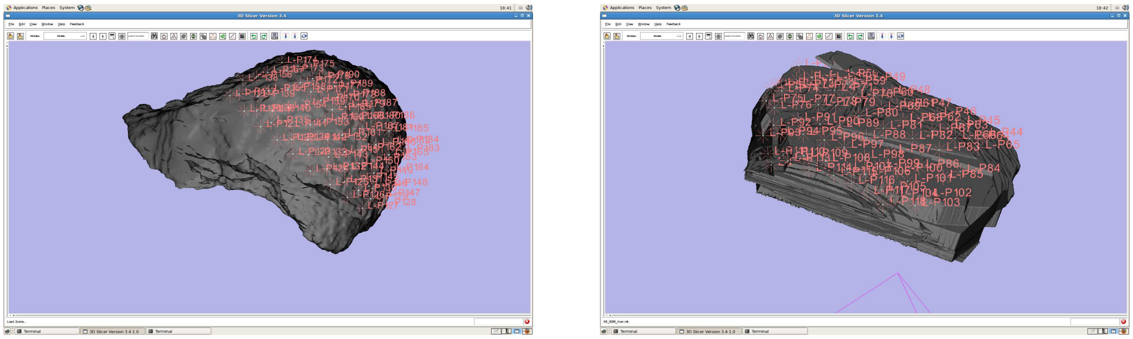

(a) MR (b) US

Figure 5.12: Slicer screenshots: points chosen over a corresponding liver surface region on surface renderings derived from the MR image volume (5.12(a)) and the US image volume (5.12(b)).

Values for the parameters $\zeta^{\mathsf{GT}} = \{\theta_z^{\mathsf{GT}}, \theta_x^{\mathsf{GT}}, \theta_y^{\mathsf{GT}}, x^{\mathsf{GT}}, y^{\mathsf{GT}}, z^{\mathsf{GT}}\}$ were then found. Since these are not uniquely defined, they were given the values of smallest modulus from possible combinations found by solving a system of simultaneous equations. The rigid relations between the different sectors themselves were found by simply computing, for each, an additional 4×4 "tracking" matrix, denoted T_i^{TC}.

$$\mathsf{T}_i^{TC} = (\mathsf{T}(\zeta^{\mathsf{GT}}))^{-1}\mathsf{T}_i,$$

so that the anatomical points corresponding to the pixels of *all slices* in an US set, considered as a stack of sectors, may be given by the one-to-many mapping

$$\mathcal{T}^{\mathsf{GT}}(\Omega_R),$$

where $\mathcal{T}^{\mathsf{GT}}$ has a matrix representation given by the following (for a six-sector stack),

$$\begin{pmatrix} \mathsf{T}^{\mathsf{GT}} & \dots & \dots & 0 \\ \vdots & \mathsf{T}^{\mathsf{GT}} & \dots & \vdots \\ \vdots & \vdots & \ddots & \vdots \\ 0 & \dots & \dots & \mathsf{T}^{\mathsf{GT}} \end{pmatrix} \begin{pmatrix} \mathsf{T}_1^{TC} \\ \mathsf{T}_2^{TC} \\ \vdots \\ \mathsf{T}_6^{TC} \end{pmatrix}, \tag{5.26}$$

and acts on coordinate *column* vectors $\mathbf{x}_i$ of the N points in Ω_R. The aim of rigid registration is then to automatically recover ζ^{GT} from some initial (different) set of values. Under the current set-up, T^{TC} is the 4×4 identity matrix.

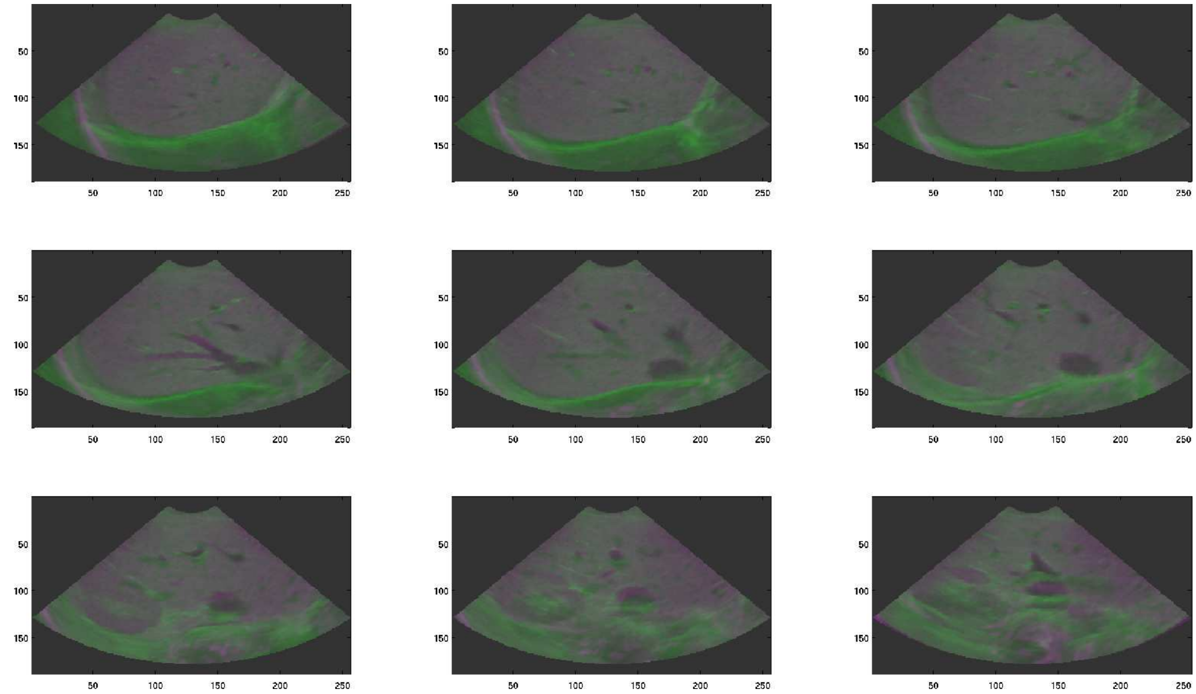

Figure 5.13: 12 degree-of-freedom affine alignment (ground-truth) based on vessel points/lines, and diaphragm points

5.2.3 Features and similarity measures

5.2.3.1 For use with 2D numerical phantom images

In general, for any choice of $\zeta = \{\theta, x, y\}$, a matrix may be assembled represent a rigid transformation, $\mathcal{T}^{\zeta}$, analogously with Equation 5.20, mapping the pixel coordinates of the reference sector to those of an anatomical sector. For each of the two experiments ('strongly artefactual' and 'subtly artefactual'), I sought to recover the transformation mapping U^i into anatomical space automatically, by optimising an initial choice, ζ^0, towards ζ^{GS}. Two different registrations were performed for each experiment, which may be called 'simulation based' and 'direct'. In the simulation-based procedure, an artificial ultrasound image, S^{ζ} was simulated at each ζ as in 5.2.1, and a similarity measure computed between S^{ζ} and U. Registration of U into anatomical space was then achieved by finding

$$\tilde{\zeta} = \underset{\zeta}{\mathrm{argmax}}\,\mathsf{sim}(U, S^{\zeta}).$$

So as to represent a situation where the acoustic parameters of tissue are accurately known in the model, the values of impedance and absorption were taken from the same maps, M^i_Z and $M^i_{\alpha}, i = 1, 2$, as were used to generate U, and the scatter term of Eq. 5.7, $\tilde{p}(\mathbf{x})$ is given by Eq. 5.21. Figure 5.15 shows the simulations, for each experiment, at $\zeta = \zeta^{\mathsf{GS}}$.

Squared normalised cross-correlation (NCC^2) was used as the similarity measure:

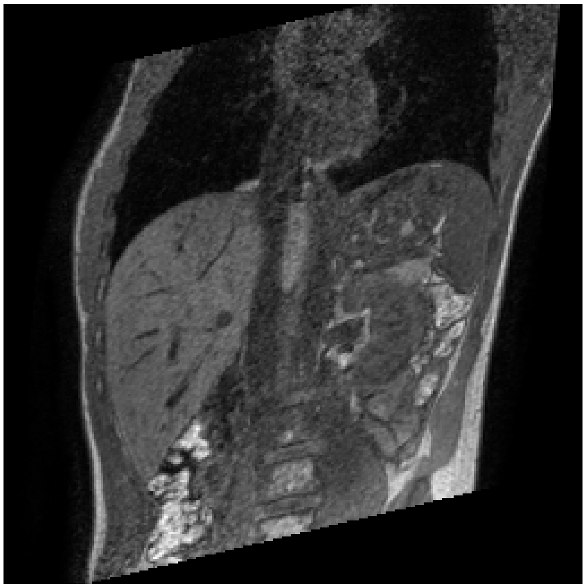

Figure 5.14: Coronal section through $\widetilde{\mathsf{MR}}$

$$\mathsf{NCC}^2_{U,S}(\zeta) = \frac{\left(\sum\limits_{\mathbf{x}\in\Omega_R} \left(U(\mathbf{x}) - \bar{U}\right)\left(S^{\zeta}(\mathbf{x}) - \bar{S}^{\zeta})\right)\right)^2}{\sum\limits_{\mathbf{x}\in\Omega_R} \left(U(\mathbf{x}) - \bar{U}\right)^2 \sum\limits_{\mathbf{x}\in\Omega_R} \left(S^{\zeta}(\mathbf{x}) - \bar{S}^{\zeta}\right)^2}. \tag{5.27}$$

At each iteration of the ‘direct’ registration, a sector region was sampled from X itself, at locations given, again, by $\mathcal{T} : \Omega_R \rightarrow \Omega_X$, and similarity computed between this sample and U. Normalised mutual information (NMI) is a similarity measure well suited to registration of images with widely different intensity characteristics ([100], [103]), and was used for this direct comparison (Equation 5.28), as well as normalised cross-correlation (Equation 5.29). Twenty-two bins were used for the joint histograms, which was judged to be a sensible number in early tests. Figures 5.16 and 5.17 show plots of these measures as cost functions after blurring the two images, in each case, with a Gaussian filter. Denoting $X(\mathcal{T}^{\zeta}(\Omega_R))$ by X^{ζ},

$$\mathsf{NMI}_{U,X}(\zeta) = \frac{H(U) + H(X^{\zeta})}{H(U, X^{\zeta})} \tag{5.28}$$

Figure 5.15: Strongly and subtly artifactual $S^{\zeta^{\text{GS}}}$. Simulated US images generated for the ground-truth FOV's corresponding to Fig. 5.4.

$$\text{NCC}^2_{U,X}(\zeta) = \frac{\left(\sum_{\mathbf{x}\in\Omega_R} \left(U(\mathbf{x}) - \bar{U}\right)\left(X^{\zeta}(\mathbf{x}) - \bar{X^{\zeta}}\right)\right)^2}{\sum_{\mathbf{x}\in\Omega_R} \left(U(\mathbf{x}) - \bar{U}\right)^2 \sum_{\mathbf{x}\in\Omega_R} \left(X^{\zeta}(\mathbf{x}) - \bar{X^{\zeta}}\right)^2}. \tag{5.29}$$

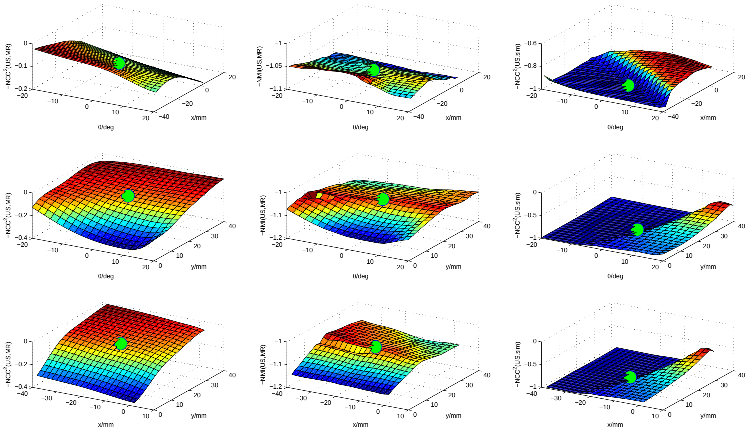

Figure 5.16: Cost function landscapes for strong-artefact data with $\sigma = 3$ blurring: $-\text{NCC}^2_{U,X}$ (left), $-\text{NMI}_{U,X}$ (middle), $-\text{NCC}^2_{U,S}$ (right). The green spheres show GS alignment.

5.2.3.2 For use with 3-D images

Normalised Mutual Information

The Normalised Mutual Information (NMI) between images U and X, considered as random variables is

$$\text{NMI}(U, X) = \frac{H(U) + H(X)}{H(U, X)}, \tag{5.30}$$

where the entropies and joint entropy are

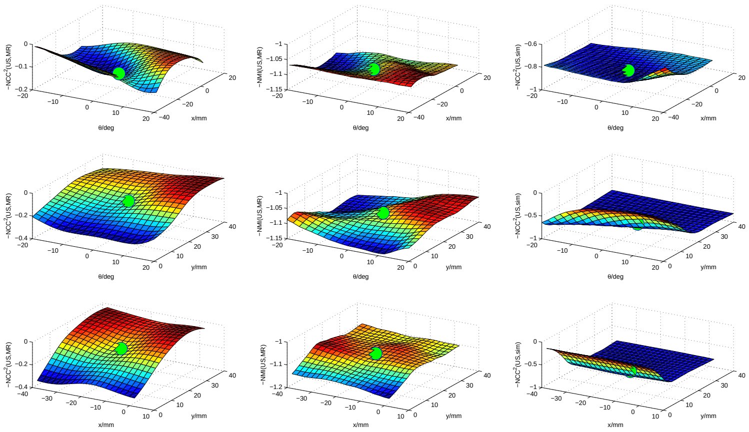

Figure 5.17: Cost function landscapes for subtle-artefact data with $\sigma = 3$ blurring: $-\text{NCC}^2_{U,X}$ (left), $-\text{NMI}_{U,X}$ (middle), $-\text{NCC}^2_{U,S}$ (right). The green spheres show GS alignment.

$$H(U) = \sum_k p(U = k) \log \left(\frac{1}{p(U = k)} \right), H(X) = \sum_l p(X = l) \log \left(\frac{1}{p(X = l)} \right)$$

$$H(U, X) = \sum_{k,l} p(U = k, X = l) \log \left(\frac{1}{p(U = k \wedge X = l)} \right).$$

In the current work, the name U_X_NMI denotes -NMI between an ultrasound and a CT or MR image. Probabilities are estimated with 256-bin histograms.

Ultrasound Simulation Correlation

Criterion U_S_NCC2 has already been described. I use the abbreviation U_S_LC2 to denote the similarity criterion published by Wein et al. [116], closely re-implemented here in MATLAB.

$$\text{U\_S\_LC2}(\zeta) = 1 - \frac{\sum_{\mathbf{x} \in \Omega} (U(\mathbf{x}) - f(\mu(\mathcal{T}^{\zeta}(\mathbf{x}))))^2}{|\Omega| Var(U)}. \tag{5.31}$$

In Eq. 5.31, U denotes an ultrasound image, and $f(\mathcal{T}(\mu))$ an ultrasound image *simulation* generated in real time from a particular FOV through a 3D map of CT Hounsfield number, μ. Simulation f is a linear combination of reflection, r, echogenicity, p and constant components. The integral in Eq. 5.2 represents the cumulative reduction of reflected (I) vs. transmitted (I_0) wave intensity from depth $\mathbf{x}$. The well-known formula for reflected wave intensity at an interface between regions of different acoustic impedance has been used, with μ serving as a surrogate for impedance, and the CT volume as a continuum of such interfaces. Eq. 5.1 models the logarithmic dynamic range compression performed by B-mode ultrasound machines for some constant a.

$$f(x_i) = \alpha p_i + \beta r_i + \gamma, \tag{5.32}$$

where r is as given by Eq. 5.1.

The echogenicity p-parameter was derived from CT intensity by the same mapping as in [116].The abbreviation U_S_LC2twh denotes the tissue-wise homogeneous version, presented in Sec. 5.2.1. This version used the tissue parameter values given in Tab. 5.2.2.4.

Vessel Probability

Pr_Pr_NCCsoft denotes a re-implementation of the vessel probability method of Penney et al. [114], which I used with the MR data. A vessel probability look-up table was generated for the MR volume according to

$$p_{\mathsf{MR}}(I) = \frac{\text{no.vesselvoxelswithintensity}I}{\text{no.livervoxelswithintensity}I} \tag{5.33}$$

and a similar p_{US} table made for the US image after processing to a ‘dip image’ and a mask was generated to confine computation of the measure to the region above the diaphragm and below the top 3cm of the US sectors, as detailed in [114]. The criterion computes the NCC between vessel probability *maps*, V_{MR}, V_{US} made by applying the look-up tables back to the MR and US dip images. Denoting $V_{\mathsf{MR}}(\mathcal{T}^{\zeta}(\Omega_R))$ as V_{MR}^{ζ},

$$\text{Pr\_Pr\_NCC}(\zeta) = \frac{\left(\sum\limits_{\mathbf{x}\in\Omega_R} \left(V_{\mathsf{US}}(\mathbf{x}) - \bar{V}_{\mathsf{US}}\right)\left(V_{\mathsf{MR}}^{\zeta}((\mathbf{x})) - \bar{V}_{\mathsf{MR}}^{\zeta}\right)\right)^2}{\sum\limits_{\mathbf{x}\in\Omega_R} \left(V_{\mathsf{US}}(\mathbf{x}) - \bar{V}_{\mathsf{US}}\right)^2 \sum\limits_{\mathbf{x}\in\Omega_R} \left(V_{\mathsf{MR}}^{\zeta}((\mathbf{x}))) - \bar{V}_{\mathsf{MR}}^{\zeta}\right)^2}. \tag{5.34}$$

In a ”‘hard”’ version for use with CT, Pr_Pr_NCChard, V_{MR} is replaced with a binary vessel segmentation, since CT vessel contrast is too weak to give a useful V_{CT} map.

Local Phase/Orientation Mutual Information

Since, to my knowledge, results for the local phase mutual information criterion of [109, 110] have not been published for use with real ultrasound, I have included it in the comparison using volunteer US and MR data. With $\phi(X)$ denoting the *local phase* of an MR or CT image X, and $X(\mathcal{T}^{\zeta}(\Omega_R))$ denoted X^{ζ},

$$\text{Ph\_Ph\_MI}(\zeta) = -\text{NMI}\left(\phi(U), \phi(X^{\zeta})\right). \tag{5.35}$$

In early tests with these I found that Grau and Noble's phase/orientation measure [113], given by Eq. 2.12 suffered from many local minima, so a modified version (Eq. 5.36), for static images, intended to be less sensitive to inter-modal differences, is included instead, where $o(X)$ the *local orientation* of X,

$$\mathsf{Phor\_Phor}(\zeta) = -\mu\mathsf{NMI}\left(\phi(U), \phi(X^{\zeta})\right) + \sum_{r} \frac{W(r)\left(1 - \left(o(U(r)).o(X^{\zeta}(r))\right)^{2}\right)}{\sum_{r} W(r)}. \tag{5.36}$$

The NMI term allows images whose phases don't correlate simply to be considered similar, while the squared orientation dot product allows, crudely speaking, both "parallel" and "antiparallel" features to be matched.

5.2.3.3 Non-overlap penalty

To help deter the optimisation procedure from rigid parameter vectors far from the solution, A non-overlap penalty term $\frac{|\mathcal{T}^{\zeta}(\Omega_R)|}{|\Omega_R|}$ was added to the above cost functions for some of the experiments. Figures 5.18 and 5.19 show its effect on the U_S_NCC2 criterion at the three different levels of the filtering scheme used for registration.

5.2.4 Initialisation and recovery of alignment (3-D data)

For the intercostal surrogate images I performed fifty registration trials with rigid parameters initialised (uniformly) randomly within $\zeta^{GS} \pm (10\mathrm{mm}, 10\mathrm{mm}, 10\mathrm{mm}, 10°, 10°, 10°)^{\mathrm{T}}$. The ribcage was "removed" from the atlas during registration, in a similar manner to the colon for the subcostal image. The justification for this step is given in Sec. 5.2 of [150]. Each cost function was minimised using the steepest descent method, after addition of the non-overlap penalty term. At each similarity computation step, the 2D sector images (reference and sampled template) are warped into rectangles. Since the warping was done by linear interpolation, no new voxel intensities were introduced. For the volunteer data I performed 250 registration trials initialised using the same method.

5.3 Results

5.3.1 Intercostal US surrogates and CT

Registration results are given for the surrogates generated from *Field II* with additional attenuation and reflection in Tab. 5.4 and Fig. 5.20. The column heading NMI(U,X) denotes trials in which the surrogates were registered to the original, 54-compartment Harvard CT segmentation. Target registration errors (TRE's) were all measured over a 30mm-radius spherical region-of-interest chosen within the liver to represent a tumour.

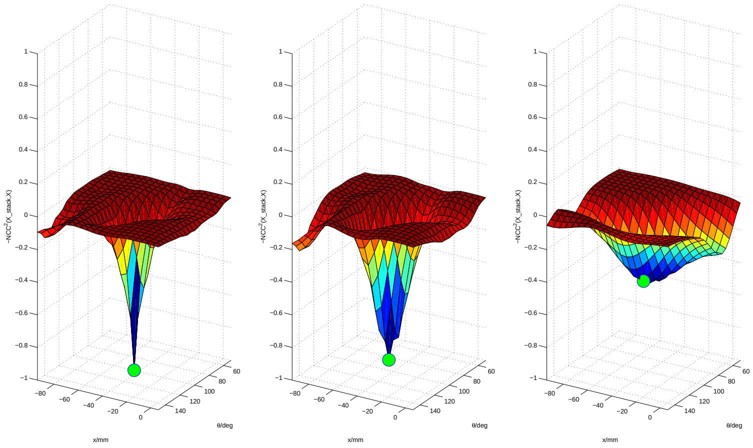

Figure 5.18: Landscape plots of -NCC^2(U,S): Gaussian blur with $\sigma = 0, 3, 15$ and no penalty term

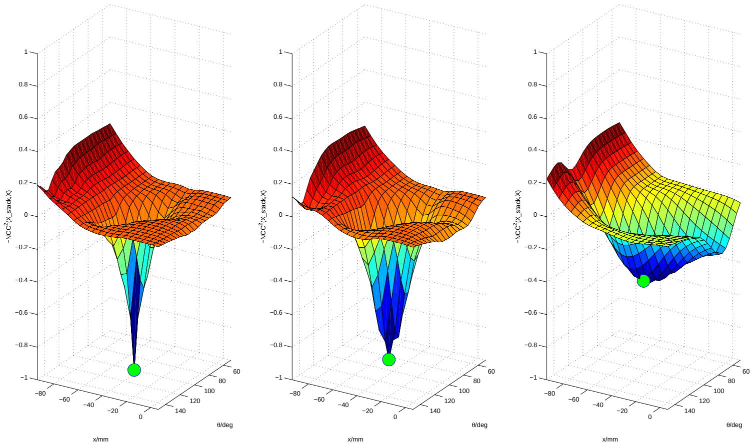

Figure 5.19: Landscape plots of -NCC^2(U,S): Gaussian blur with $\sigma = 0, 3, 15$, and penalty term

		NMI	NMI	NCC^2
	Initial	(U, X)	(U, CT)	(U, S)
mean TRE/mm	10.1	14.8	57.5	7.2
5^{th} pctile. TRE/mm	4.1	0.7	6.2	1.0
median TRE/mm	10.4	3.8	67.1	4.8
95^{th} pctile. TRE/mm	17.6	68.9	96.0	18.7
% successful	-	54	0	54
capture range/mm	-	2.0	n/a	2.0
mean total time/sec	-	44	34	87

Table 5.4: Intercostal surrogates: summary statistics

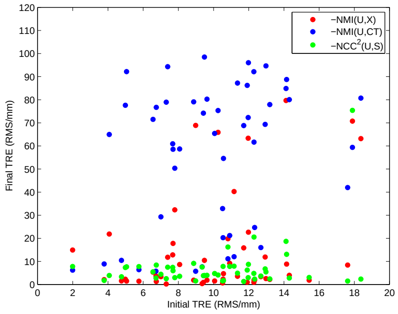

Figure 5.20: final vs. initial TRE's

	U_X_NMI	U_S_LC2	Phor_Phor	Pr_Pr_NCChard
acc./mm	4.4	9.5	6.1	14.8
prec./mm	25.6	7.6	8.1	20.3
% successful	74	90	86	76
cap. radius/mm	25.5	26.6	20.6	32.4
mean total time/sec	432	1035	1415	329

Table 5.5: Subcostal surrogates: summary statistics

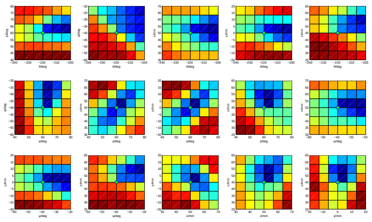

Figure 5.21: U_S_LC2 plots at coarse level

5.3.2 Subcostal US surrogates and CT

Registration results for the sub-costal images are shown in Tab. 5.5. TRE's are computed over the same ROI as for the intercostal slices.

5.3.3 Volunteer US and MR

For the volunteer data, I again chose an ROI within the liver. TRE's in Tab. 5.3.3 are quoted over ROI/whole liver.

	Pr_Pr_NCCsoft	U_S_LC2twh	Ph_Ph_MI
acc./mm	2.2/1.5	3.9/7.4	16.2/42.6
prec./mm	1.0/1.4	3.1/4.9	50.7/82.8
% successful	99/99	48/44	46/65
capture radius/mm	8.3/10.0	7.4/13.3	12.5/13.4

Table 5.6: Summary Statistics: volunteer US-to-MR registration computed over ROI/liver

5.4 Discussion

5.4.1 Intercostal US surrogates and CT

The results show that the simulation-based method performs more consistently and accurately in-the-average than the direct method. The fact that the direct method sometimes performs remarkably well, when it does succeed, is of some interest, though its lack of consistency would certainly make it unsuitable for clinical use. These successes occur in the U-to-X trials, and not the U-to-CT trials, indicating that NMI is finding a weak minimum as GS alignment, when the anatomical image consists of *discrete tissue compartments*, even though these are more finely partitioned than in the model used to generate the surrogate ultrasound, U. The simulation provides some overall benefit, but this is much less clear than in Section **??**.

5.4.2 Subcostal US surrogates and CT

The most surprising result here is how well NMI performed, especially when compared with the simulation-based method. Additional landscape plots for U_S_LC2 at the coarse and medium pyramid levels show that global minima generally lie at or near the ground truth locations, however, there is a strong drop-off with increasing θ and ϕ - see Fig. 5.21. The simulated images contain an increasing proportion of highly echogenic muscle and fat toward this region, which probably leads to the poor registration.

5.4.3 Volunteer US and MR

The vessel probability method has worked remarkably well despite the poor performance of the "hard" version reported on in Sec. 5.3.2. That the ground-truth alignment has also been determined from the vessels may well account for the very low accuracy and precision figures here, but the robustness figures are also good. Perhaps this is due to the simple nature of this criterion - as much of the "work" it does is done before registration commences, to generate two like feature representations, p_{US} and p_{MR}, the actual similarity *measure* can be one that makes few assumptions, NCC^2, so that local minima will only appear by " coincidence" (assuming good p_{US} and p_{MR}). This is in contrast to U_X_NMI above: a sometimes-over-accommodating similarity measure acting on raw and complicated feature representations. Precisions are less than accuracies for the two criteria which worked better (much less for U_S_LC2) suggesting a possible local minimum or ground truth error. Local phase MI has done badly, perhaps predictably, from the lack of applications of this criterion to US-MR in the literature.

5.5 Conclusions

A framework has been put in place for evaluating different US-MR and US-CT registration criteria. The tesults obtained indicate that vessel probability is the strongest method overall for US-CT, and that simulation correlation or local phase/orientation is the strongest for US-MR. However it is not clear that the vessel probability criterion wasn't unfairly advantaged by the origin of the ground truth alignment. Ideally, this alignment would be found by identifying anatomical landmarks independently of the vasculature, but vessels-based landmarks are by far the easiest to identify. Perhaps a more serious problem with my implementation of Pr_Pr_NCC2 is that p_{MR} and p_{US} were derived from the images for which they were then used. With further data sets this can be corrected with a leave-one-out scheme. Similar though not so serious, concerns apply to the CT no. - echogenicity mapping for U_S_LC2.

Chapter 6

Conclusions

6.1 Summary of findings

Recovery of densities and bulk moduli from compartments of a piecewise homogeneous medium is possible in principle with limited-angle reflected ultrasound, given knowledge of the compartment locations up to at least a spatial translation. Vessel probability appears to be a feature with which to register anatomical compartments robustly and accurately from an MR image into physical space using B-mode ultrasound. The best image-based method to register them from a CT image appears to be to one which “extracts” ultrasound-like features from the CT via a simulation.

6.2 Limitations and future work

The results relating to recovery of densities and bulk moduli are restricted to two-dimensional numerical phantom media which are piecewise homogeneous and lossless. The acoustic excitation signals used are synthetic and assumed to take a Gaussian-modulated sinusoidal form and to be noiseless. With these signals, the pressure response on solving the wave equations using *k-Wave* is known, and transduction between physical pressures and voltages does not play a role. The transceivers are treated as points. Future work in this area, including development of the *ENIM* technique of Chapter 4 should relax these assumptions.

The *ENIM* technique itself relies on a pre-determined number of simple parametric models of pulse traveltime based on source and receiver co-ordinates which may break down for some reflector shapes, e.g. concave ones with sufficiently small radii of curvature, which in seismology are known to cause confounding features known as “bow-tie” artifacts in arrival time patterns []. The form of these models additionally relies on the assumption that the sound speed in the medium overlying a given reflection event (averaged over the traveltime of a ray) is further assumed to be approximately the same for all rays participating in the event. The description given in Chapter 4 of the misalignment between modelled organ locations and their physical locations is extremely limited: further work in this area should include all rigid degrees of freedom and allow for deformation by parametrizing the compartment interfaces in a higher dimensional fashion, with level sets being one example. The *number* of (squared) traveltime models present is assumed to be determinable from visual inspection of the observed signals, and not to change throughout the minimisation of $\mathcal{E}_{\text{ENIM}}$. With the assumptions above removed, an important part of any future work on *ENIM* must be to determine how good an *initial* (image-based) registration of anatomical compartments into physical (ultrasound) space is required for this last condition to hold, so that *ENIM* can successfully "complete" the registration while recovering the tissue properties. Future work should also aim to determine the circumstances under which the gradient of $\mathcal{E}_{\text{ENIM}}$ can be computed using the adjoint field method. Minimisation of *any* signal dissimilarity criterion might also benefit from speed gains if a Newton-type method can be used instead of conjugate gradients, as mentioned in Chapter 5.

Although determination of densities and bulk moduli does not require the interrogating waves to propagate nonlinearly, *ENIM* relies to some extent on linear propagation, since echoes contained in signals are assumed to retain profiles that correlate meaningfully with a template pulse. It may then be unsuited to attempts to estimate B/A using a non-linear wave equation.

The multimodal image registration problem in Chapter 5 while not the main focus of the work, is limited mainly in the small number of datasets used and the relative inefficiency of the MATLAB implementations. Further work here should start with an implementational framework more suited to speed and throughput of data based on C++, such as *ITK*. A considerably greater number of image datasets should be used for the experiments. Any training needed to determine operational parameters should be done in a way that does more to avoid bias in results.

References

[1] Lynn, J.G., Zwember, R.L., Chick, A.J., Miller, A.E.: A new method for the generation and use of focused ultrasound in experimental biology. The Journal of General Physiology **26** (1942) 179–192

[2] Wood, R.W., Loomis, A.: The physical and biological effects of high frequency sound-waves of great intensity. Philosophical Magazine **4** (1927) 417

[3] Grutzmacher, L.: Piezoelektrischer kristall mit ultraschallkonvergenz. Zeitschrift f ur Physik **96** (1935) 342

[4] Kennedy, J., Wu, F., ter Haar, G., Gleeson, F., Phillips, R., Middleton, M., Cranston, D.: High-intensity focused ultrasound for the treatment of liver tumours. Ultrasonics **42** (2004) 931–935

[5] ter Haar, G., Coussios, C.: High intensity focused ultrasound: Physical principles and devices. International Journal of Hyperthermia **23** (2007) 89–104

[6] Larrat, B., Pernot, M., Aubry, J.F., Dervishi, E., Sinkus, R., Seilhean, D., Marie, Y., Boch, A.L., Fink, M., Tanter, M.: Mr-guided transcranial brain hifu in small animal models. Physics in Medicine and Biology **55** (2010) 365–388

[7] Leslie, T.A., Kennedy, J.E.: High intensity focused ultrasound in the treatment of gynaecological diseases. International Journal of Hyperthermia **23** (2007) 173–182

[8] Jung, S.E., Cho, S.H., Jang, J.H., Han, J.Y.: High-intensity focused ultrasound ablation in hepatic and pancreatic cancer: complications. Abdominal Imaging (2010)

[9] Dick, E.A., Gedroyc, W.M.W.: Exablate® magnetic resonance-guided focused ultrasound system in multiple body applications. Expert Review of Medical Devices **7** (2010) 589–597

[10] Esnault, O., FRanc, B., Ménégaux, F., Rouxel, A., Kerviler, E.D., Bourrier, P., Lacoste, F., Chapelon, J.Y., Leenhardt, L.: High-intensity focused ultrasound ablation of thyroid nodules: First human feasibility study. Thyroid **21** (2011) 965–973

[11] Hynynen, K., McDannold, N., Vykhodtseva, N., Jolesz, F.A.: Noninvasive mr imaging-guided focal opening of the blood-brain barrier in rabbits. Radiology **220** (2001) 640–646

[12] Vaezy, S., Andrew, M., Kaczkowski, P., Crum, L.: Image-guided acoustic therapy. Annual Review of Biomedical Engineering **3** (2001) 375–390

[13] Chen, D., Xia, R., Chen, X.: Sonoknife: Feasibility of a line-focused ultrasound device for thermal ablation therapy. Medical Physics **38** (2011) 4372–4385

[14] Tempany, C.M.C., McDannold, N.J., Hynynen, K., Jolesz, F.A.: Focused ultrasound surgery in oncology: Overview and principles. Radiology **259** (2011) 39–56

[15] sun Kim, Y., Rhim, H., Choi, M.J., Lim, H.K., Choi, D.: High-intensity focused ultrasound therapy: an overview for radiologists. Korean Journal of Radiology **9** (2008) 291–302

[16] Sannholm, F.: Automated treatment planning in magnetic resonance guided high intensity focused ultrasound. Master's thesis, Aalto University (2011)

[17] Paulides, M.M., Stauffer, P.R., Neufeld, E., Maccarini, P., Kyriakou, A., Canters, R.A.M., adn J F Bakker, C.D., Rhoon, G.C.V.: Simulation techniques in hyperthermia treatment planning. International Journal of Hyperthermia **29** (2013) 346–357

[18] Duck, F.: Physical Properties of Tissue: A Comprehensive Reference Book. Academic Press, London (1990)

[19] Bamber, J.C., Cosgrove, D.O., Page, J., Bossi, C.: *In-vivo* sound speed in normal liver by whole-body transit-time measurement using a real-time scanner. In: Euroson '87, Proceedings of the 6th European Congress on Ultrasound in Medicine and Biology, M. Linzer (ed.) p. 306. (1987)

[20] Bamber, J.C., Hill, C.R.: Ultrasonic attenuation and propagation speed in mammalian tissues as a function of temperature. Ultrasound in Medicine and Biology **5** (1979) 149–157

[21] Bowen, T., Connor, W.G., Nasoni, R.L., Pifer, A.E., Sholes, R.R.: Measurement of the temperature dependence of the velocity of ultrasoiund in soft tissues. In: Ultrasonic Tissue Characterization II. US Government Printing Office, Washington, DC (1979)

[22] Buschmann, W., Voss, M., Kemmerling, S.: Acoustic properties of normal human orbit tissues. Ophthalmological Research **1** (1970) 354–364

[23] Errabolu, R.L., Sehgal, C.M., Bahn, R.C., Greenleaf, J.J.: Measurement of ultrasonic nonlinear parameter in excised fat tissues. Ultrasound in Medicine and Biology **14** (1988) 137–146

[24] ICRP: Report of the task group on reference man, icrp publication 23, international commission on radiological protection. Technical report, ICRP, Pergamon Press, Oxford (1975)

[25] ICRU: Tissue substitutes in radiation dosimetry and measurement, icru report 44, international commission on radiation units and measurements. Technical report, ICRU, Bethseda, MD, USA (1989)

[26] Lewin, P.A., Busk, H.: *In-vivo* ultrasonic measurement of tissue properties. In: 1982 IEEE Ultrasonics Symposium Proceedings, p. 709-712. (1982)

[27] Miles, C.A., Fursey, G.A.J. In: *In-vivo* Meausrement of Body Composition in Meat Animals. Elsevier Applied Science (1984) 93–105

[28] Nasoni, R.L., Bowen, T., Connor, W.G., Sholes, R.R.: *In-vivo* temperature dependence of ultrasound speed in tissue and its application to noninvasive temperature monitoring. Ultrasonic Imaging **1** (1979) 34–43

[29] Rajagopalan, B., Greenleaf, J.F., Thomas, P.J., Johnson, S.A., R C Bahn, R.C.: Variation of acoustic speed with temperature in various excised human tissues studied by ultrasound computed tomography. In: Euroson ’87, Proceedings of the 6th European Congress on Ultrasound in Medicine and Biology, M. Linzer (ed.) pp. 227-233. (1979)

[30] Robinson, D.E., Chen, C.F., Wilson, L.S.: Experience in sound speed measurement in liver and spleen. In: Proceedings of Euroson ’87, Finnish Society for Ultrasound in Medicince and Biology, p. 305. (1987)

[31] Sehgal, C.M., Brown, G.M., Bahn, R.C., Greenleaf, J.F.: Measurement and use of acoustic nonlinearity and sound speed to estimate composition of excised livers. Ultrasound in Medicine and Biology **12** (1986) 865–874

[32] Sollish, B.D.: A device for measuring ultrasonic propagation velocity in tissue. In: Euroson ’87, Proceedings of the 6th European Congress on Ultrasound in Medicine and Biology, M. Linzer (ed.) pp. 53-56. (1979)

[33] Woodard, H.Q., White, D.R.: The composition of body tissues. British Journal of Radiology **59** (1986) 1209–1219

[34] Diem, K., Lentner, C., eds.: Documenta Geigy Scientific Tables. Geigy, Macclesfield (1970)

[35] Bamber, J.C.: Chapter 4: Ultrasonic Properties of Tissues. In: Ultrasound in Medicine. IoP Publishing Ltd. (1998) 57–88

[36] Konofagou, E.E.: Quo vadis elasticity imaging? Ultrasonics **42** (2004) 331–336

[37] Kuc, R.: Estimating acoustic attenuation from refleced ultrasound signals: Comparison of spectral-shift and spectral difference approaches. IEEE Transactions on Acoustics, Speech, and Signal Processing **ASSP-32** (1984) 1–6

[38] Abeyratne, U.R., Petropulu, A.P., Reid, J.M.: On modeling the tissue response from ultrasonic b-scan images. IEEE Transactions on Medical Imaging **15** (1996) 476–490

[39] Kolios, M.C., Czarnota, G.J., Lee, M., Hunt, J.W., Sherar, M.D.: Ultrasonic spectral parameter characterization of apoptosis. Ultrasound in Medicine and Biology **28** (2002) 589–597

[40] Lizzi, F.L., Ostromogilsky, M., Feleppa, E.J., Rorke, M.C., Yaremo, M.M.: Relationship of ultrasonic spectral parameters to features of tissue microstructure. IEEE Transactions on Ultrasonics, Ferroelectrics and Frequency Control **UFFC-33** (1986) 319–329

[41] Lizzi, F.L., Astor, M., Liu, T., Deng, C., Coleman, D.J., Silverman, R.H.: Ultrasonic spectrum analysis for tissue assays and therapy evaluation. International Journal of Imaging Systems Technology **8** (1997) 3–10

[42] Lizzi, F.L., Astor, M., Feleppa, E.J., Shao, M., Kalisz, A.: Statistical framework for ultrasonic spectral parameter imaging. Ultrasound in Medicine and Biology **23** (1997) 1371–1382

[43] Lizzi, F.L., Feleppa, E.J., Alam, S.K., Deng, C.X.: Ultrasonic spectrum analysis for tissue evaluation. Pattern Recognition Letters **24** (2003) 637–658

[44] Machado, C.B., de Albuquerque Pereira, W.C., Meziri, M., Laugier, P.: Characterization of *In Vitro* healthy and pathological human liver tissue periodicity using backscattered ultrasound signals. Ultrasound in Medicine and Biology **32** (2006) 649–657

[45] Oelze, M.L., Jr, W.D.O.: Method of improved scatterer size estimation and application to parametrid imaging using ultrasound. Journal of the Acoustical Society of America **112** (2002) 3053–3063

[46] Oelze, M.L.: Characterization of tissue microstructure using ultrasonic backscatter: Theory and technique for optimization using a gaussian form factor. Journal of the Acoustical Society of America **112** (2002) 1202–1211

[47] Waag, R.C.: A review of tissue characterization from ultrasonic scattering. IEEE Transactions on Biomedical Engineering **BME-31** (1984) 884–893

[48] Thijssen, J.M., Oosterveld, B.J.: Speckle and texture in echography: Artifact or information. In: IEEE Ultrasonics Symposium. (1986)

[49] Thijssen, J.M.: Ultrasonic tissue characterization and echographic imaging. Physics in Medicine and Biology **34** (1989) 1667–1674

[50] Wells, P.N.T.: Ultrasonic imaging of the human body. Reports in Progress in Physics **62** (1999) 671–722

[51] Mast, T.D.: Empirical relationships between acoustic parameters in human soft tissues. Acoustics Research Letters Online **12** (2000) 37–42

[52] Glide, C., Duric, N., Littrup, P.: Novel approach to evaluating breast density utilizing ultraound tomography. Medical Physics **34** (2007) 744–753

[53] Littrup, P., Duric, N., Jr., R.R.L., Azevedo, S.G., Candy, J.V., Moore, T., Chambers, D.H., Mast, J.E., Johnson, S.A., Holsapple, E.: Characterizing tissue with acoustic parameters derived from ultrasound data. Submitted to Medical Imaging, 2002 (2002)

[54] Glide-Hurst, C.K., Duric, N., Littrup, P.: Volumetric breast density evaluation from ultrasound tomography images. Medical Physics **35** (2008) 3988–3997

[55] Gemmeke, H., Ruiter, N.V.: 3d ultrasound computer tomography for medical imaging. Nuclear Intruments and Methods in Physics Research **A 580** (2007) 1057–1065

[56] Duck, F.A., Baker, A.C., Starritt, H.C., eds.: Ultrasound in Medicine. Institute of Physics Publishing (1998)

[57] Fan, X., Hynynen, K.: The effect of wave reflection and refraction at soft tissue interfaces during ultrasound hyperthermia treatments. Journal of the Acoustical Society of America **91** (1992) 1727–1736

[58] Fan, X., Hynynen, K.: The effects of curved tissue layers on the power deposition patterns of therapeutic ultrasound beams. Medical Physics **21** (1994) 25–34

[59] Damianou, C.A., Sanghvi, N.T., Fry, F.J.: Dependence of ultrasonic atenuation and absorption in dog soft tissues on temperature and thermal dose. Journal of the Acoustical Society of America **102** (1997) 628–634

[60] Techavipoo, U.: Temperature dependence of ultrasonic propagation speed and attenuation in excised canine liver tissue measured using transmitted and reflected pulses. Journal of the Acoustical Society of America **115** (2004) 2859–2865

[61] Floch, C.L., Tanter, M., Fink, M.: Self-defocusing in ultrasonic hyperthermia: Experiment and simulation. Applied Physics Letters **74** (1999) 3062–3064

[62] Divkovic, G.W., Huber, P.E., Jenne, J.W.: Impact of fat layers on lesion development during hifu application - a precise experimental analysis. In: CP911, 6th International Symposium on Therapeutic Ultrasound. (2007)

[63] de Brosses, E.S., Gennisson, J.L., Pernot, M., Fink, M., Tanter, M.: Termperature dependence of the shear modulus of soft tissues assessed by ultrasound. Physics in Medicine and Biology **55** (2010) 1701–1718

[64] Konopatskaya, I.I., Mironov, M.A., Pyatakov, P.A.: Acoustical registration of shear modulus variation under hifu in soft tissues. In: CP829, Therapeutic Ultrasound: 5th International Symposium on Therapeutic Ultrasound. (2006)

[65] Kabanikhin, S.I.: Methods for solving dynamic inverse problems for hyperbolic equations. Journal of Ill-Posed Problems **12** (2004) 493–517

[66] Katchalov, A., Kurylev, Y., Lassas, M.: Inverse Boundary Spectral Problems. Chapman & Hall/CRC (2001)

[67] Romanov, V.G.: Investigation Methods for Inverse Problems. VSP (2002)

[68] Blagoveshchenskii, A.S.: Inverse Problems of Wave Processes. VSP (2001)

[69] Kuc, R., Schwarz, M.: Esimating the acoustic attenuation slope for liver from reflected ultrasound signals. IEEE Transactions on Sonics and Ultrasonics **SU-26** (1979) 353–362

[70] Sehgal, C.M., Bahn, R.C., Greenleaf, J.F.: Measurement of the acoustic nonlinearity parameter b/a in human tissues by a thermodynamic method. Journal of the Acoustical Society of America **76** (1984) 1023–1029

[71] Kim, D., Greenleaf, J.F., Sehgal, C.M.: Ultrasonic imaging of the nonlinear parameter b/a: simulation studies to evaluate phase and frequency modulation methods. Ultrasound in Medicine and Biology **16** (1990) 175–181

[72] Rietsema, J.: Assessment of ultrasound tomography as a technique for quantitative tissue characterization. PhD thesis, Eindhoven Technical University (1993)

[73] Ophir, J.: Estimation of the speed of ultrasound propagation in biological tissues: A beam-tracking method. IEEE Transactions on Ultrasonics, Ferroelectrics and Frequency Control **UFFC-33**(4) (1986) 359–368

[74] Robinson, D.E., Chen, F., Wilson, L.S.: Measurement of velocity of propagation from ultrasonic pulse-echo data. Ultrasound in Medicine and Biology **8**(4) (1982) 413–420

[75] Ashfaq, M., Ermert, H.: A new approach towards ultrasonic transmission tomography with a standard ultrasound system. In: 2004 IEEE International Ultrasonics, Ferroelectrics and Frequency Control Joint 50th Anniversary Conference. (2004)

[76] Krueger, M., Burow, V., Hiltawsky, K.M., Ermert, H.: Limited angle ultrasonic transmission tomography of the compressed female breast. In: IEEE 1998 Ultrasonics Symposium Proceedings. (1998) 1345–1348

[77] Green, P., Arditi, M.: Ultrasonic reflex transmission imaging. Ultrasonic Imaging **7** (1985) 201–214

[78] Gennisson, J.L., Deffieux, T., Fink, M., Tanter, M.: Ultrasound elastography: Principles and techniques. Diagnostic and Interventional Imaging **94** (2013) 487–495

[79] Sarvazyan, A., Skovoroda, A.R., Emelianov, S., Fowlkes, J.B.: Biophysical bases of elasticity imaging. Acoustical Imaging **21** (1995) 223–241

[80] Pinton, G., Trahey, G.: Full-wave simulation of finite-amplitude ultrasound in heterogeneous media. In: IEEE Ultrasonics Symposium. (2007)

[81] Jensen, J.A.: A model for the propagation and scattering of ultrasound in tissue. Journal of the Acoustical Society of America **89** (1991) 182–191

[82] Kelly, J.F., McGough, R.K.: Analytical time-domain green's functions for power-law media. Journal of the Acoustical Society of America **124**(5) (2008) 2861–2872

[83] Ginter, S., Liebler, M., Steiger, E., Dreyer, T.: Full-wave modeling of therapeutic ultrasound: Nonlinear ultrasound propagation in ideal fluids. Journal of the Acoustical Society of America **111** (2002) 2049–2059

[84] Pulkkinen, A., Hynynen, K.: Computational aspects in high intensity ultrasonic surgey planning. Computerized Medical Imaging and Graphics **34** (2010) 69–78

[85] Treeby, B.E., Cox, B.T.: k-wave: Matlab toolbox for the simulation and reconstruction of photoacoustic wave fields. Journal of Biomedical Optics **15** (2010) 021314–1–021314–12

[86] Huttunen, J.: Estimation of thermal parameters in tissue using focused ultrasound and mri temperature mapping. Licentiate thesis, Department of Applied Physics, University of Kuopio (September 2005)

[87] Huijssen, J., Bouakaz, A., Verweij, M.D., de Jong, N.: Simulations of the nonlinear acoustic pressure field without using the parabolic approximation. In: IEEE Ultrasonics Symposium. (2003)

[88] Huijssen, J., Verweij, M.D., de Jong, N.: Green's function method for modeling nonlinear three-dimensional pulsed acoustic fields in diagnostic ultrasound including tissue-like attenuation. In: 2008 IEEE International Ultrasonics Symposium Proceedings. (2008)

[89] Demi, L., Verweij, M.D., Huijssen, J., de Jong, N., van Dongen, K.W.A.: Attenuation of ultrasound pressure fields described via contrast source formulation. In: 2009 IEEE International Ultrasonics Symposium Proceedings. (2009)

[90] Huijssen, J., Verweij, M.D.: An iterative method for the computation of nonlinear, wide-angle, pulsed acoustic fields of medical diagnostic transducers. Journal of the Acoustical Society of America **127**(1) (January 2010) 33–44

[91] Smirnov, V.I.: A Course of Higher Mathematics IV. Pergamon Press (1964)

[92] Mast, T.D., Sourianu, L.P., Lin, D.L.D., Tabei, M., Nachman, A.I., Waag, R.C.: A k-space method for large-scale models of wave propagation in tissue. IEEE Transactions on Ultrasonics, Ferroelectrics and Frequency Control **48** (2001) 341–354

[93] Cox, B.T., Kara, S.: k-space propagation models for acoustically heterogeneous media: Application to biomedical photoacoustics. Acoustical Society of America **121** (2007) 3453–3464

[94] Treeby, B.E., Cox, B.T.: k-wave: a matlab toolbox for the simulation and reconstruction of photoacoustic wave-fields. Journal of Biomedical Optics **15**(2) (2010) 021314

[95] Treeby, B., Janos, J., Rendell, A.P., Cox, B.T.: Modeling nonlinear ultrasound propagation in heterogeneous media with power law absorption using a i-space pseudospectral method. Journal of the Acoustical Society of America **131** (2012) 4324–4336

[96] Wang, K., Teoh, E., Jaros, J., Treeby, B.: Modelling nonlinear ultrasound propagation in absorbing media using the k-wave toolbox: Experimental validation. In: IEEE Ultrasonics Symposium. (2012)

[97] Hajnal, J.V., Hill, D.L., Hawkes, D.J., eds.: Detecting Failure, Assessing Success. In: Medical Image Registration. CRC Press (2001) 117–139

[98] Modersitzki, J.: Numerical Methods for Image Registration. Oxford Science Publications (2004)

[99] Wein, W.: Multimodal Integration of Medical Ultrasound for Treatment Planning and Interventions. PhD thesis, Technical University of Munich (June 2007)

[100] Viola, P., Wells, W.M.: Alignment by maximization of mutual information. International Journal of Computer Vision **24**(2) (1997) 137–154

[101] Pagoulatos, N., Haynor, D.R., Kim, Y.: Image-based registration of ultrasound and magnetic resonance images: a preliminary study (proceedings paper). In: Medical Imaging 2000: Image Display and Visualization. Volume 3976 of SPIE., Society of Photo-Optical Instrumentation Engineers, Bellingham, WA (2000) 156–164

[102] Blackall, J.M., Rueckert, D., Maurer, C.R., Penney, G.P., Hill, D.L.G., Hawkes, D.J.: An image registration approach to automated calibration for freehand 3d ultrasound. In: MICCAI 2000. Volume 1935 of LNCS. (2000)

[103] Studholme, C., Hill, D.L.G., Hawkes, D.J.: An overlap invariant entropy measure of 3d medical image alignment. Pattern Recognition **32**(1) (1999) 71–86

[104] Maintz, J.A., Viergever, M.A.: A survey of medical image registration. Medical Image Analysis **2**(1) (1998) 1–36

[105] Roche, A., Malandain, G.: Multimodal image registration by maximization of the correlation ratio. Technical Report 3378, INRIA (August 1998)

[106] Roche, A., Pennec, X., Rudolph, M., Auer, D.P., Malandain, G., Ourselin, S., Auer, L.M., Ayache, N.: Generalized correlation ratio for rigid registration of 3d ultrasound with mr images. In: MICCAI 2000. Volume 1935 of LNCS., Springer, Berlin/Heidelberg (2000) 203–220

[107] Roche, A., Pennec, X., Malandain, G., Ayache, N.: Rigid registration of 3-d ultrasound with mr images: A new approach combining intensity and gradient information. IEEE Transactions on Medical Imaging **20** (2001) 1038–1049

[108] Mellor, M., Brady, M.: Non-rigid multimodal image registration using local phase. In: LNCS 3216. (2004)

[109] Mellor, M., Brady, M.: Phase mutual information as a similarity measure for registration. Medical Image Analysis **9** (2005) 330–343

[110] Mellor, M., Brady, M.: Fluid registration of ultrasound using multi-scale phase estimates. Unknown **unknown** (2005) unknown

[111] Jian, B., Vemuri, B.C., Marroquin, J.L.: Robust nonrigid multimodal image registration using local frequency maps. In: LNCS 3565. (2005)

[112] Dalvi, R., Abugharbieh, R., Pickering, M., Scarvell, J., Smith, P.: Registration of 2d to 3d joint images using phase-based mutual information. In: Proc. of SPIE Vol. 6512. (2007)

[113] Grau, V., Becher, H., Noble, J.A.: Registration of multiview real-time 3-d echocardiographic sequences. IEEE Transactions on Medical Imaging **26**(9) (2007) 1154–1165

[114] Penney, G., Blackall, J., Hamady, M., Sabharwal, T., Adam, A., Hawkes, D.: Registration of freehand 3d ultrasound and magnetic resonance liver images. Medical Image Analysis **8** (2004) 81–91

[115] Wein, W., Röper, B., Navab, N.: Automatic registration and fusion of ultrasound with ct for radiotherapy. In: MICCAI 2005. Volume 3750 of LNCS., Springer, Heidelberg (2005) 303–311

[116] Wein, W., Khamene, A., Clevert, D.A., Kutter, O., Navab, N.: Simulation and fully automatic multimodal registration of medical ultrasound. In: MICCAI 2007. Volume 4791 of LNCS., Springer, Heidelberg (2007) 136–143

[117] Wein, W., Brunke, S., Khamene, A., Callstrom, M.R., Navab, N.: Automatic ct-ultrasound registration for diagnostic imaging and image-guided intervention. Medical Image Analysis **12** (2008) 577–585

[118] Kutter, O., Wein, W., Navab, N.: Multi-modal registration based ultrasound mosaicing. In: MICCAI 2009. Volume 5761 of LNCS. (2009) 763–770

[119] King, A.P., Ma, Y.L., Yao, C., Jansen, C., Razavi, R., Rhode, K.S., Penney, G.P.: Image-to-physical registration for image-guided interventions using 3-d ultrasound and an ultrasound imaging model. In: Image Processing in Medical Imaging. (2009)

[120] Gill, S., Mousavi, P., Fichtinger, G., Chen, E., Boisvert, J., Pichora, D., Abolmaesumi, P.: Biomechanically constrained groupwise us to ct registration of the lumbar spine. In: LNCS 5761. (2009)

[121] Wein, W., Röper, B., Navab, N.: Integrating diagnostic *B*-mode ultrasonography into ct-based radiation treatment planning. IEEE Transactions on Medical Imaging **26** (2007) 866–879

[122] Milko, S., Melvær, E.L., Samset, E., Kadir, T.: Evaluation of bivariate correlation ratio similarity metric for rigid registration fo us/mr images of the liver. Int J CARS **4** (2009) 147–155

[123] Goss, S.A., Cobb, J.W., Frizzell, L.A.: Effect of beamwidth and thermocouple size on the measurement of acoustic absorption using the thermoelectric technique. In: IEEE Ultrasonic Symposium Proceedings. (1977) IEEE Cat. e77CH1264-1SU.

[124] Frizzel, L.A., Carstensen, E.L., Davis, J.D.: Ultrasonic absorption in liver tissue. Journal of the Acoustical Society of America **65** (1979) 1309–1312

[125] Liu, J., Chauris, H., Calandra, H.: The normalized integration method - an alternative to full waveform inversion? In: EAGE Near Surface, the 17th European Meeting of Environmental and Engineering Geophysics, B07. (2011)

[126] Luo, J., Wu, R.S.: Seismic envelope inversion: reduction of local minima and noise resistance. Geophysical Prospecting **63** (2015) 597–614

[127] Tarantola, A.: Inversion of seismic reflection data in the acoustic approximation. Geophysics **49** (1984) 1259–1266

[128] Crocker, M.J., ed.: Parameters of nonlinearity in acoustic media. In: Encyclopedia of Acoustics, Vol 1. John Wiley & Sons, Inc., Hoboken, NJ, USA (1997) 219–226

[129] Morse, P.M., Ingard, K.U.: Theoretical Acoustics. McGraw-Hill (1968)

[130] Plessix, R.E.: A review of the adjoint-state method for computing the gradient of a functional with geophysical applications. Geophysical Journal International **167** (2006) 495–503

[131] Norton, S.J.: Iterative inverse scattering algorithms: Methods of computing fréchet derivatives. Journal of the Acoustical Society of America **106** (1999) 2653–2660

[132] Bob, B.B.: The normalized integration method. bobsjournal **1** (2011) 1–10

[133] Fowler, C.M.R.: The Solid Earth. Cambridge University Press (2005)

[134] Fichtner, A., Trampert, J.: Hessian kernels of seismic data functionals based upon adjoint techniques. Geophysical Journal International **185** (2011) 775–798

[135] Davis, J.W.: Improved arrival time detection for cardiac pulse transit sonomicrometry. In: Computers in Cardiology. (1996)

[136] McNew, J.: Application of acoustic ray tracing to determine sound pathways into the human head. Master's thesis, University of Illinois at Urbana Champaign (2008)

[137] Avanesians, P., Momayez, M.: Wave separation: Application for arrival time detection in ultrasonic signals. Ultrasonics **55** (2015) 15–25

[138] Fischler, M.A., Bolles, R.C.: Random sample consensus: a paradigm for model-fitting with applications to image-analysis and automated cartography. Communications of the ACM **24** (1981) 381–395

[139] Tarel, J.P., Ieng, S.S., Charbonnier, P.: A constrained-optimization based half-quadratic algorithm for robustly fitting sets of linearly parametrized curves. Advances in Data Analysis and Classification **2** (2008) 227–239

[140] Scales, J.A.: Theory of Seismic Imaging. Springer (1995)

[141] Sheriff, R.E., Geldart, L.P.: Exploration Seismology. Cambridge University Press (1995)

[142] Shearer, P.M.: Introduction to Seismology. Cambridge University Press (2009)

[143] Jensen, J.A., Nikolov, S.: Fast simulation of ultrasound images. In: proceedings of the IEEE Ultrasonics Symposium in Puerto Rico. (October 2000)

[144] Ng, J., Prager, R., Kingsbury, N., Treece, G., Gee, A.: Modelling ultrasound imaging as a linear, shift-variant system. IEEE Transactions on Ultrasonics, Ferroelectrics and Frequency Control **53** (2006) 549–563

[145] Ng, J., Prager, R., Kingsbury, N., Treece, G., Gee, A.: Wavelet restoration of medical pulse-echo ultrasound images in an em framework. IEEE Transactions on Ultrasonics, Ferroelectrics and Frequency Control **54** (2007) 550–568

[146] Shams, R., Hartley, R., Navab, N.: Real-time simulation of medical ultrasound from ct images. In: MICCAI 2008. Volume 5242 of LNCS., Springer, Heidelberg (2008) 734–741

[147] Jensen, J.A., Svendsen, J.B.: Calculation of pressure fields from arbitrarily shaped, apodized and excited ultrasound transducers. IEEE Transactions on Ultrasonics, Ferroelectrics and Frequency Control **39** (1992) 262–267

[148] Jensen, J.A.: Field: A program for simulating ultrasound systems. In: Nordic-Baltic Conference on Biomedical Imaging Published in Medical & Biological Engineering & Computing. (1996)

[149] Fitzpatrick, J.M., West, J.B., Calvin R. Maurer, J.: Predicting error in rigid-body point-based registration. IEEE Transactions on Medical Imaging **17**(5) (1998) 694–702

[150] Heanes, D.: Ultrasound image simulation for data fusion in image-guided interventions. MPhil/PhD First Year Internal Report

[151] Haberman, R.: Elementary Applied Partial Differential Equations: with Fourier Series and Boundary Value Problems. Prentice Hall, Upper Saddle River, NJ (1998)

[152] Wolfram, S.: www.wolframalpha.com

Appendix A

Conservation equations for a fluid

A.1 mass conservation

Consider a region $\mathcal{D}$ with boundary $\partial\mathcal{D}$ through which a fluid is free to flow. The rate of change of the fluid mass inside $\mathcal{D}$ is equal to the mass flux through $\partial\mathcal{D}$ *into* $\mathcal{D}$, i.e. with normal surface vector $\hat{\mathbf{n}}$ directed outwards we have,

$$\frac{d}{dt}\iiint\limits_{\mathcal{D}} \rho(\mathbf{x},t)\, d^3x = -\oiint\limits_{\partial\mathcal{D}} \rho\mathbf{U}\cdot\hat{\mathbf{n}}\, dS. \tag{A.1}$$

Using the Divergence Theorem to turn the surface integral into a volume integral,

$$\frac{d}{dt}\iiint\limits_{\mathcal{D}} \rho(\mathbf{x},t)\, d^3x = -\iiint\limits_{\mathcal{D}} \nabla\cdot(\rho\mathbf{U})\, d^3x. \tag{A.2}$$

Since this holds for *any* arbitrary region $\mathcal{D}$, we must have

$$\frac{d\rho}{dt} + \nabla\cdot(\rho\mathbf{U}) = 0. \tag{A.3}$$

A.2 momentum conservation

Consider a *small* fluid element of mass m, momentarily contained inside the cubical region of volume $\delta x\delta y\delta z$ shown in Fig. A.1 and not subject to any external forces. Writing down Newton's Second Law for this element *and following it on its motion path*, we have, in cartesian co-ordinates

$$\begin{bmatrix} d(mU_x)/dt \\ d(mU_y)/dt \\ d(mU_z)/dt \end{bmatrix} = \begin{bmatrix} (P(x)-P(x+\delta x)\delta y\delta z) \\ (P(y)-P(y+\delta y)\delta z\delta x) \\ (P(z)-P(z+\delta z)\delta x\delta y), \end{bmatrix}, \tag{A.4}$$

i.e.

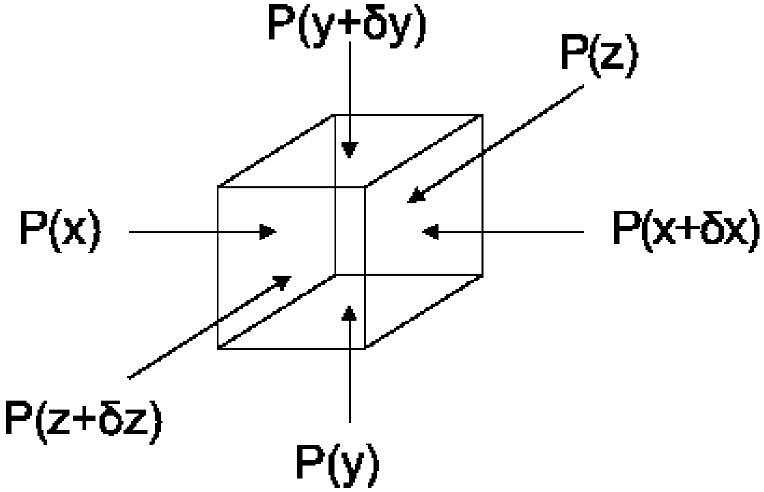

Figure A.1: Fluid element

$$\begin{bmatrix} d(\rho\delta x\delta y\delta z U_x)/dt \\ d(\rho\delta x\delta y\delta z U_y)/dt \\ d(\rho\delta x\delta y\delta z U_z)/dt \end{bmatrix} = \begin{bmatrix} (-\partial P/\partial x)\delta x\delta y\delta z) \\ (-\partial P/\partial y)\delta x\delta y\delta z) \\ (-\partial P/\partial z)\delta x\delta y\delta z), \end{bmatrix}. \tag{A.5}$$

Since the dimensions of the element are arbitrary, we have

$$\frac{d(\rho\mathbf{U})}{dt} = -\nabla P \tag{A.6}$$

or, in fluid dynamics language, to emphasize that the derivative on the left is taken *following* the fluid,

$$\frac{D(\rho\mathbf{U})}{Dt} = -\nabla P. \tag{A.7}$$

If the element is sufficiently small, changes in density will be of a much smaller size than changes in velocity, so that the following approximation becomes valid.

$$\frac{D(\mathbf{U})}{Dt} = -\frac{\nabla P}{\rho}. \tag{A.8}$$

Eq. 3.2 is equivalent to Eq. A.8 with its left hand side Lagrangian derivative written out in full using the chain rule.

Appendix B

d'Alembert's solution to the 1D scalar wave equation

Consider the inhomogeneous initial value problem, and a particular point in 1D space, x_i, with reference to Fig. B.1. Only sources within the region R can influence the field u at the point in 1D space, x_i when a wave of speed c propagates.

$$\begin{aligned} c^2 u_{xx}(x,t) - u_{tt}(x,t) &= s(x,t) \\ u(x,0) &= f(x) \\ u_t(x,0) &= g(x). \end{aligned} \quad \text{(B.1)}$$

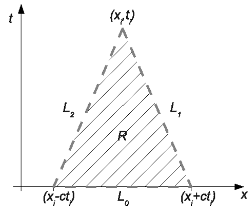

Figure B.1: Influence region

D'Alembert's solution to problem B.1 begins [151] by integrating the wave equation over R

$$\int\int_R \left(c^2 u_{xx}(x,t) - u_{tt}(x,t)\right)\,dxdt = \int\int_R s(x,t)\,dxdt$$

Green's theorem turns this into a line integral anticlockwise around the boundary of R

$$\int_{L_0\cup L_1\cup L_2} \left(-c^2 u_x(x,t)dt - u_t(x,t)dx\right) = \int\int_R s(x,t)\,dxdt.$$

The part along L_0 simplifies to

$$\int_{x_i-ct_i}^{x_i+ct_i} -u_t(x,0)\,dx = -\int_{x_i-ct_i}^{x_i+ct_i} g(x)\,dx. \quad \text{(B.2)}$$

Along L_1, we have that $x+ct$ is constant, i.e. that $dx - cdt = 0$ and the contribution to the integral becomes

$$
\begin{aligned}
&\int_{L_1} \left(c^2 u_{xx}(x,t) - u_{tt}(x,t)\right)\, dxdt \\
&\qquad = \int_{L_1} \left(-c^2 u_x(x,t)dt - u_t(x,t)dx\right) \\
&\qquad = \int_{L_1} \left(cu_x(x,t)dx + cu_t(x,t)dt\right) \\
&\qquad = c\int_{L_1} du(x,t) \\
&\qquad = cu(x_i,t_i) - cf(x_i + ct_i),
\end{aligned}
\tag{B.3}
$$

and along L_2,

$$
\begin{aligned}
&\int_{L_1} \left(c^2 u_{xx}(x,t) - u_{tt}(x,t)\right)\, dxdt \\
&\qquad = \int_{L_1} \left(-c^2 u_x(x,t)dt - u_t(x,t)dx\right) \\
&\qquad = -\int_{L_1} \left(cu_x(x,t)dx + cu_t(x,t)dt\right) \\
&\qquad = -c\int_{L_1} du(x,t) \\
&\qquad = -\left(cf(x_i + ct_i) - cu(x_i,t_i)\right) \\
&\qquad = cu(x_i,t_i) - cf(x_i - ct_i).
\end{aligned}
\tag{B.4}
$$

Combining B.2, B.3 and B.4 finally gives

$$
u(x,t) = \frac{f(x+ct) + f(x-ct)}{2} + \frac{1}{2c}\int_{x-ct}^{x+ct} g(x')\, dx' + \frac{1}{2c}\int_0^t \int_{x-c(t-t')}^{x+c(t-t')} s(x',t')\, dx'\, dt'. \tag{B.5}
$$

Appendix C

The Hilbert Transform of a signal

Hilbert Transform of a time-varying function $f(t)$ is defined as

$$H[f](t) = \frac{1}{\pi}\int_{-\infty}^{\infty} \frac{f(\tau)}{\tau - t}\, d\tau.$$

The *analytic signal* and *envelope* of f are given, respectively, by

$$f_a(t) = f(t) + iH[f](t), \quad E[f](t) = \left\| f_a(t) \right\|_2. \tag{C.1}$$

The derivative of $E[f]$ with respect to the value of f at any time is given by

$$\frac{\partial E[f](\tau)}{\partial f(t)} = \begin{cases} \frac{f(t)}{E[f](t)} & \text{for} \quad \tau = t \\ \frac{H[f](\tau)}{\pi(\tau - t)E[f](\tau)} & \text{for} \quad \tau \neq t. \end{cases} \tag{C.2}$$

Appendix D

Time integral of a Gaussian-modulated pulse

The integral of a complex-valued Gaussian pulse with centre frequency ω and unit standard deviation may be expressed as a series expansion for large ω [152]

$$\int e^{-t^2} e^{i\omega t}\, dt = e^{i\omega t} \left(-\frac{ie^{-t^2}}{\omega} - \frac{2(e^{-t^2}t)}{\omega^2} + \frac{2ie-t^2(2t^2-1)}{\omega^3} + O\left(\left(\frac{1}{\omega} \right)^4 \right) \right) - \frac{1}{2}\sqrt{\pi} e^{-\frac{\omega^2}{4}} i^{2\lfloor \frac{arg(t(t-i\omega))}{2\pi} \rfloor} \tag{D.1}$$

Retaining only the first term of the right-hand side, gives an approximate result in the taking the form of another Gaussian pulse, scaled down and phase-shifted,

$$\int e^{-t^2} e^{i\omega t}\, dt \approx e^{it\omega} \left(-\frac{ie^{-t^2}}{\omega} \right). \tag{D.2}$$

If the original pulse envelope has a width specified by σ, this result becomes

$$\int e^{\frac{-t^2}{2\sigma^2}} e^{i\omega t}\, dt \approx \frac{1}{2} e^{it\omega} \left(-\frac{2i}{\omega} e^{\frac{-t^2}{2\sigma^2}} \right). \tag{D.3}$$

Appendix E

Seismic diffraction hyperbolae

Following [142], for a point scatterer at depth h and horizontal distance x from a collocated source and receiver ($\mathbf{x}_s = \mathbf{x}_r$) with medium velocity V, the two-way travel time t is given by

$$\frac{V^2t^2}{4h^2} - \frac{x^2}{h^2} = 1.$$

Following [141], for a horizontal plane reflector at depth h, medium velocity V and horizontal “offset” $x = |\mathbf{x}_r - \mathbf{x}_s|$,

$$\frac{V^2t^2}{4h^2} - \frac{x^2}{4h^2} = 1.$$

Further, for a plane reflector “dipped” at an angle ξ to the horizontal, at a normal distance h from the source and with horizontal “offset” $x = |\mathbf{x}_r - \mathbf{x}_s|$,

$$\frac{V^2t^2}{(2h\cos\xi)^2} - \frac{(x + 2h\sin\xi)^2}{(2h\cos\xi)^2} = 1.$$

The first two of these are hyperbolae in $x - t$ with the symmetry axis $x = 0$. The third is an hyperbola with symmetry axis $x = -2h\sin\xi$.

Appendix F

Local phase and orientation

The local phase, ϕ and local orientation o in an image, I, are calculated, for a 3D image, from the outputs of filters

$$\begin{aligned} H_1(u,v,w) &= \frac{u}{\sqrt{u^2+v^2+w^2}} \\ H_2(u,v,w) &= \frac{v}{\sqrt{u^2+v^2+w^2}} \\ H_3(u,v,w) &= \frac{w}{\sqrt{u^2+v^2+w^2}}, \end{aligned}$$

where u, v, w are spatial frequency co-ordinates in Fourier space. By additionally applying a bandpass filter, g_s, such as a log-Gabor filter, ϕ and o can be found at multiple scales, labelled by s, as

$$o(I(\mathbf{r}),s) = \frac{((g_s \star h_1 \star I)(\mathbf{r}), (g_s \star h_2 \star I)(\mathbf{r}), (g_s \star h_3 \star I)(\mathbf{r}),)}{\sum_{i=1}^{3}((g_s \star h_i \star I)(\mathbf{r}))^2} \tag{F.1}$$

$$\phi(I(\mathbf{r}),s) = \tan^{-1}\left(\sqrt{\sum_{i=1}^{3}(g_s \star h_1 \star I)(\mathbf{r}))^2}, (g_s \star I)(\mathbf{r})\right), \tag{F.2}$$

where h_1, h_2, h_3 are the spatial domain versions of H_1, H_2, H_3.